N 69 21022
NASA CR 100433

NATIONAL AERONAUTICS AND SPACE ADMINISTRATION

CASE FILE COPY

Space Programs Summary 37-55, Vol. II

The Deep Space Network

For the Period November 1 to December 31, 1968

JET PROPULSION LABORATORY
CALIFORNIA INSTITUTE OF TECHNOLOGY
PASADENA, CALIFORNIA

January 31, 1969

NATIONAL AERONAUTICS AND SPACE ADMINISTRATION

Space Programs Summary 37-55, Vol. II

The Deep Space Network

For the Period November 1 to December 31, 1968

JET PROPULSION LABORATORY
CALIFORNIA INSTITUTE OF TECHNOLOGY
PASADENA, CALIFORNIA

January 31, 1969

SPACE PROGRAMS SUMMARY 37-55, VOL. II

Copyright © 1969
Jet Propulsion Laboratory
California Institute of Technology

Prepared Under Contract No. NAS 7-100
National Aeronautics and Space Administration

Preface

The Space Programs Summary is a multivolume, bimonthly publication that presents a review of technical information resulting from current engineering and scientific work performed, or managed, by the Jet Propulsion Laboratory for the National Aeronautics and Space Administration. The Space Programs Summary is currently composed of four volumes:

Vol. I. *Flight Projects* (Unclassified)

Vol. II. *The Deep Space Network* (Unclassified)

Vol. III. *Supporting Research and Advanced Development* (Unclassified)

Vol. IV. *Flight Projects and Supporting Research and Advanced Development* (Confidential)

Foreword

Volume II of the Space Programs Summary reports the results of work performed by the Deep Space Network (DSN). Information is presented, as appropriate, in the following categories:

Introduction
- Description of the DSN
- Description of DSN Systems

Mission Support
- Interplanetary Flight Projects
- Planetary Flight Projects
- Manned Space Flight Project
- Advanced Flight Projects

Advanced Engineering
- Tracking and Navigational Accuracy Analysis
- Communications System Research
- Communications Elements Research
- DSN Programming

Facility Development and Operations
- Space Flight Operations Facility
- Ground Communications Facility
- Deep Space Instrumentation Facility

Design and Implementation of Technical Structures and Utilities

In each issue, the section entitled "Description of DSN Systems" reports the current configuration of one of the six DSN systems (tracking, telemetry, command, monitoring, simulation, and operations control). The fundamental research carried out in support of the DSN is reported in Vol. III.

Contents

I. Introduction 1

A. Description of the DSN 1

B. Description of DSN Systems: Operations Control System
L. W. Miller 3

II. Mission Support 7

A. *Mariner V* Extended Mission Operations
D. J. Mudgway 7

B. *Mariner* Mars 1971 Missions
D. J. Mudgway 7

C. *Apollo 7* Mission
P. S. Goodwin 8

D. Advanced Flight Projects
J. R. Hall 10

III. Advanced Engineering: Tracking and Navigational Accuracy Analysis 12

A. Introduction
T. W. Hamilton and D. W. Trask 12

B. Evaluation of Errors in h_{max} on the DPODP Ionosphere Model
L. M. Webb and B. D. Mulhall 13

C. Conversion of Faraday Rotation Data to Ionospheric Measurements
B. D. Mulhall and K. L. Thuleen 15

D. Conversion of Ionospheric Measurements to Doppler Correction for Deep Space Probe Tracking Data
B. D. Mulhall and R. N. Wimberly 19

E. *Lunar Orbiter* Gravity Analysis
P. M. Muller and W. L. Sjogren 23

F. Mass Distributions Inferred From *Lunar Orbiter* Tracking Data
P. Gottlieb 25

G. *Pioneer IX* Trajectory and Orbit Determination
A. Khatib and G. Reynolds 26

IV. Advanced Engineering: Communications Systems Research 30

A. Low Data Rate Communication: Block-Coded Frequency Shift Keying
R. M. Goldstein 30

B. Frequency Generation and Control: Programmable RF Attenuator
S. Fisher 36

C. Multiple-Mission Command: Considerations for Command Communications
R. C. Tausworthe 39

Contents (contd)

V. Advanced Engineering: Communications Elements Research 44

A. Low Noise Receivers: Microwave Maser Development
R. Berwin 44

B. Determination of Antenna Temperatures and Flux From Cygnus-A Observations at S-Band
R. E. Cormack 45

C. Efficient Antenna Systems: X-Band Gain Measurements, 85-ft Antenna
R. A. Norman 47

D. Efficient Antenna Systems: X-Band Gain Measurements, 210-ft AAS
D. A. Bathker 50

E. Efficient Antenna Systems: Comparison of the Calculated Gain of the AAS With a Unicone Feed to the Gain With a Tricone Feed
S. A. Brunstein 55

F. *Pioneer VI* Faraday Rotation Solar Occultation Experiment
G. S. Levy, C. T. Stelzried, T. Sato, and B. L. Seidel 57

VI. Advanced Engineering: DSN Programming 60

A. Mission-Independent Telemetry Decommutation
S. Mandell and F. Lesh 60

B. Data Recovery From a Noisy Telemetry Channel: An Algorithm to Smooth Doubly Contaminated Data
R. Lewis 65

VII. DSIF Development and Operations 73

A. Surveillance TV Camera for Monitoring Antenna Area
C. Lundy 73

B. Antenna-Surface Thermal Deflection Study
V. B. Lobb and M. Kron 74

C. New Technique for Setting Perforated Plate Panels
F. W. Stoller and J. Carpenter 75

D. Venus DSS Activities
E. B. Jackson, J. D. Campbell, R. M. Gosline, and A. L. Price 77

E. Klystron Characteristics at Reduced Output Levels
R. C. Chernoff 79

F. X-Band Time Synchronization Transmitter
R. E. Arnold 81

G. Wide-Band Doubler and Sine Wave Quadrature Generator
R. B. Crow 85

H. Division 33 Hi-Rel Module Development: A Line Driver for the DSIF Standard Logic Module Family
D. W. Slaughter 89

Contents (contd)

VIII. Design and Implementation of Technical Structures and Utilities 92

A. Pioneer DSS Antenna Surface Reset
V. B. Lobb and J. Carpenter 92

B. Mars DSS Operation Support Building Implementation
T. Potter 94

C. Reconfiguration of Goldstone DSCC Communications Centers
B. G. Bridges 97

I. Introduction

A. Description of the DSN

The Deep Space Network (DSN), established by the NASA Office of Tracking and Data Acquisition under the system management and technical direction of JPL, is responsible for two-way communications with unmanned spacecraft traveling approximately 10,000 mi from earth to interplanetary distances. It supports, or has supported, the following NASA deep space exploration projects: *Ranger*, *Surveyor*, *Mariner* Venus 1962, *Mariner* Mars 1964, *Mariner* Venus 67, *Mariner* Mars 1969, *Mariner* Mars 1971, and *Mariner V* extended mission operations (JPL); *Lunar Orbiter* (Langley Research Center); *Pioneer* (Ames Research Center); and *Apollo* (Manned Spacecraft Center), as backup to the Manned Space Flight Network (MSFN).

The DSN is distinct from other NASA networks such as the MSFN, which has primary responsibility for tracking the manned spacecraft of the *Apollo* Project, and the Space Tracking and Data Acquisition Network (STADAN), which tracks earth-orbiting scientific and communications satellites. With no future unmanned lunar spacecraft presently planned, the primary objective of the DSN is to continue its support of planetary and interplanetary flight projects. Future activities may include support of certain foreign deep-space flight projects.

To provide this support of flight projects, the DSN simultaneously performs advanced engineering on components and systems, integrates proven equipment and methods into the network,[1] and provides direct support of each project through that project's Tracking and Data System. This management element and the project's Mission Operations System are responsible for the design and operation of the data system, software system, and operations system required in the conduct of mission operations. The organization and procedures necessary to carry out these activities were described in SPS 37-50, Vol. II, pp. 15–17.

In providing the direct support of a flight project, the DSN performs three basic functions:

(1) *Tracking:* locating the spacecraft; measuring its distance, velocity, and position; and following its course.

(2) *Data acquisition:* recovering information from the spacecraft in the form of telemetry, namely, engineering measurements and scientific data.

(3) *Command:* sending coded signals to the spacecraft to activate equipment to initiate spacecraft functions.

To accomplish these functions, six DSN systems have been established: (1) tracking, (2) telemetry, (3) command, (4) monitoring, (5) simulation, and (6) operations control.

[1]When a new piece of equipment or new method has been accepted for integration into the network, it is classed as Goldstone duplicate standard (GSDS), thus standardizing the design and operation of identical items throughout the network.

The DSN can be characterized as being comprised of three facilities: the Deep Space Instrumentation Facility (DSIF), the Ground Communications Facility (GCF), and the Space Flight Operations Facility (SFOF).

1. Deep Space Instrumentation Facility

a. Tracking and data acquisition facilities. A worldwide set of deep space stations (DSSs) with large antennas, low-noise phase-lock receiving systems, and high-power transmitters provide radio communications with spacecraft. The DSSs and the deep space communications complexes (DSCCs) they comprise are given in Table 1.

Radio contact with a spacecraft usually begins when the spacecraft is on the launch vehicle at Cape Kennedy, and it is maintained throughout the mission. The early part of the trajectory is covered by selected network stations of the Air Force Eastern Test Range (AFETR) and the MSFN of the Goddard Space Flight Center.[2] Normally, two-way communications are established between the spacecraft and the DSN within 30 min after the spacecraft has been injected into lunar, planetary, or interplanetary flight. A compatibility test station at Cape Kennedy (discussed later) monitors the spacecraft continuously during the launch phase until it passes over the local horizon. The deep space phase begins with acquisition by either the Johannesburg, Woomera, or Tidbinbilla DSS. These and the remaining DSSs given in Table 1 provide radio communications to the end of the flight.

To enable continuous radio contact with spacecraft, the DSSs are located approximately 120 deg apart in longitude; thus, a spacecraft in deep space flight is always within the field-of-view of at least one station, and for several hours each day may be seen by two stations. Furthermore, since most spacecraft on deep space missions travel within 30 deg of the equatorial plane, the DSSs are located within latitudes of 45 deg north or south of the equator. All DSSs operate at S-band frequencies: 2110–2120 MHz for earth-to-spacecraft transmission and 2290–2300 MHz for spacecraft-to-earth transmission.

To provide sufficient tracking capability to enable useful data returns from around the planets and from the edge of the solar system, a 210-ft-diam-antenna network will be required. Two additional 210-ft-diam-antenna DSSs are being established at Madrid and Canberra, starting in 1969. These DSSs, scheduled to be operational by early-1973, will operate in conjunction with the Mars DSS to provide this capability.

b. Compatibility test facilities. In 1959, a mobile L-band compatibility test station was established at Cape Kennedy to verify flight-spacecraft/DSN compatibility prior to the launch of the *Ranger* and *Mariner* Venus 1962

[2]The 30-ft-diam-antenna station established by the DSN on Ascension Island during 1965 to act in conjunction with the MSFN orbital support 30-ft-diam-antenna station was transferred to the MSFN in July 1968.

Table 1. Tracking and data acquisition stations of the DSIF

DSCC	Location	DSS	Antenna		Year of initial operation
			Diameter, ft	Type of mounting	
Goldstone	California	Pioneer	85	Polar	1958
		Echo[a]	85	Polar	1962
		(Venus)[b]	(85)	(Az–El)	(1962)
		Mars	210	Az–El	1966
Canberra	Australia	Woomera[c]	85	Polar	1960
		Tidbinbilla[c]	85	Polar	1965
—	South Africa	Johannesburg[c]	85	Polar	1961[d]
Madrid	Spain	Robledo[c]	85	Polar	1965
		Cebreros[c]	85	Polar	1967

[a]Established in 1959 to support NASA's *Echo* Project to explore the feasibility of transcontinental two-way communications using a passive satellite; the Echo DSS was originally configured with an 85-ft-diam Az–El-mounted antenna. In 1962, when the need arose for a second 85-ft-diam polar-mounted antenna at the Goldstone site, the 85-ft-diam Az–El-mounted antenna was moved to the Venus DSS, and an 85-ft-diam polar-mounted antenna was constructed at the Echo DSS.

[b]A research-and-development facility used to demonstrate the feasibility of new equipment and methods to be integrated into the operational network. Besides the 85-ft-diam Az–El-mounted antenna, the Venus DSS has a 30-ft-diam Az–El-mounted antenna that is used for testing the design and operation of the feed system for the Mars DSS 210-ft-diam antenna.

[c]Normally staffed and operated by government agencies of the respective countries (except for a temporary staff at the Madrid DSCC), with some assistance of U.S. support personnel.

[d]Between 1958 and 1962, a temporary mobile tracking station was located near Johannesburg to provide L-band communications required by the *Ranger* and *Mariner* Venus 1962 spacecraft.

spacecraft. Experience revealed the need for a permanent facility at Cape Kennedy for this function. An S-band compatibility test station with a 4-ft-diam antenna became operational in 1965. In addition to supporting the preflight compatibility tests, this station monitors the spacecraft continuously during the launch phase until it passes over the local horizon.

Spacecraft telecommunications compatibility in the design and prototype development phases was formerly verified by tests at the Goldstone DSCC. To provide a more economical means for conducting such work and because of the increasing use of multiple-mission telemetry and command equipment by the DSN, a compatibility test area was established at JPL in 1968. In all essential characteristics, the configuration of this facility is identical to that of the 85- and 210-ft-diam-antenna stations.

The JPL compatibility test area is used during spacecraft system tests to establish the compatibility with the DSN of the proof test model and developmental models of spacecraft, and the Cape Kennedy compatibility test station is used for final flight spacecraft compatibility validation testing prior to launch.

2. Ground Communications Facility

The GCF, using, in part, facilities of the worldwide NASA Communications Facility (NASCOM),[3] provides voice, high-speed data, and teletype communications between the SFOF and all DSSs, except those of the Goldstone DSCC. Communications between the Goldstone DSCC and the SFOF are provided by a microwave link leased from a common carrier. Early missions were supported with voice and teletype circuits only, but increased data rates necessitated the use of wide-band circuits from all DSSs.

3. Space Flight Operations Facility

Network and mission control functions are performed by the SFOF at JPL. (Prior to 1964, these functions were performed in temporary facilities at JPL.) The SFOF receives data from all DSSs and processes that information required by the flight project to conduct mission operations. The following services are provided: (1) real-time processing and display of tracking data; (2) real-time and non-real-time processing and display of telemetry data; (3) simulation of flight operations; (4) near-real-time evaluation of DSN performance; (5) operations control, and status and operational data display; and (6) general support such as internal communications by telephone, intercom, public address, closed-circuit TV, documentation, and reproduction of data packages. Master data records of science data received from spacecraft are generated. Technical areas are provided for flight project personnel who analyze spacecraft performance, trajectories, and generation of commands.

The SFOF is equipped to support many spacecraft in flight and those under test in preparation for flight. Over a 24-hour period in 1967, as many as eight in-flight spacecraft or operational-readiness tests for flight were supported by the SFOF.

[3]Managed and directed by the Goddard Space Flight Center.

B. Description of DSN Systems: Operations Control System, *L. W. Miller*

1. Functions

The DSN operations control system is the mechanism for directing DSN facilities, systems, and resources in support of flight operations; it provides information to aid in DSN operations planning and efficient utilization of the DSN facilities, systems, and resources. System functions are as follows: (1) real-time operations control, (2) resource allocation, (3) discrepancy reporting, (4) operations analysis, and (5) operations data bank maintenance.

2. System Elements

The DSN subsystems and equipment that contribute to the operation of the current DSN operations control system are:

(1) IBM 7094 processor.

(2) SFOF internal communications.

(3) SFOF display system.

(4) Operations control area in the SFOF.

(5) GCF equipment providing voice and teletype channels to the DSSs.

3. System Operation

The relationship of the operations control system to the other DSN systems and to flight projects is shown in simplified conceptual form in Fig. 1.[4] The "products" of the DSN are the data generated by the tracking,

[4]The simplifications made on Fig. 1 are: (1) the direct interface from mission control to the command system is not shown, and (2) the DSN simulation system is not shown since it is considered an exact replacement for the spacecraft and/or the tracking, telemetry, and command systems during testing.

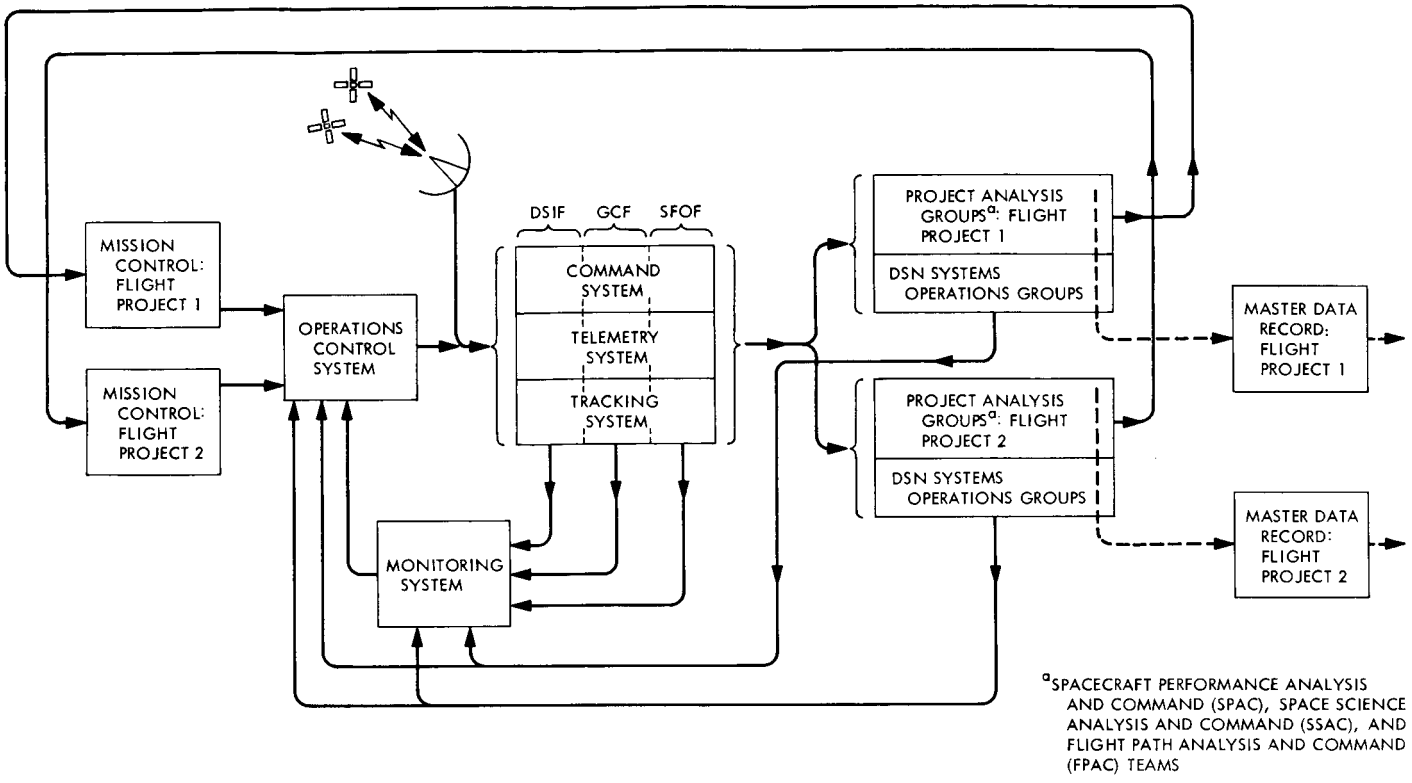

Fig. 1. Interfaces between the operations control system, other DSN systems, and flight projects

telemetry, and command systems. These data are certified by the DSN systems operations groups and processed by the project analysis groups prior to their transmittal to form a master data record.

As a result of the data analysis, the project analysis groups transmit information about the spacecraft to mission control, which, if necessary, directs operations control to take specific action. In a similar manner, DSN status is reported to operations control by the monitoring system and the DSN systems operations groups. From the information gained concerning DSN status, together with previous planning, the DSN operations control system can respond to the project request with direction and control to the DSN systems and facilities. The major functional elements that tie together for direction and control are real-time operations control, resource allocation, and discrepancy reporting.

Additional functions associated with the operations control system that are under development are those of operations analysis and operations data bank maintenance.

a. Real-time operations control. The following information is input for the operations control function:

(1) Resource allocations.

(2) Status reports for the DSN systems and facilities.

(3) Status reports for each flight project.

(4) Flight project priorities.

(5) Flight project commitments, as defined in the NASA Support Plan.

(6) Flight project nominal plan, as defined in the DSN Operations Plan.

(7) Real-time direction from each flight project.

Using this input, the following information is generated:

(1) Resource reallocations.

(2) Direction and control to the DSN systems and facilities.

(3) Operations status reports to the DSN systems and facilities.

(4) Conflict resolutions.

(5) DSN status reports to mission control.

The normal mode of system operation is to maintain the DSN at the preplanned commitment level. During a mission, the real-time status as reported by the monitoring system, facilities, the discrepancy reporting system, and the flight project is compared to the commitments determined from the DSN Operations Plan, the NASA Support Plan, and the resource allocation system. Any deviation from these plans is corrected by the DSN control team. Project direction for real-time changes come from mission control and the project analysis groups through the DSN/project interface team directed by the DSN project engineer. These requests are transmitted to the DSN control team for appropriate action.

b. Resource allocation. To provide simultaneous tracking coverage and telemetry support for several flight projects, careful planning and efficient assignment of available DSN resources are required. A capability for periodic updating of the allocations as user requirements change is also required. Commitments are made to the limits of the total available resources, using guidelines specified in such documents as the Support Instrumentation Requirements Document and priorities established by NASA Headquarters. All DSN operations are scheduled by the DSN operations control chiefs and the DSN scheduling office in the SFOF. The resource allocation scheduling system involves the following three levels of scheduling:

Short-range schedule. Requests for support are placed 10 to 14 days prior to the period covered by the 7-day schedule. These requests are compatible with commitments established by the middle-range schedule. The 7-day schedule allocates all DSN resources on an hour-by-hour basis at a subsystem level of detail.

Middle-range schedule. Requests for the middle-range schedule are made prior to submission of the 7-day schedule requests. The facility detail is at a major subsystem level, but the time basis is in specific hours per day (view periods). This schedule is an updated version of the long-range schedule, but covers a shorter time and is expanded in facility detail. Conflicts are considered enough in advance to allow some rescheduling of activities into the slack time available. If rescheduling is not possible, the matter is referred to NASA Headquarters. The current 12-wk middle-range schedule is being modified to meet the objectives of a middle-range schedule under the DSN resource allocation system.

Long-range schedule. The long-range 72-wk resource allocation schedule applies to DSN coverage commitments to users at DSS and major computer system levels and DSN personnel staffing levels. Commitments of the major system resources are made on a specific-hours-per-day basis. Non-time-sensitive requirements such as testing and maintenance are included on an hours-per-week basis. Conflicting requirements are resolved in a DSN/user joint allocation meeting prior to issuance of the schedule. The long-range schedule is included as a commitment document attached to the DSN Operations Plan for each flight project.

c. Discrepancy reporting. The discrepancy reporting system is a network-wide system of failure reporting, engineering analysis, and management action to ensure proper DSN support of flight operations and continuing reliability of DSN equipment. To realize these objectives, the system was developed on two levels. The first provides a controlled closed-loop method for systematically reporting and correcting operational (e.g., procedural, equipment, and computer program) failures or problems. The second level serves to locate design deficiencies, identify specific component weaknesses, and evaluate equipment reliability.

d. Operations analysis. The operations analysis function involves evaluation of the effectiveness of system procedures (e.g., standard operating procedures, data shipping procedures, and man–machine interface procedures) and analysis of queueing, scheduling, and operations information flow problems.

e. Operations data bank maintenance. The operations data bank is comprised of the following elements:

(1) Historical data on DSN operational performance, capabilities, and configurations.

(2) Statistics on the actual measured DSN operational performance in terms of such factors as reliability and effectiveness.

(3) Applicable documents describing current DSN operational capabilities and configurations.

(4) Applicable documents describing current DSN policies, guidelines, standard operating procedures, and configuration change control procedures.

(5) Approved and proposed operational development plans and listings of the systems affected by them.

(6) Operational documents, plans, requirements, and status reports concerning present and future missions supported by the DSN.

(7) Other applicable documents required for projecting the DSN operations workload.

Information is cross-filed and indexed for easy accessibility in DSN operations control and planning.

II. Mission Support

A. *Mariner V* Extended Mission Operations, D. J. Mudgway

The planning, preparation, and operational support provided for the *Mariner V* Extended Mission Operations (MEMO) Project through October 20, 1968, was described in Vol. II of SPS 37-51, pp. 20, 21, and SPS 37-54, pp. 11, 12. On October 20, two-way lock was obtained, but the downlink signal continued to exhibit the same characteristics it had exhibited since its first detection on October 14; i.e., the signal remained approximately 10 dB below the predicted power level and approximately 30 kHz above the predicted frequency. Also, attempts to send commands to the spacecraft were unsuccessful. To understand and, if possible, resolve the apparent spacecraft anomaly, observations of the spacecraft signal, interspersed with command attempts, were continued at regular intervals until November 5. Since the anomaly was not resolved, DSN support of the *Mariner V* reacquisition activity was terminated at that time.

Support of the MEMO Project afforded all elements of the DSN an opportunity to apply recent innovations and refinements in planning, documentation, implementation, and pre-mission testing procedures. Improvements were particularly apparent in DSN documentation, in the resolution of schedule conflicts regarding allocation of station time, and in the planning for master data record production. Thus, it can be stated that, although the primary objective of the project was not attained, valuable experience was gained by the DSN in meeting its support commitments.

B. *Mariner* Mars 1971 Missions, D. J. Mudgway

Planning and coordination activities for *Mariner* Mars 1971 mission support continued during this reporting period. Requirements for DSN participation in project design team activities (e.g., spacecraft system, mission operations, and mission design), project reviews, and documentation production increased significantly.

Considerable progress was made by the DSN capabilities planning team in defining the baseline capabilities of each required DSN system. Block diagrams, which are available for the telemetry, tracking, command, and monitoring systems, include descriptions of supporting hardware and software. This material provides a common baseline concerning DSN capabilities for use by the other project-related teams.

An implementation schedule for DSN support as part of the project's Tracking and Data System provides for achieving operational readiness by December 1970. At that time, the DSN will be made available to the project for training and testing on an operational basis in preparation for launch readiness in May 1971. The first two

milestones on the schedule, namely, the production of an estimated capabilities document and the definition of DSN system requirements, have been accomplished thus far.

C. *Apollo 7* Mission, *P. S. Goodwin*

1. Introduction

The DSN support furnished to the MSFN for the *Apollo 4* and *5* missions was summarized in SPS 37-50, Vol. II, pp. 27–33. The *Apollo 6* DSN support was described in SPS 37-51, Vol. II, pp. 21–25. Support provided by the Cape Kennedy Compatibility Test Station (CTS), the Tidbinbilla DSS MSFN wing, and the Robledo DSS MSFN wing during the launch and subsequent flight of *Apollo 7* is described here.

2. Mission Description

The AS-205 (*Apollo 7*) spacecraft, the first manned *Apollo* spacecraft, was launched at 15:02:45 GMT on October 11, 1968, from Pad 34 at Cape Kennedy. It carried astronauts W. M. Schirra, Jr., D. F. Eisele, and W. Cunningham into a slightly elliptical earth orbit with an initial altitude of 123–153 nmi. The mission, lasting approximately 10 days, 20 h, 9 min, was designed primarily to check out the spacecraft in its entirety and to provide crew training for rendezvous with the *S-IVB* third-stage vehicle. Included was a complete checkout of the entire communications system, including real-time TV transmission to earth while the spacecraft was over the United States. All mission objectives were met with the successful splashdown of *Apollo 7* at 11:11:48 GMT on October 22.

3. Cape Kennedy CTS Support

As was the case with *Apollos 4*, *5* and *6*, the Cape Kennedy CTS provided informal assistance to the MSFN Merritt Island Station during the countdown and launch. The station was configured in a manner identical to that for the *Apollo 4* mission (SPS 37-50, Vol. II, p. 31); i.e., the command service module (CSM) S-band downlink signal was received at the Cape Kennedy CTS, and the detected phase modulation telemetry baseband was relayed to the MSFN Merritt Island Station for processing in the event that multipath or flame attenuation caused reception difficulties at the Merritt Island Station that might possibly not be experienced at the Cape Kennedy CTS.

The significant difference between the AS-501 (*Apollo 4*) and AS-205 launches was that the AS-205 launch was from Pad 34, just a few miles almost directly north of the Cape Kennedy CTS (as may be seen in Fig. 1), and the AS-501 launch was from Pad 39, several miles distant on Merritt Island. The Cape Kennedy CTS was a very strategic location for providing cross-support to the MSFN Merritt Island Station. The prelaunch and postlaunch tracking by the Cape Kennedy CTS was accomplished using the manually steerable 4-ft antenna shown in Fig. 1.

a. Countdown demonstration test. The countdown demonstration test was started on September 11 at the $T - 96$ h point in the countdown.[1] Support of the countdown by the Cape Kennedy CTS also started at $T - 96$ h when the command service module S-band signal was turned on. The Cape Kennedy CTS received the S-band signal, transmitted the telemetry from the S-band receiver to the MSFN Merritt Island Station for processing, photographed the RF spectrum, and reported the relative sideband amplitudes to the MSFN Merritt Island Station. This support was provided from 08:55 until 10:02 GMT, when the S-band signal was turned off. The MSFN Merritt Island Station reported that good telemetry was received during this period.

The terminal portion of the countdown demonstration test started on September 15 with the reactivation of the S-band signal at $T - 6$ h, 50 min. The Cape Kennedy CTS was requested by the Manned Spacecraft Center at Houston to provide an RF spectrum analysis utilizing a technique devised at the Cape Kennedy CTS. During the terminal count, the Cape Kennedy CTS ran the RF spectrum analysis program and found the following spurious signals on the S-band RF carrier spectrum:

Frequency from carrier, kHz	Relative amplitude from carrier, dB
±30	−12
±51.2	−29
±70.0	−12

The 30- and 70-kHz signals from the MSFN Merritt Island Station, which were the uplink command and voice subcarriers, were turned around in the spacecraft transponder.

[1]"*T*-minus" time differs from "launch-minus" (*L*) time because the latter must account for the built-in holds (*L* time displays a larger negative number). During a countdown, the *T* clock stops during the holds, while the *L* clock continues to count down toward launch. The *T* and *L* clocks are in step after the last hold.

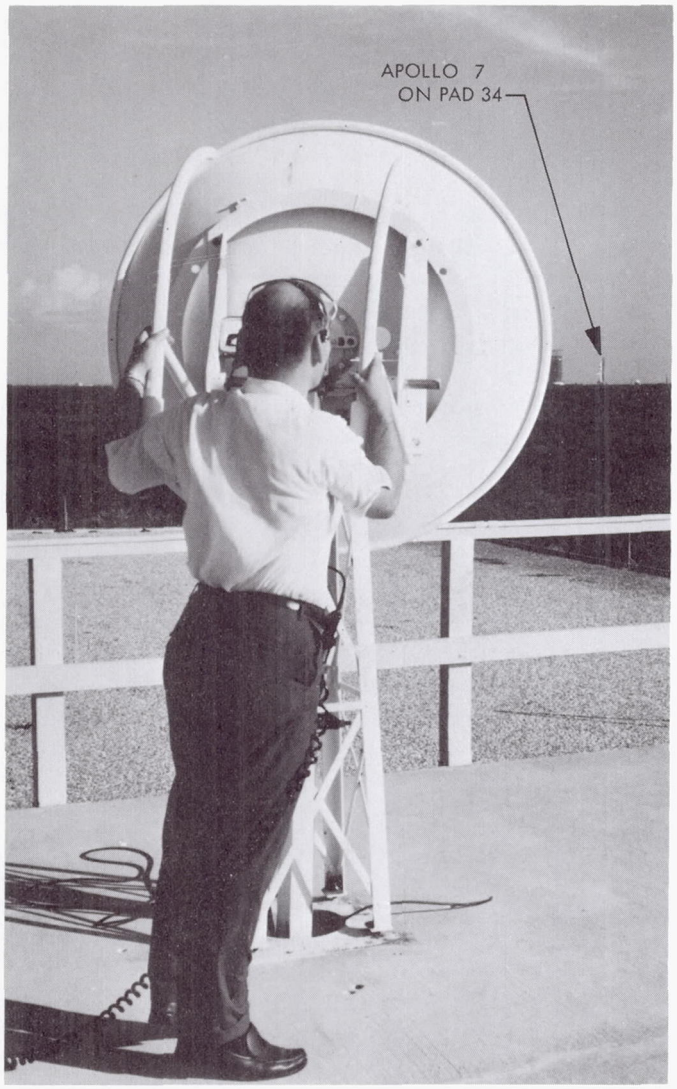

Fig. 1. Cape Kennedy DSS antenna being readied for AS-205 (*Apollo 7*) launch

b. Countdown and launch. The Cape Kennedy CTS participation in the launch countdown began at 20:05 GMT on October 6 for the S-band signal test at $T - 98$ h. The command service module S-band signal was turned off at 00:00 GMT on October 7.

The next participation was at $T - 6$ h, 50 min in the count at 02:42 GMT on October 11. The Cape Kennedy CTS provided the same support as before, and good data were received at the MSFN Merritt Island Station. At liftoff at 15:02:45 GMT, the Cape Kennedy CTS had a received signal level of −63 dBm. The Cape Kennedy CTS manually tracked the spacecraft from liftoff until 15:12:21 GMT, except for a momentary drop of lock at 15:04:43 GMT. The spacecraft was manually tracked using prelaunch predicted look angles. Automatic gain control meters from the receiver to the antennas also helped the antenna operator follow the spacecraft after loss of visual siting.

The data from the countdown and launch were distributed to the MSFN Merritt Island Station and the Marshall Space Flight Center in Huntsville, Alabama, for evaluation.

4. Support by DSS MSFN Wings

Although the MSFN wings at the DSSs were not committed to support the earth-orbital *Apollo* missions, a need existed for operational training of personnel to prepare them for support of the forthcoming lunar missions. With the successful participation in *Apollo 7* support on a "best-effort" basis by the Tidbinbilla DSS and Robledo DSS MSFN wings,[2] personnel at each of the three DSS MSFN wings have received this required preliminary training.

a. Tidbinbilla DSS MSFN wing. The *Apollo 7* mission occurred at the same time the Tidbinbilla DSS control room was undergoing a major reconfiguration in preparation for the early-November *Pioneer IX* launch and the subsequent *Mariner* Mars 1969 spacecraft launch in early-1969. Since the equipment in the MSFN wing was not affected by the reconfiguration work, arrangements were made with the MSFN to provide *Pioneer VIII* tracking cross-support utilizing the antenna with the MSFN wing equipment. The station continued *Pioneer VIII* tracks intermixed with the essential *Apollo* premission test activities up to the time of the AS-205 launch.

The Tidbinbilla DSS MSFN wing participated with the Canberra (Honeysuckle) MSFN Station in the MSFN station readiness tests conducted October 3 and again October 9 and 10. On October 10, the station completed a *Pioneer VIII* pass and associated post-tracking calibration at 15:00 GMT. The station was reconfigured and checked out in the MSFN configuration at 22:00 GMT on October 10. The terminal count and launch support preparations were then initiated on October 11 at 04:30 GMT.

The first acquisition of *Apollo 7* on revolution 1 was at 16:04 GMT. During revolutions 14–16, a leak occurred in the hydraulic system at the Tidbinbilla DSS MSFN wing

[2]A major structural upgrade of the Pioneer DSS antenna precluded participation of the Pioneer DSS MSFN wing in *Apollo 7* support; this MSFN wing did, however, support the *Apollo 4, 5,* and *6* missions.

that reduced the tracking-rate capability of the station and limited its coverage during these revolutions. The leak was repaired, and normal operations were resumed during the next visibility period on revolution 27.

With the exception of two minor anomalies, the Tidbinbilla DSS MSFN wing tracked *Apollo 7* on each available orbit (total of 32 passes) until the end of revolution 105 on October 17, at which time the station was relieved of further *Apollo 7* support in order to prepare for the *Pioneer IX* launch.

b. Robledo DSS MSFN wing. The *Apollo 7* mission was the first in which the Robledo DSS MSFN wing participated. (The restart anomaly of the *S-IVB* third-stage vehicle prevented its scheduled participation in the *Apollo 6* mission; see SPS 37-51, Vol. II, p. 25.) Preparations for *Apollo 7* support at the Robledo DSS MSFN wing started at 23:00 GMT on October 10 with a Class A countdown completed at 08:30 GMT on October 11. Although the station maintained a standby condition for the launch, the *Apollo 7* trajectory was such that the station could not track until revolution 12.

On October 16 during revolution 87, the Robledo DSS MSFN wing received a handover from the MSFN Canary Island Station and went into a two-way track. This was the first *Apollo* two-way track experienced by the Robledo DSS in the MSFN configuration.

With the exception of an October 14 search for the *Mariner V* spacecraft, the Robledo DSS MSFN wing participated in the daily *Apollo 7* tracks through October 22 (total of 32 passes) and revolution 161 (the final pass over the station). However, at the request of the MSFN, the station remained on standby status until the actual spacecraft splashdown, to be used if an anomaly had occurred during the retromaneuver over the Hawaiian Islands.

D. Advanced Flight Projects, *J. R. Hall*

The Tracking and Data Acquisition (T&DA) Office at JPL provides planning support to both established NASA flight projects and to proposed advanced flight projects not yet formally established or funded as operating projects within the NASA Office of Space Science and Applications (OSSA) structure. The OSSA is also sponsoring planning support to an advanced flight project of the Federal Republic of Germany.

The objective of this planning support is to determine, as early as possible, the future T&DA requirements imposed by mission designs and to provide guidelines for the T&DA development activities to match projected capabilities to those requirements. Mission operations and telecommunications design teams, composed of flight project and T&DA personnel, assist in the development of the requirements. A tentative T&DA capability commitment for future T&DA support is provided by an Estimated Capabilities Document. This document, which discusses required preliminary configurations and capabilities for both the near-earth and deep space phases, is later superseded by the NASA Support Plan.

Advanced flight projects for which planning support is being provided include those described below:

1. *Viking* Mission

The objective of the *Viking* Project is to soft-land a scientific instrument package on the surface of Mars. The present mission design incorporates an out-of-orbit deboost of the lander vehicle. An orbiting spacecraft will provide a relay link from the lander to earth, as well as orbital science and imagery data. Overall project management and lander system management responsibilities have been assigned to the Langley Research Center; orbital spacecraft system management responsibility has been assigned to JPL. Launch is anticipated for mid-1973, using a *Titan III/Centaur* launch vehicle.

An Estimated Capabilities Document has been published. The *Viking* mission will probably be the first fully supported by the Mark III system. Coverage early in the mission will be provided by an 85-ft-antenna network. A third-generation central computer in the SFOF will be used for mission operations and analysis. All mission control functions will be performed at the SFOF.

2. *Pioneer F* and *G* Missions

The *Pioneer F* and *G* missions are presently designed as Jupiter flyby missions, with the first launch anticipated for early-1972 and the second launch 1 yr later. Planetary science will include fields and particles measurements and imagery. Considerable interplanetary data, particularly through the asteroid belt, will also be obtained during the approximately 650 days of flight. The spacecraft, spin-stabilized in the equatorial plane, will carry a 9-ft high-gain antenna pointed to earth. An *Atlas/Centaur/* T364 launch vehicle is planned.

A preliminary Estimated Capabilities Document has been formulated. Present plans indicate that support up to encounter will be provided by an 85-ft-antenna network

and that planetary science support during encounter will be provided by the 210-ft-antenna network now under development. The SFOF will be utilized for mission control and analysis functions during all critical mission phases.

3. *Planetary Explorer* Missions

Five *Planetary Explorer* missions are planned to obtain fields and particles measurements in Venus and Mars orbits. The first launch to Venus is anticipated for early-1972 and that to Mars, for mid-1973. The three additional launches are planned for successive Venus and Mars opportunities. The spin-stabilized spacecraft will carry an electronically de-spun high-gain antenna. An augmented *Thor/Delta* launch vehicle is planned.

Although such missions are normally supported by an 85-ft-antenna network, the *Planetary Explorer* spacecraft will be designed to take advantage of any enhancement a 210-ft-antenna network could provide. Until the Estimated Capabilities Document for this project is available, the corresponding document for the *Mariner* Mars 1971 Project is being used as a basis for planning.

4. *Helios* Mission

The West German *Helios* spacecraft will be designed to carry a fields and particles scientific instrument package to within 0.3 AU of the sun. Periapsis will be reached 72 days after launch, and the primary science objective should be accomplished approximately 28 days later. The spacecraft, spin-stabilized perpendicular to the ecliptic, will carry a mechanically de-spun high-gain antenna. The first launch is anticipated for early-1974, using an *Atlas/Centaur*/T364 launch vehicle provided by NASA. The second launch will follow in late-1975.

Both West German and NASA T&DA facilities will be utilized. Primary DSN support will be provided by an 85-ft-antenna network, but the spacecraft will be designed to take advantage of any enhancement a 210-ft-antenna network could provide. Mission control and analysis functions will be performed at the SFOF during the first 2 to 4 wk of the mission and at the West German Control Center near Munich thereafter. A preliminary Estimated Capabilities Document has been published that specifies use of the Mark III system. However, the spacecraft will be designed on the basis of the T&DA capabilities available for the *Mariner* Mars 1971 Project.

5. Thermoelectric Outer-Planet Spacecraft (TOPS) Missions

Guidelines for projected T&DA capabilities have been provided to assist in planning studies of outer-planet "tours" during 1975–1980. A "TOPS precursor" mission is planned for 1974. To enhance the value of such missions, the estimated capabilities of the spacecraft/ground telecommunications system that are listed below are purposely both technically and programmatically ambitious:

(1) Spacecraft storage of imaging data, with playback at X-band as the primary mode and playback at S-band as a backup mode.

(2) Spacecraft storage of cruise science data, with playback at S-band as the primary mode and playback at X-band and real-time transmission at either S-band or X-band as backup modes.

(3) Continuous transmission of spacecraft engineering telemetry and two-way tracking data at S-band using low-, medium-, and/or high-gain spacecraft antennas, with a matching capability for continuous reception on the ground.

(4) Multiple spacecraft telemetry data transmission rates to accommodate either improved or degraded link performance, including increased rates if two or more 210-ft antennas are available for reception.

(5) Coded telemetry transmission such that the maximum required signal-to-noise ratio would be 1.5 to 3.0 dB for the telemetry sideband energy.

(6) S-band uplink and simultaneous coherent S-band and X-band downlink tracking for calibration of charged particle effects to increase navigational accuracy and for radio science propagation experiments.

(7) Capability to accommodate low data rates (0.1–10 bits/s) requiring use of higher-stability oscillators and RF carrier tracking bandwidths from 1 to 10 Hz.

(8) Continuous reliable spacecraft command reception capability using low- to medium-gain antennas (with no verification required via the engineering telemetry link), with a matching capability for continuous ground transmission.

(9) Direct transmission of commands from the control center through ground stations.

(10) Ranging over the entire mission for celestial mechanics and other scientific experiments.

III. Advanced Engineering: Tracking and Navigational Accuracy Analysis

A. Introduction, *T. W. Hamilton and D. W. Trask*

The DSN Inherent Accuracy Project was formally established by the DSN Executive Committee in July 1965. The objectives of the project are:

(1) Determination (and verification) of the inherent accuracy of the DSN as a radio navigation instrument for lunar and planetary missions.

(2) Formulation of designs and plans for refining this accuracy to its practical limits.

Achievement of these goals is the joint responsibility of the Telecommunications and Systems Divisions of JPL. To this end, regular monthly meetings are held to coordinate and initiate relevant activities. The project leader and his assistant (from the Systems and Telecommunications Divisions, respectively) report to the DSN Executive Committee, and are authorized to task project members to (1) conduct analyses of proposed experiments, (2) prepare reports on current work, and (3) write descriptions of proposed experiments. The project is further authorized to deal directly with those flight projects using the DSN regarding data-gathering procedures that bear on inherent accuracy.

The various data types and tracking modes provided by the DSIF in support of lunar and planetary missions are discussed in SPS 37-39, Vol. III, pp. 6–8. Technical work directly related to the Inherent Accuracy Project is presented in SPS 37-38, Vol. III, and in subsequent *Deep Space Network* SPS volumes, and is continued in the following sections of this volume.

If the navigation accuracy goals presently being considered for future deep space probes are to be realized, the effects of charged particles must be calibrated out of the radio tracking data. In the case of the upcoming *Mariner* Mars 1969 mission, the navigational errors incurred by ignoring the effect of the ionosphere will exceed the total budget allocated to the ground-based system during support of the planetary encounter phase. Consequently, the effect of charged particles will be modeled/calibrated out of the tracking data for the *Mariner* Mars 1969 mission; *Sections B*, *C*, and *D* discuss preparations for this effort.

The ionospheric model presently in the double precision orbit determination program is reviewed in *Section B*. Because some of the key parameters may not be available for use during the real-time operations and consequently must be estimated, the quality of these estimates and the resultant error in calibrating the charged particle effects from the tracking data are of particular concern. This article considers one of the parameters, namely, the altitude at which maximum density of free electrons h_{max} occurs, and concludes that errors in estimating h_{max} variations will at most cause a 9% error in the correction applied to the tracking data.

For the Goldstone, California tracking facility, Faraday rotation data, which is a measure of the charged particle content in the ionosphere, is available and consequently can be used to calibrate the tracking data in preference to the previously discussed model. An instrument to measure this Faraday rotation was leased by JPL in support of the *Pioneer VI* Faraday rotation solar occultation experiment as discussed in SPS 37-53, Col. II, pp. 69–71; *Section C* describes a computer program that has been developed to automatically convert the modulo π radian output of this device into a continuous data stream. However, the resultant ionospheric data have been accumulated while watching a geostationary satellite (constant probe-tracking station geometry); the actual ionospheric correction needed is that which corresponds to the electromagnetic wave path between the earth and a distant spacecraft. In the latter case the ray path is constantly changing through the ionosphere throughout the pass. The computer program that accomplishes this conversion is discussed in *Section D*, which will not only be able to handle the Faraday rotation data but also the ionosonde data collected by the Environmental Science Service Administration from stations throughout the world. At present the Faraday rotation data are only available for the Goldstone stations; therefore, corrections for the deep space stations located in Spain, South Africa, and Australia will depend on either a model or the ionosonde data.

The *Lunar Orbiter* gravity analysis, which has been regularly reported in this volume of the SPS, is continued in *Section E*. During the initial studies, doppler residuals from short arc fits were found to be invariant for low eccentricity and low inclination orbits so that cases assuming a triaxial moon show little difference from those which assume a spherical moon. However, it has been found that in the polar orbit the effect is definitely visible and can account for variations in the amplitude of the normalized acceleration signature by as much as 30%. An offset in the lunar center of gravity is suspected as the cause and is being investigated. In addition, progress and plans for two other efforts are presented: (1) the solution for a point mass gridwork that best describes the gravity variations using spacecraft at different altitudes over the same lunar surface features, and (2) a more detailed presentation of the acceleration data than the original work presented in SPS 37-53, Vol. II, pp. 10–16.

In addition to the above work, the use of a model employing 41 discrete mass points in conjunction with a triaxial moon is reported in *Section F*. The largest doppler residuals obtained when a triaxial moon model is assumed are reduced by an order of magnitude by this discrete mass model. However, the inherent accuracy of the doppler data should permit a further reduction of at least another order of magnitude.

Section G summarizes the trajectory and orbit determination support given the *Pioneer IX* Project during the early phases of the mission. The actual trajectory achieved is very close to the nominal trajectory as indicated by both an early estimate accomplished with 35 min of two-way doppler data and angle data and by a later estimate utilizing two days of doppler tracking data.

B. Evaluation of Errors in h_{max} on the DPODP Ionosphere Model, *L. M. Webb and B. D. Mulhall*

The double precision orbit determination program (DPODP) includes a model of the ionosphere. The purpose of this model is to calculate the ionospheric refraction of a propagating electromagnetic signal so that the resulting error can be calibrated out of radio tracking data.

To achieve its inherent accuracy, the model requires as input data the following ionospheric parameters:

(1) Scale height.

(2) Maximum density of free electrons.

(3) Altitude of maximum electron density.

The model is being evaluated to determine the error that will result if these parameters are not available and nominal values are used.

Using the formulation of Liu (SPS 37-41, Vol. III, pp. 38–41), the range correction can be written as

$$\Delta R = \left(\frac{B}{39}\right)\left(\frac{2.300}{f}\right)^2\left(\frac{n_{max}}{5\times 10^{13}}\right)P(\gamma)\,C_H C_D C_L C_S \tag{1}$$

where

ΔR = range correction, m

B = scale height, km

f = signal frequency, GHz

n_{max} = maximum free electron density, electrons/m^3

$P(\gamma)$ = elevation angle factor

γ = elevation angle, deg

C_H = altitude of maximum density factor

C_D = diurnal factor (a function of time)

C_L = geomagnetic field factor (a function of geomagnetic latitude)

C_S = solar activity factor (a function of sun spot number)

and

$$C_H = \sum_{k=0}^{2} a_k(\gamma)\left(\frac{h_{\max}}{200}\right)^k$$

$$a_0(\gamma) = 1.51266 - 0.20397\theta + 0.020460\theta^2$$

$$a_1(\gamma) = -0.63725 + 0.26115\theta - 0.02672\theta^2$$

$$a_2(\gamma) = 0.12459 - 0.05718\theta + 0.00626\theta^2$$

where

$h_{\max}$ = altitude of maximum free electron density, km

$\theta = \gamma/10$

The function of $P(\gamma)$ is given in Table 1 for nominal $h_{\max}$ of 200 km, B of 39 km, f of 2.3 GHz, and $n_{\max}$ of 5×10^{13} electrons/m^3.

Table 1. $P(\gamma)$ versus γ

γ, deg	$P(\gamma)$	γ, deg	$P(\gamma)$
0	23.435	20	14.396
1	23.387	30	11.138
2	23.222	40	9.134
3	22.954	50	7.869
4	22.598	60	7.061
5	22.169	70	6.561
10	19.458	80	6.286
15	16.706	90	6.197

To evaluate C_H, nominal values were selected for B, f, and $n_{\max}$. The factors C_D, C_L, and C_S were also held constant. The elevation angle was set at zero since this maximizes the effect of the ionosphere. The C_H factor depends on elevation angle and $h_{\max}$. The elevation angle is a function of the trajectory and is available within the DPODP. On the other hand, either $h_{\max}$ must be determined from outside sources or a nominal value assumed. Figure 1 shows the error in range correction caused by assuming nominal values of $h_{\max}$. Typically, $h_{\max}$ lies between 200 and 450 km (Ref. 1). Consequently, the error curves are restricted to the upper and lower practical limits of $h_{\max}$ as indicated by the dashed lines.

The maximum absolute error in range correction is 8.7% for an 80% error in $h_{\max}$ (Fig. 1).

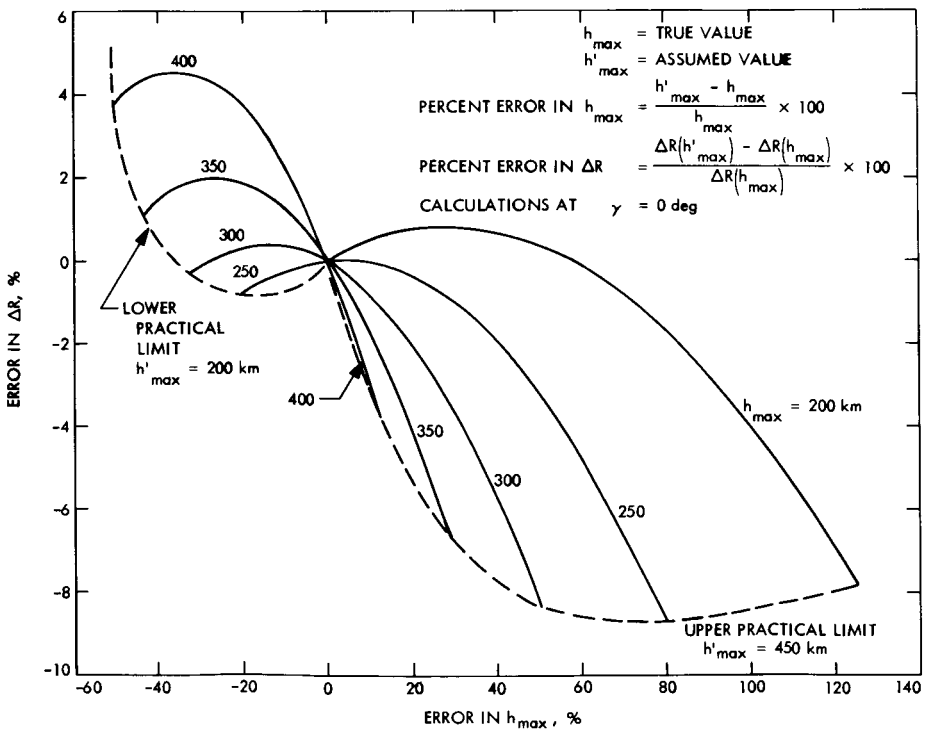

Fig. 1. Error in ΔR due to $h_{\max}$

The quantity h_{max} is calculated from ionosonde data by the Environmental Science Services Administration (ESSA), Boulder, Colo. Ionosonde data are available from stations scattered all over the world. However, the data must be air mailed to ESSA for analysis and reduction before h_{max} can be calculated. Thus, obtaining h_{max} in near real time to correct tracking data for mission operation is not promising. A nominal value will probably have to be used for real-time operations.

Evaluation of the diurnal, geomagnetic, and solar activity factors is in progress. When completed, the accuracy of the total model can be determined and at that point the relative effect of the error which results from assuming a nominal h_{max} will be evaluated.

Reference

1. Wright, J. W., *Mean Electron Density Variation of the Quiet Ionosphere*, NBS TN 40-13. National Bureau of Standards, Boulder, Colo., Apr. 15, 1962.

C. Conversion of Faraday Rotation Data to Ionospheric Measurements,

B. D. Mulhall and K. L. Thuleen

1. Introduction

In support of the *Pioneer VI* Faraday rotation solar occultation experiment of Levy, Stelzried, and Seidel (SPS 37-53, Vol. II, pp. 69–71), a computer program has been developed to process the Faraday rotation measurements of the earth's ionosphere made at the Venus site so that they can be used to remove the ionospheric effect from the experimental data. This program can also be used in spacecraft orbit determination work to compute a correction to radio tracking data so that the ionospheric effect can be calibrated.

2. Faraday Rotation

Radio waves of a frequency great enough to penetrate the ionosphere are subject to phase-path length change, refraction, group-path delay, absorption, and polarization rotation. If the radio wave is linearly polarized and the plane of polarization at the point of origin is known, the rotation of polarization due to the Faraday effect can be determined by measuring the polarization of the received signal.

The *Applications Technology Satellite 1* (ATS-1) is a spacecraft in a geostationary orbit over the Pacific Ocean that transmits a linearly polarized signal which can be received at the Goldstone Deep Space Communication Complex. The polarization of the ATS-1 signal is continuously measured, digitized, and recorded. Using the method described in *Subsection 6*, Faraday rotation data can be converted to a measurement of electron content and used to calibrate the earth's ionosphere over a complete diurnal cycle.

3. Original Data

The polarization measuring device determines rotations from 0 to 180 deg and then retraces back to 0 deg. Samples are digitized every second and averaged over one minute. Due to noise, the values recorded near 0 or 180 deg contain samples from both sides of the retrace.

For example, the original record of a constantly increasing ionosphere appears to be a series of alternate increases (from 0 to 180 deg) and decreases (from 180 to 0 deg). The decreases are actually retraces; however, experience is required before retraces in the original record can be distinguished from actual decreases in the measured value.

Figures 2, 3, and 4 show original data records and reconstructed data (electron content in electrons/m$^2 \times 10^{17}$). The nighttime reading of the ionosphere is fairly constant (Fig. 2). However, the original data may stay very near the retrace point for a long period of time (Fig. 3). Noise causes the original data to fluctuate wildly when the actual measurement remains nearly constant (within a few degrees of the retrace point).

Another difficult situation arises when the midday peak occurs at the retrace point. Multiple retraces will occur and appear as rapid changes (both increases and decreases) between 0 and 180 deg when the actual measurement remains almost constant. Figure 3 shows two double retraces, one at 16:00 GMT and a second at 17:15.

If a retrace is not detected, the electron content will be in error by 5×10^{16} electrons/m^2. This is a 20% error on a typical day.

4. Methods for Detecting Retraces

No single retrace detection scheme is effective because of the varying characteristics of the ionosphere during the day. For example, the electron content remains very nearly constant throughout the night and increases in the morning, reaching a peak between noon and 3:00 p.m.

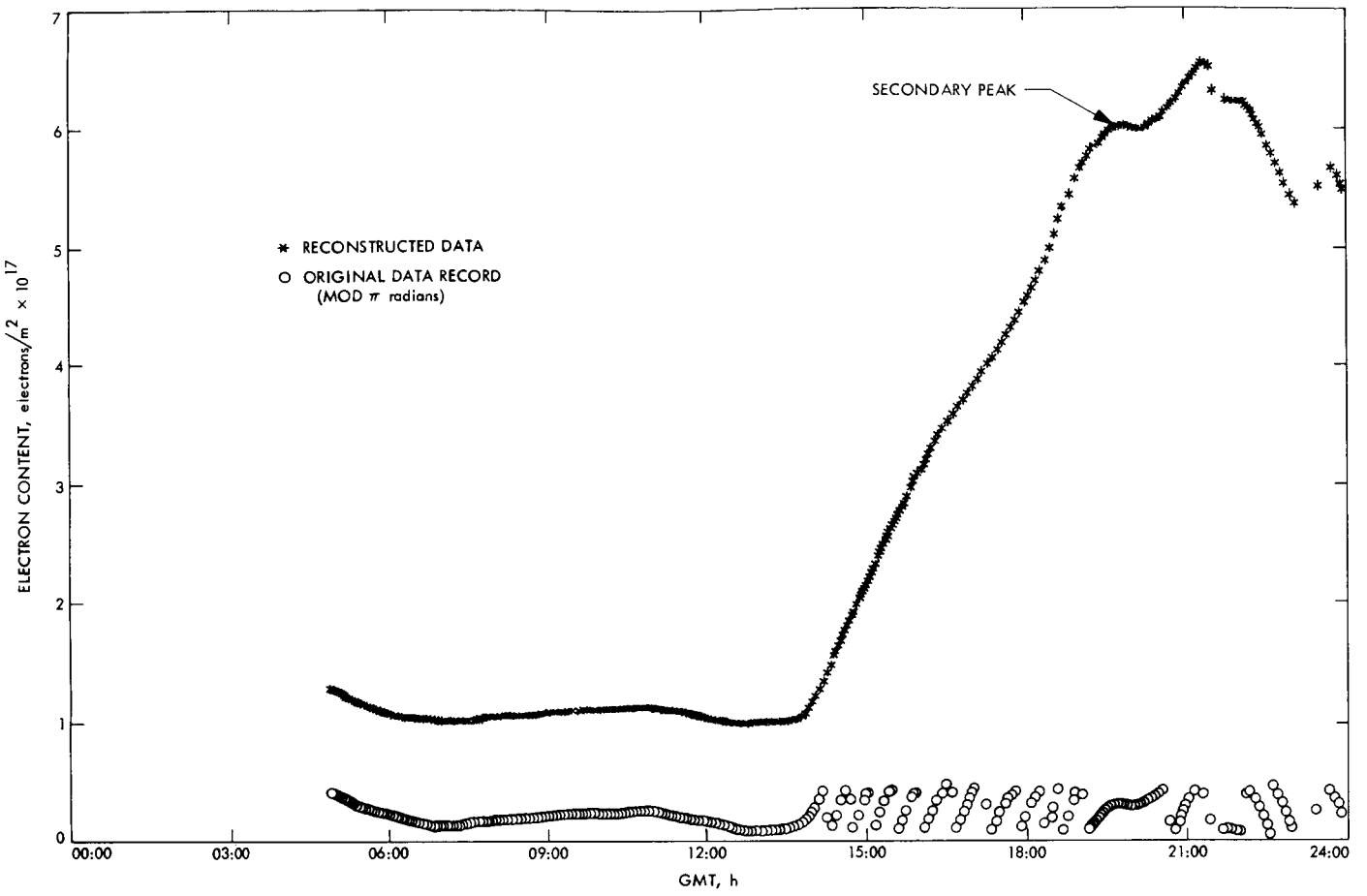

Fig. 2. Faraday rotation data: Oct. 24, 1968

(Figs. 2, 3, and 4). The content then decreases as the free electrons and ions recombine into neutral atoms.

Consequently, the method used to detect retraces in the data varies with the time of day. Four time areas have been defined, each with its own scheme: night (I), morning (II), midday (III), and afternoon (IV). Although different standards are set to distinguish between changes in content and retraces for each of these time areas, the basic logic of the program is the same throughout the day. All data are tested against the criteria for the time area in which they were recorded. Any out-of-tolerance data point initiates a retrace test. This test is continued until three consecutive points are within tolerance.

All out-of-tolerance points (the points collected while the retrace test was in progress) are evaluated as a group. If the group fails to pass, it is rejected as a retrace, a quadratic polynomial is fitted through the resulting gap, and one half rotation added to or subtracted from subsequent data. If the group passes, it is all accepted as valid data and no adjustment of absolute level is made.

Quantities used for testing are

$$CSL = \frac{x_n - x_{n-1}}{t_n - t_{n-1}}$$

$$XCUR = |x_a - x_n|$$

$$TXCUR = |t_a - t_n|$$

where

CSL = current slope

$XCUR$ = excursion value

$TXCUR$ = time of excursion

x_n = nth data point

t_n = time x_n was recorded

x_a = last accepted data point

t_a = time of x_a

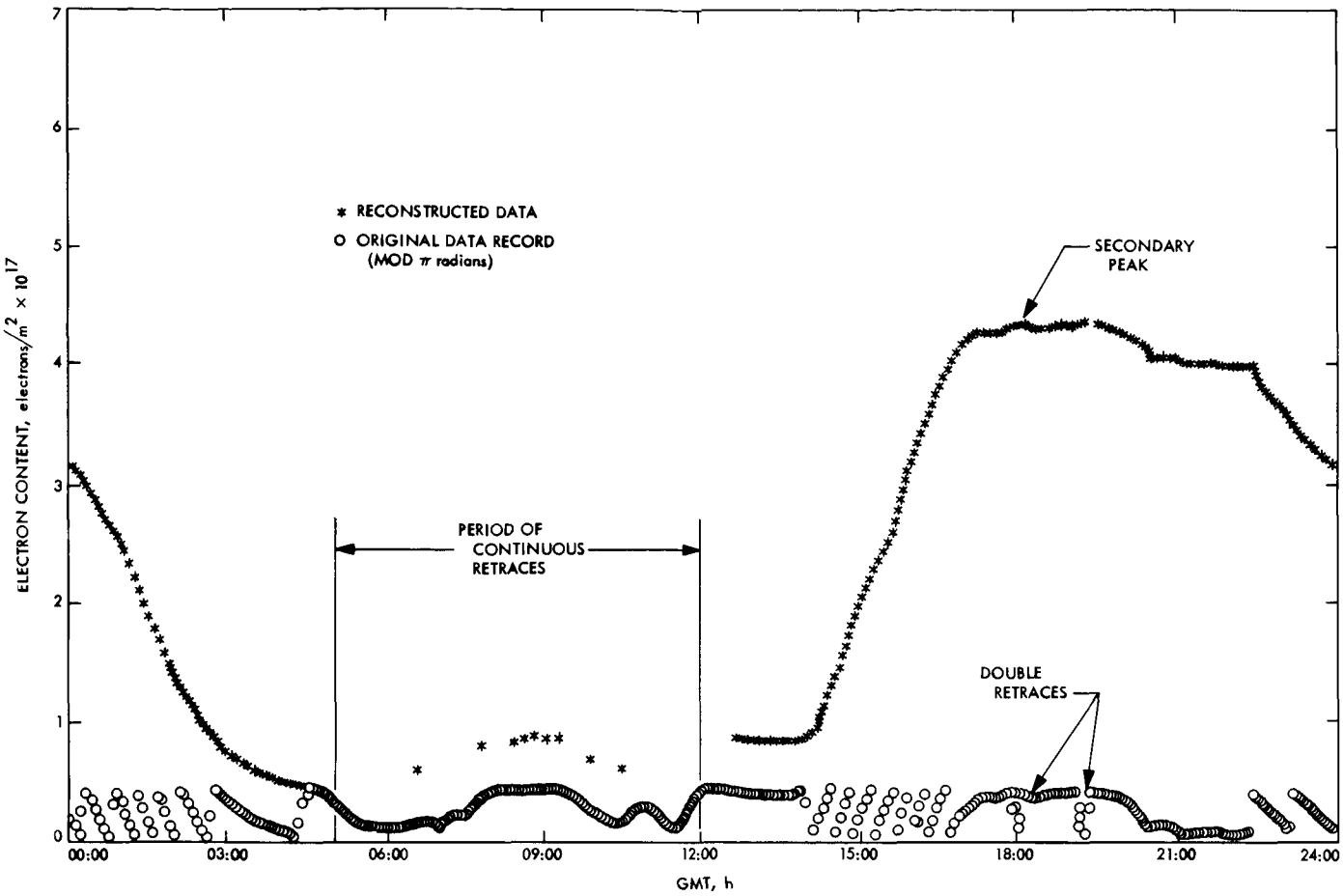

Fig. 3. Faraday rotation data: Nov. 7, 1968

The strategy used in each of the time areas is as follows:

Time area I. During this period (10:00 p.m. to 5:00 a.m. local time), the electron content is at minimum value and its rate of change is quite slow. Points encountered here are tested for current slope. If the absolute value of the slope exceeds 250 deg of rotation/h, the point is considered questionable and a retrace test is initiated. If the excursion over the entire retrace test exceeds 90 deg of rotation, it is considered a retrace.

Time areas II and IV. During time areas II (5:00 to 9:00 a.m.) and IV (4:00 to 10:00 p.m. local time), the electron content is steadily increasing and steadily decreasing, respectively. Points encountered in these areas are tested on the sign of the current slope. If the sign is not in agreement with the predicted sign, the point is considered questionable. Each successive point is tested for a retrace. The excursion is computed and, if it exceeds 90 deg of rotation, a retrace is detected.

Time area III. During time area III (9:00 a.m. to 4:00 p.m. local time), the electron content reaches maximum value. Frequently, secondary peaks occur (Figs. 2 and 3); therefore a test of the sign of the current slope is not adequate since both increases and decreases may occur in any order. This time area is the most difficult in which to assign definite characteristics. For this reason the testing is more extensive and complex than in the other time areas.

Points in this area are tested initially on the absolute value of the current slope. It is assumed that any point giving an absolute value less than 667 deg of rotation/h is valid data. This is a larger maximum slope than that used in area I. A point not passing this test is held as questionable, along with successive points.

Successive data is tested by computing the excursion and the time of excursion for each point received. If the excursion exceeds 90 deg and if the time of excursion is

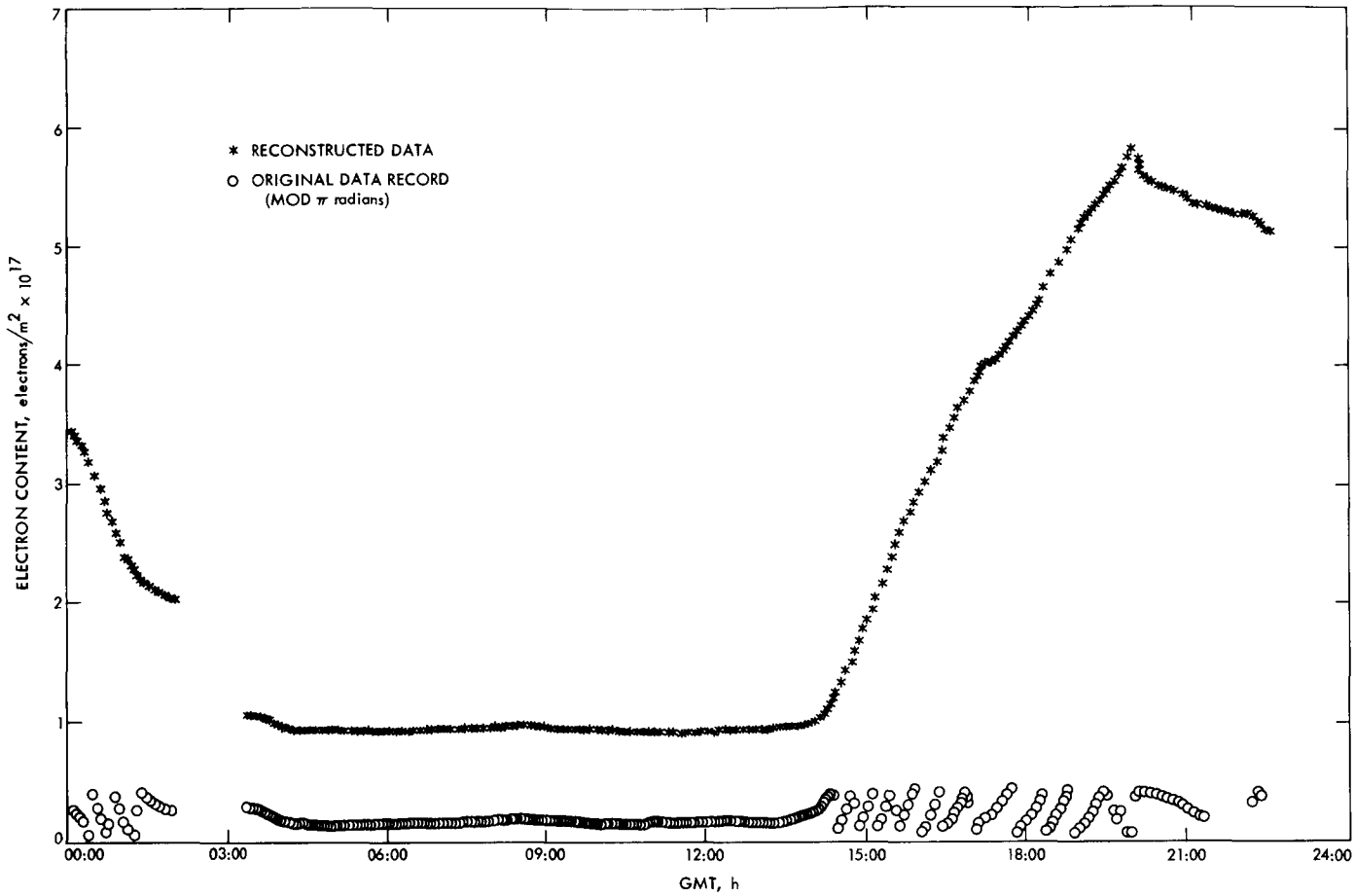

Fig. 4. Faraday rotation data: Nov. 20, 1968

not greater than 10 min, the data group is considered a retrace. If both of these criteria are met, the group of data is considered valid.

5. Establishing the Absolute Level

As part of the initialization process, the program consults the DPODP ionosphere model (see Webb and Mulhall, *Section B*) to determine the absolute electron content. This absolute level is used as the starting point. Retraces are then used to add or subtract levels as the day progresses. If a large data gap occurs, the program reinitializes processing and the model is used to determine the absolute level.

The program will accept data records starting at any time of day, take the predicted electron content provided by the model, and process data with this starting point. The program checks to ensure that, as retrace levels are subtracted, the absolute level never falls below a minimum specified value. If this minimum is reached, the program considers the starting level provided by the model to be in error, and reprocesses all previous data, adding in one retrace level to all the measurements.

An additional check is made to assure that the model has not predicted the ionosphere at too high a starting level. The ionosphere is least active early in the morning (about 2:00 a.m. local time). Consequently, the model predicts the ionosphere most accurately at that hour. As the data record reaches 2:00 a.m., the program checks the absolute level against a new estimate provided by the model. This new estimate is used in preference to the original one. All previously processed data are adjusted by the number of half-rotation levels by which the two estimates were in disagreement.

6. Conversion to Electron Content

When all retraces have been eliminated from the original data, the electron content is computed. It has been shown (Ref. 1) that the rotation (Ω) in radians of the plane

of polarization of a linearly polarized electromagnetic wave due to the Faraday effect is

$$\Omega = \frac{Q}{f^2} \int_{\text{ray}} NH \cos\theta \, ds \tag{1}$$

where

$Q = 2.97 \times 10^{-2}$ (in mks units)

$f =$ wave frequency, Hz

$H =$ magnetic field intensity, Amp-turns/m

$\theta =$ angle between wave normal and magnetic field

$N =$ electron density, electrons/m^3

$ds =$ differential element of path length

$$ds = \sec\zeta \, dh \tag{2}$$

where

$h =$ altitude, km

$\zeta =$ zenith angle

To determine the integrated electron content along the path $H \cos\theta \sec\zeta$ must be determined or approximated. A convenient approximation that is frequently used is to take the average value M_{avg}, where

$$M_{avg} = (H \cos\theta \sec\zeta)_{avg} \tag{3}$$

Yeh and Gonzalez (Ref. 2) have found that M_{avg} is generally equal to the value of $H \cos\theta \sec\zeta$ calculated for an altitude of 340 to 400 km. The program uses the value of M computed for 400 km to determine the vertical columnar electron content.

$$\int N \, dh = \frac{f^2}{QM_{400}} \Omega \tag{4}$$

The value of M is computed by a subroutine written by R. H. Eckhouse, Jr.,[1] which was made available by Dr. K. C. Yeh of the University of Illinois. The subroutine uses the method of Jones and Melotte (Ref. 3) to perform a spherical harmonic expansion of the earth's magnetic field. The 48 coefficients of Jensen and Cain (Ref. 4) are used, which result in terms of the sixth order.

[1]NASA Contract NSG 24-59.

7. Correction for Spacecraft Line of Sight

The electron content must be referenced to the spacecraft line of sight from the tracking station so that the ionospheric effect on the received signal can be calculated. This is done by computing the spacecraft subionosphere point (the point on the earth's surface directly below the point where the radio signal ray path is 400 km above the earth's surface) as a function of time throughout the pass. This calculation is performed as described in *Section D* by Mulhall and Wimberly.

The electron content is then scaled for the differences in geomagnetic field, elevation angle, and ray-path length through the ionosphere. Finally, Eq. (4) is used to compute the Faraday rotation of the *Pioneer* S-band frequency so that the rotations of the *Pioneer* signal caused by the ionosphere can be removed from the experimental data.

References

1. Lawrence, R. S., Little, C. G., and Chivers, H. J. A., "A Survey of the Ionospheric Effects Upon Earth-Space Radio Propagation," *IEEE Proc.*, pp. 4–27, Jan. 1964.
2. Yeh, K. C., and Gonzalez, V. H., "Note on the Geometry of the Earth Magnetic Field Useful to Faraday Effect Experiments," *J. Geophys. Res.*, Vol. 65, pp. 3209–3214, 1960.
3. Jones, H. S., and Melotte, P. F., "The Harmonic Analysis of the Earth's Magnetic Field, for Epoch 1942," *Monthly Notices Roy. Astron. Soc., Geophys. Suppl.*, Vol. 6, p. 409, 1953.
4. Jensen, D. C., and Cain, J. C., "An Interim Geomagnetic Field," *J. Geophys. Res.*, Vol. 67, p. 3568, 1962.

D. Conversion of Ionospheric Measurements to Doppler Correction for Deep Space Probe Tracking Data, *B. D. Mulhall and R. N. Wimberly*

1. Introduction

As part of the Precision Navigation Project (PNP), the task of developing techniques and software to calibrate radio tracking data for the ionospheric refraction has been undertaken. The corrections for the ionosphere will be applied to *Mariner IV* encounter, *Mariner V* cruise and encounter, and *Pioneer* tracking data in support of the station locations improvement effort for the PNP. Capability is also being developed to calibrate the ionospheric effect on tracking data in real time for *Mariner* Mars 1969 mission operations.

Three methods for calibrating the ionospheric effect are currently in use. These include the use of two different measurements of the ionosphere and a computer

model. The two types of measurements being used to correct the *Mariner* and *Pioneer* post mission data are ionosonde data and Faraday rotation data.

Ionosonde data are collected by the Environmental Science Services Administration (ESSA), Boulder, Colo., from stations throughout the world. These data provide a measure of the maximum free electron concentration (n_{max}), the altitude (h_{max}) at which it occurs, and a profile of the lower portion of the distribution of free electrons in the ionosphere. Upon request, ESSA research laboratories will compute the entire integrated electron content based on the ionosonde measurement and a model of the upper portion (above h_{max}) of the ionosphere.

Faraday rotation measurements have been made by Stanford University since 1964. Recently, a device was set up by JPL at the Venus site to make Faraday rotation observations of the ionosphere (SPS 37-53, Vol. II, pp. 69–71, and *Section C*, above). This technique provides a measure of the total columnar content of free electrons between the observer and a spacecraft. By monitoring the signal from a geostationary satellite, the full diurnal variation of the ionosphere can be observed.

In addition to measurements, a model of the ionosphere can be used to calibrate its effect. The model proves useful to fill in the gaps in data when no measurements are available.

The program described in this article has been developed to provide the capability to calibrate tracking data for ionospheric effect based on either ionosonde data, Faraday rotation measurements, or a model of the ionosphere.

2. Calculations

To use ionosonde or Faraday rotation measurements to calibrate tracking data, certain calculations are required. The measurement must be adjusted for the differences between the columnar electron content where the measurement was made and the columnar content through which the spacecraft's radio signal passed along the spacecraft–station line of sight. The adjustments that are calculated are those due to differences in geographic location, ray-path length through the ionosphere, elevation angle, and geomagnetic field strength.

To relate ionospheric measurements to tracking data, subionosphere points are calculated for both the measurement and the probe–station line of sight. The subionosphere point is defined as the point on the earth's surface directly below the point where the radio signal ray path is at an altitude of 400 km. Yeh and Gonzalez (Ref. 1) have shown that the geomagnetic field strength at 400 km is generally equal to the average field strength. This makes 400 km a very useful reference point for ionospheric calculations. Computing the subionosphere point of the tracking station with respect to the probe is the first step in solving for the ionospheric effect on the tracking data. The subionosphere point for the probe is computed from (see Fig. 5)

$$\mathbf{R} = \boldsymbol{\rho} + \mathbf{r}$$

$$\mathbf{r} = r \begin{bmatrix} \cos\lambda_s \cos\phi_s \\ \sin\lambda_s \cos\phi_s \\ \sin\phi_s \end{bmatrix}$$

$$\boldsymbol{\rho} = \rho \begin{bmatrix} \cos(\lambda_s - HA)\cos\delta \\ \sin(\lambda_s - HA)\cos\delta \\ \sin\delta \end{bmatrix}$$

$$\mathbf{R} = R \begin{bmatrix} \cos\lambda_p \cos\phi_p \\ \sin\lambda_p \cos\phi_p \\ \sin\phi_p \end{bmatrix}$$

where

$\mathbf{R}$ = vector from center of earth to subionosphere point

$|\mathbf{R}| = R = h + R_e$, and $h = 400$ km, R_e = earth's radius

$\boldsymbol{\rho}$ = vector from station to subionosphere point

$|\boldsymbol{\rho}| = \rho = -R_e \sin\gamma + (2hR_e + h^2 + R_e^2 \sin^2\gamma)^{1/2}$, and γ = elevation angle of probe

$\mathbf{r}$ = vector from center of earth to station

$|\mathbf{r}| = R_e$

λ_s = station longitude

ϕ_s = station latitude

HA = probe's topocentric hour angle

δ = probe's topocentric declination

λ_p = longitude of subionosphere point

ϕ_p = latitude of subionosphere point

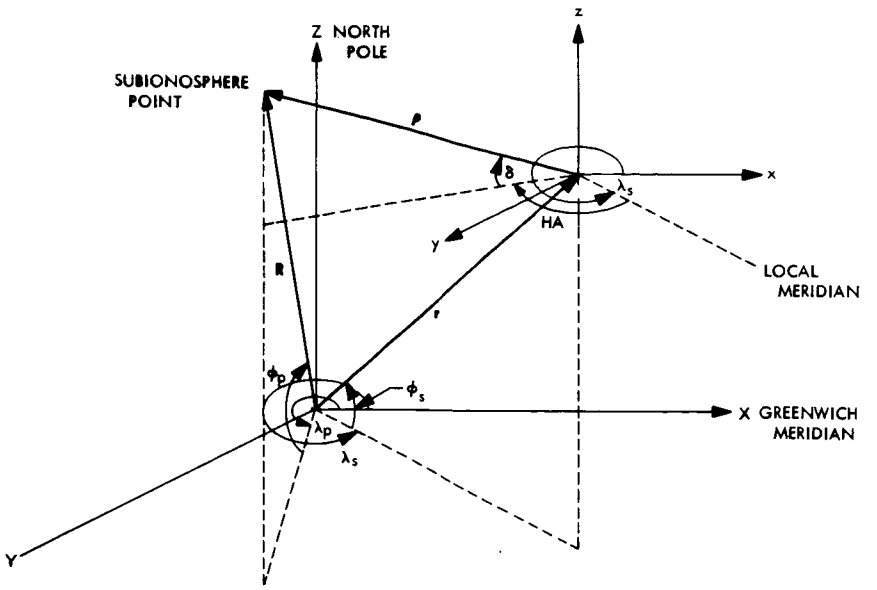

Fig. 5. Calculation of subionosphere point

$$\lambda_p = \tan^{-1}\left[\frac{\rho \sin(\lambda_s - HA)\cos\delta + R_e \sin\lambda_s \cos\phi_s}{\rho\cos(\lambda_s - HA)\cos\delta + R_e\cos\lambda_s\cos\phi_s}\right]$$

$$\phi_p = \sin^{-1}\left[\frac{1}{R}(\rho\sin\delta + R_e\sin\phi_s)\right]$$

The difference in longitude of the geographic locations of the ionospheric measurement and the probe's subionosphere point must be calculated to correlate the measurement time with the time the probe's tracking data was recorded. The measurements are stored in two arrays in the program. One array contains the measurements and the other the measurement times. For convenience, several days of data can be stored at one time.

With the computed difference in longitudes between the probe's subionosphere point and the measurement, a time vector is determined by entering the measurement time array. The subscripts of the time vector (the measurement time closest to the desired time) are found and used to select the corresponding measurement. A linear interpolation is performed to bring the measurement as close to the desired time as possible. By using this time vector technique, measurements need not be spaced at regular intervals. The sample time of ionospheric measurements can be changed as the time derivative of ionospheric electron content changes.

The double precision orbit determination program (DPODP) ionosphere model is used to adjust the measurement for differences in geomagnetic field strength, ray-path length, and elevation angle.

The geomagnetic adjustment is based on the ionosphere model geomagnetic field factor

$$C_L = 3\left(\frac{1}{2} - \left|\frac{\phi_M}{\pi}\right|\right)$$

where

C_L = geomagnetic field factor

ϕ_M = geomagnetic latitude

The geomagnetic latitude is computed for the measurement and the probe's subionosphere point. The adjustment is made by taking the ratio of C_L for the probe over C_L for the measurement.

Similarly the elevation angle difference is adjusted by the ratios of the $P(\gamma)$ and C_H factors in the ionosphere model described by Webb and Mulhall in *Section B*.

3. Conversion to Doppler Correction

The measured ionosphere is used to compute a correction to continuously counted coherent two-way doppler (f_2). From Fig. 6 it can be seen that the correction for one sample of f_2 taken over a count time of T_c, involves

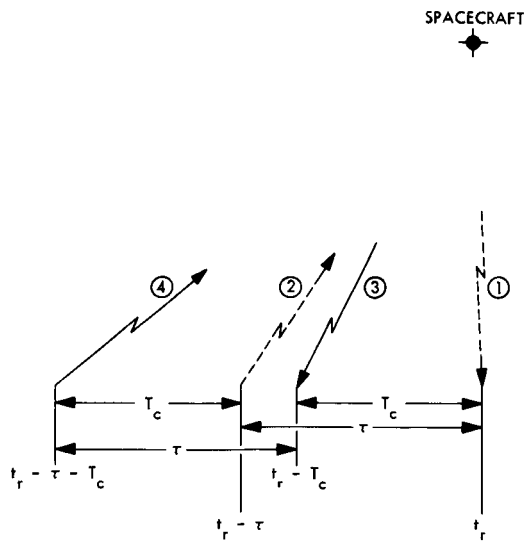

Fig. 6. Calculation of Δf_2

the error in range $\Delta\rho$, resulting from four passes through the ionosphere. These are:

(1) The down-link pass at the end of the count time (received at t_r).

(2) The up-link pass corresponding to (1) (transmitted at $t_r - \tau$, where τ is the round-trip time).

(3) The down-link pass at the start of T_c (received at $t_r - T_c$).

(4) The up-link pass corresponding to (3) (transmitted at $t_r - \tau - T_c$).

The correction in hertz is then

$$\Delta f_2 = \frac{1}{2T_c}\{[\Delta\rho_{\mathrm{up}}(t_r - \tau) + \Delta\rho_{\mathrm{dn}}(t_r)] - [\Delta\rho_{\mathrm{up}}(t_r - \tau - T_c) + \Delta\rho_{\mathrm{dn}}(t_r - T_c)]\} \cdot \left(\frac{f}{c}\right) \tag{1}$$

where

f = received carrier frequency, Hz

c = speed of light, m/s

For operational convenience the program computes the correction independent of the actual time a sample was recorded (t_r). Instead an arbitrarily selected time t_r' is used in Eq. (1). The values of T_c, f, and τ must be entered as input data.

The program computes the correction Δf_2 and produces punched cards formatted so that they can be used directly as control cards for the orbit data generator (ODG) program. The format of these cards is described in Ref. 2.

The Δf_2 correction is rounded off to 10^{-4} Hz. Consequently, an error is introduced that is usually a bias error for the period that one correction is specified. Over an entire pass, this error becomes a low-frequency noise term. A technique[2] has been employed to reduce the error in Δf_2. The program computes the integrated error

$$E = \sum_{i=1}^{N} \epsilon_i \, \Delta t$$

where

E = integrated error, cycles

N = number of times Δf_2 has been computed

ϵ_i = difference between actual value of Δf_2 and the rounded-off value, Hz

Δt = time interval for which Δf_2 is computed and is equal to count time T_c, s

Error bounds are placed on E. If E exceeds the upper bound, the correction is increased by 10^{-4} Hz (see Fig. 7). When E reaches the lower bound the correction is reduced to the original nominal value.

This technique does not totally eliminate the error but increases the frequency of noise, which is a desirable effect since the DPODP is more sensitive to low-frequency noise than to high frequency.

References

1. Yeh, K. C., and Gonzalez, V. H., "Note on the Geometry of the Earth Magnetic Field Useful to Faraday Effect Experiments," *J. Geophys. Res.*, Vol. 65, pp. 3209–3214, 1960.
2. Finfer, M. C., *ODG Users Guide*, JPL Contract 951491. Computer Applications, Inc., Glendale, Calif., Apr. 21, 1967.

[2]Suggested by D. W. Curkendall, JPL Systems Analysis Research Section.

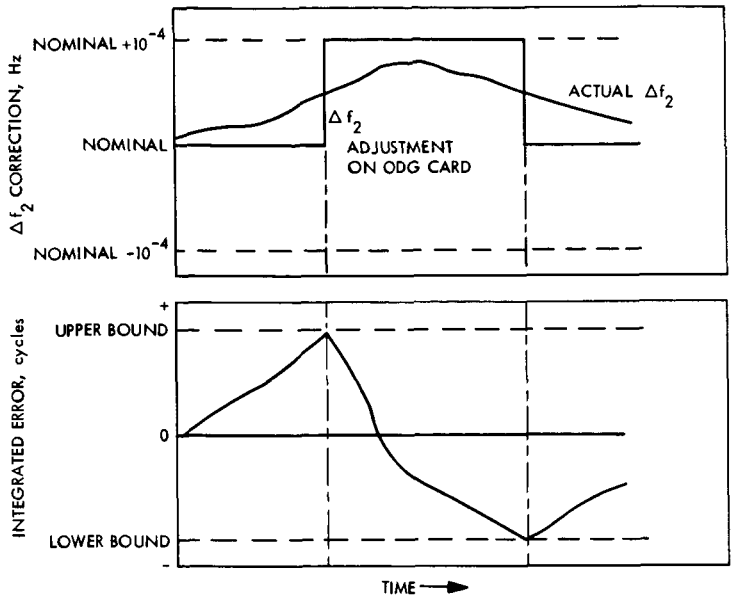

Fig. 7. Δf_2 adjustment

E. *Lunar Orbiter* Gravity Analysis,

P. M. Muller and W. L. Sjogren

Extensive analysis has been proceeding to refine the results in SPS 37-53, Vol. II, pp. 10–16, where qualitative results indicate large gravity anomalies in the ringed maria. Studies include: (1) the effect of J_{20}, C_{22}, and J_{30} on the short arc residuals, (2) the solution for a point mass grid work that best describes the gravity variations using spacecraft at different altitudes over the same lunar surface features, and (3) the presentation of the data to other users.

During the initial studies for invariancy in the doppler residuals, the data from a low eccentricity (0.04) and low inclination (21 deg) orbit were used. In this case the effects of J_{20} and C_{22} (the triaxial moon), as compared to a spherical moon, showed very little difference. However, in the polar orbit the effect is definitely visible and can account for variations in the amplitude of the normalized acceleration signature by as much as 30% (Fig. 8). The signature is approximately the same over the portion from $\pm 50°$ of latitude, but beyond this the signature can vary enormously. A shorter data arc of 50 min was used, and invariancy seemed to hold (Fig. 9).

Another test was made where J_{20} and J_{30} were estimated along with the spacecraft state parameters (C_{22} was left at the nominal value and not estimated since it correlates 0.99 with J_{20} in polar orbit) using a 90-min data arc (Fig. 10). The results compare favorably with the 50-min arc residuals of Fig. 9. The solution for J_{20}, however, was rather low at 1.30×10^{-4} rather than 2.04×10^{-4}. Other solutions at $\approx$15-deg intervals over the front face again give low values for J_{20}. Using orbits covering the back side of the moon where occultation has not occurred (high orbit at $\lambda \approx 140$ deg), the value of J_{20} becomes 2.67. This phenomenon is being investigated with the center-of-gravity offset considered as a possible explanation. The solutions for J_{30} in this same series of runs show a perfect correlation with the ringed maria and/or mascons as expected (Table 2).

At the Aerospace Corp., El Segundo, Calif., using the TRACE program that has the capability of estimating both spherical harmonic coefficients and point mass locations (i.e., mass, radius, latitude, and longitude for 50 points), analysis has shown that the selection of the particular grid of mass points, the *a priori* information used, the parameters estimated, and the set of doppler observables used is a very complicated and interrelated problem.

Table 2. Spherical harmonic coefficient J_{30} vs ringed maria[a]

Mare	$J_{30} \times 10^4$	Latitude, deg
Crisium	1.2	16
Nectaris	−0.7	−15
Serenitatis	0.8	25
Imbrium	1.2	33
Humorum	−0.4	−25
Orientale	−0.3	−20

[a]Data based on one arc from south pole to north pole, 100 km perilune altitude.

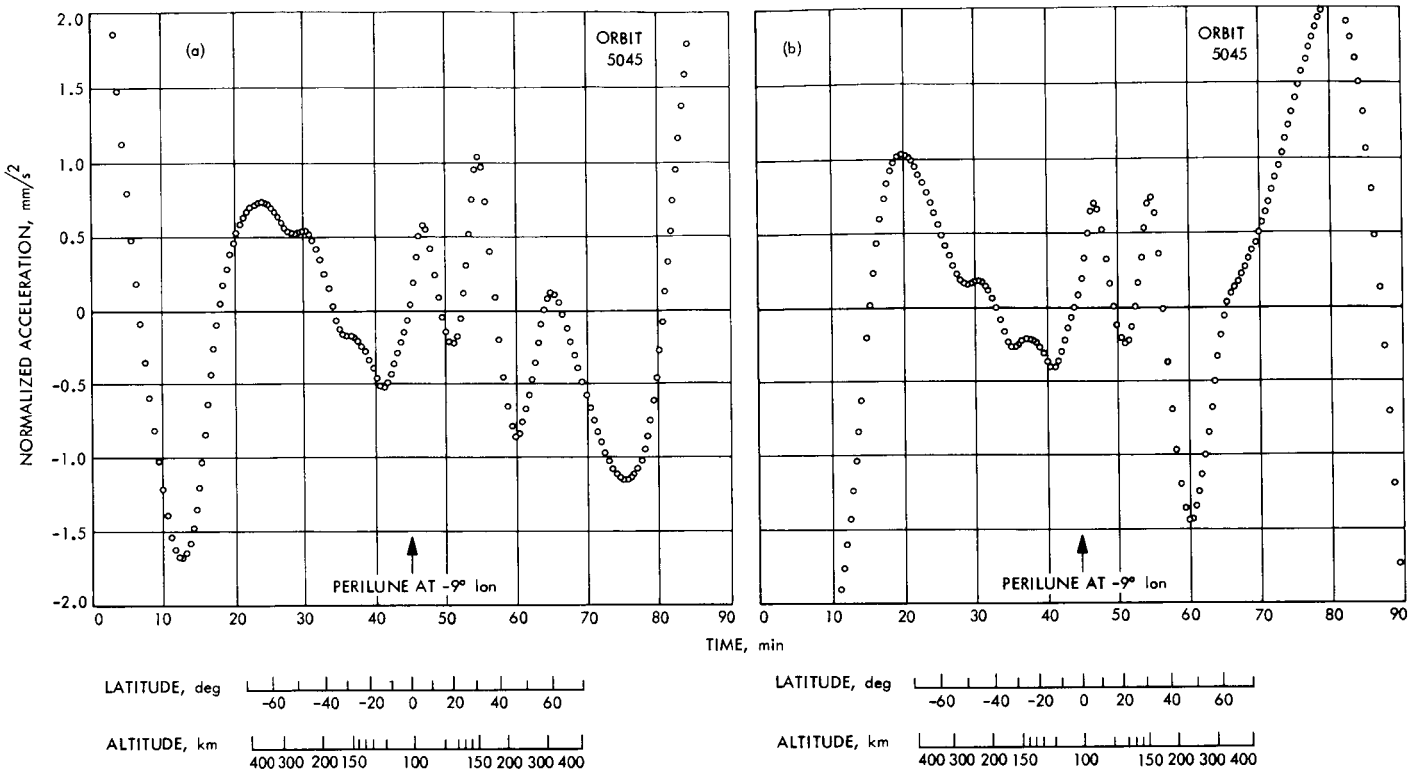

Fig. 8. Acceleration data on *Lunar Orbiter V*-C using 90-min data arc with: (a) triaxial model, (b) point mass model

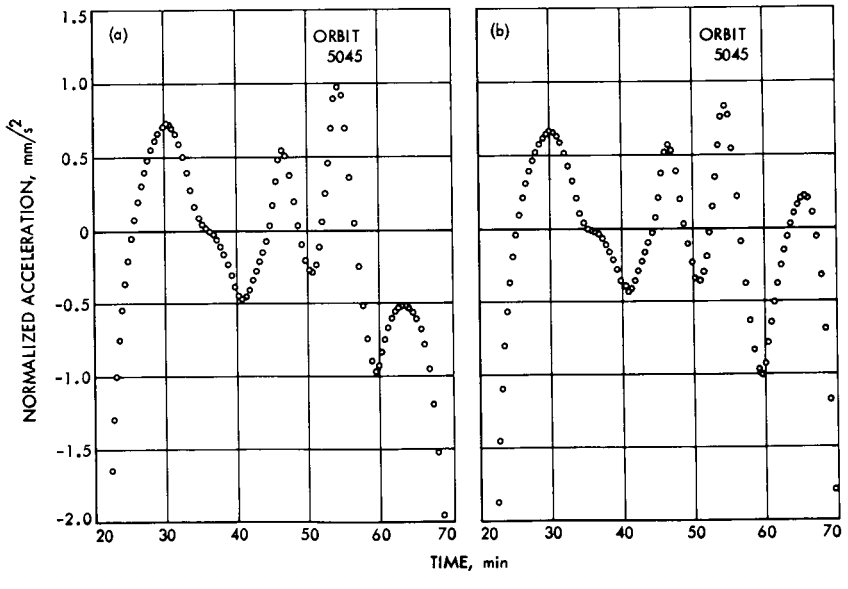

Fig. 9. Acceleration data on *Lunar Orbiter V*-C using 50-min data arc with: (a) triaxial model, (b) point mass model

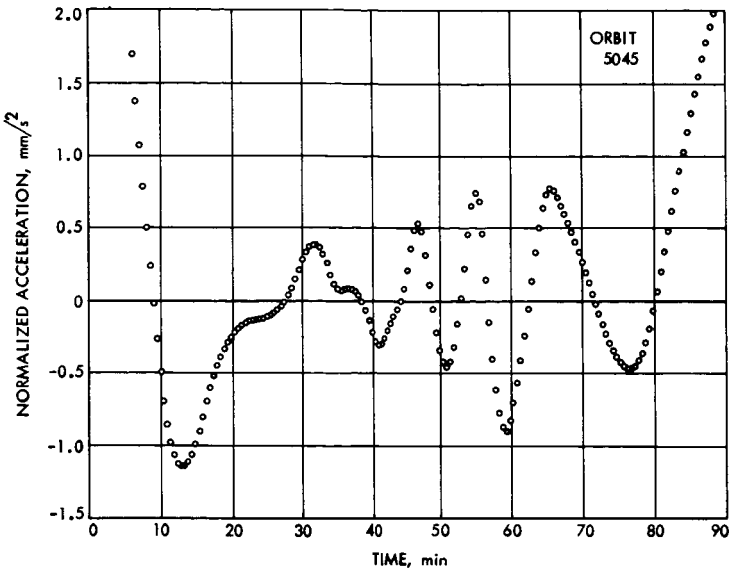

Fig. 10. Acceleration data on *Lunar Orbiter V-C* with J_{20} and J_{30} model

There is emerging a good insight to the proper selection of parameters for a reduction. In collaboration with L. Wong of Aerospace, it now appears that a rather small *a priori* value is required on one position parameter of the spacecraft state, and mass points should be placed at the lunar surface straddled by at least two orbits of data. Consistent relative estimates have been achieved from two different spacecraft over the same terrain. It is planned that within the next few months a complete reduction of this type will be accomplished.

For further analysis by others interested in the data, a reduction is underway and should be completed in January 1969. It includes the reduction of the raw doppler residuals from $\pm 95°$ longitude to $\pm 80°$ latitude, using a point mass moon on a 60-min data arc. The residuals will be fit with patched polynomials so that the derivative of the acceleration curve will be continuous (i.e., the initial reduction was not). The acceleration data will be presented: (1) in a listing as a function of spacecraft altitude, latitude, and longitude at intervals of approximately 1.5° in latitude and longitude, (2) in a listing averaged over 5° squares, (3) in a listing averaged over 10° squares, and (4) in a Mercator projection contour plot.

F. Mass Distributions Inferred From *Lunar Orbiter* Tracking Data, *P. Gottlieb*

The recent work of Muller and Sjogren (Ref. 1 and SPS 37-53, Vol. II, pp. 10–16), correlating line-of-sight *Lunar Orbiter* accelerations with locations on the lunar surface, indicates that the largest *Lunar Orbiter* doppler anomalies are due to concentrations of mass near the surface of the moon. The gravitational effects of these concentrations, called mascons (Ref. 1), can be conveniently represented by spherical masses located between 40 and 150 km below the lunar surface. A model has been constructed that represents the dynamic effects of the largest mascons to within 10%.

The initial model was constructed by placing a mass under the center of each of the largest acceleration areas of Ref. 1 (Maria Imbrium, Serenitatis, Nectaris, and Crisium). The depths for these masses were estimated from the falloff, from each peak, of the acceleration contours. The values of the masses were then chosen to produce the observed peak acceleration. The mass values and peak locations were corrected for viewing angle. Smaller mass values were used to produce the acceleration effects over Mare Humorum and other less defined areas. A total of 36 mass points were used in the initial model.

This initial model was used to integrate trajectories over the most prominent features for short are estimates of spacecraft state (just as was done with the simple triaxial model in Ref. 1). Accelerations were computed from the doppler residuals on these subsequent iterations. These accelerations were then used to slightly modify the magnitudes and locations of the larger masses, or to add new small masses to the model.

The current model has 41 discrete masses. It is being further updated to obtain a more accurate picture of the regions of smaller acceleration areas. The accuracy of the present model can be illustrated by comparing orbit determination (single precision orbit determination program) doppler residuals for computed runs with the simple triaxial model and with the 41 point model.

Figure 11 shows the doppler residuals for a *Lunar Orbiter IV* trajectory, which passes over Mare Serenitatis, after an orbit determination fit with (1) the simple triaxial model, (2) the current 41 mass point model, and (3) the 41 mass points expanded to fifteenth order in spherical harmonics as a smoothing operation. Figure 12 shows the residuals from a typical *Lunar Orbiter V* trajectory passing over Mare Imbrium with a triaxial model and the same trajectory with the current 41 mass point model (smoothed by expanding to fifteenth order in spherical harmonics).

The largest residuals in these figures show a reduction of an order of magnitude when the current model is used. The inherent accuracy of the data should permit a reduction of at least another order of magnitude.

Reference

1. Muller, P. M., and Sjogren, W. L., "Mascons: Lunar Mass Concentrations," *Science*, Vol. 161, pp. 680–684, Aug. 16, 1968.

G. *Pioneer IX* Trajectory and Orbit Determination,

A. Khatib and G. Reynolds

1. Mission Description

The objective of the *Pioneer IX* mission is to collect scientific data within the general region of 0.8 to 1.2 AU from the sun. Scientific measurements will aid in the investigation of the earth's magnetic field, space plasma, cosmic rays, electron density, and other high-density particles and cosmic dust. In addition, solar activity will be investigated during solar occultation 770 days into the mission. Mission design objectives were to have:

(1) A nominal perihelion value of 0.76 AU.

(2) A heliocentric orbit inclination of 0 deg.

(3) A lunar occultation during the first 180 days after launch.

(4) More than one passage through superior conjunction.

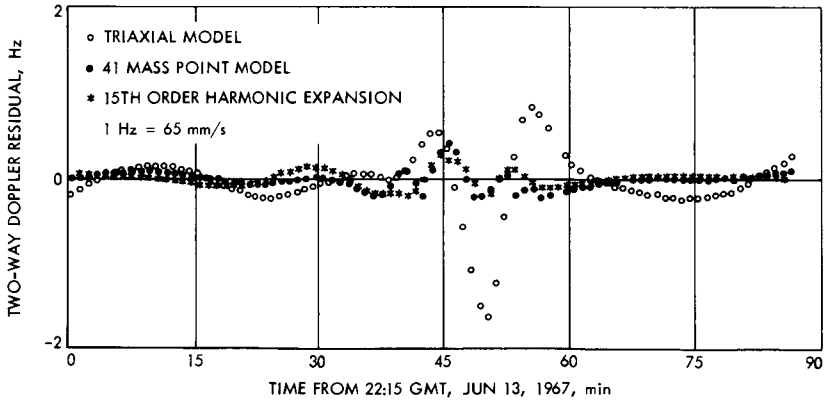

Fig. 11. Residuals over Mare Serenitatis

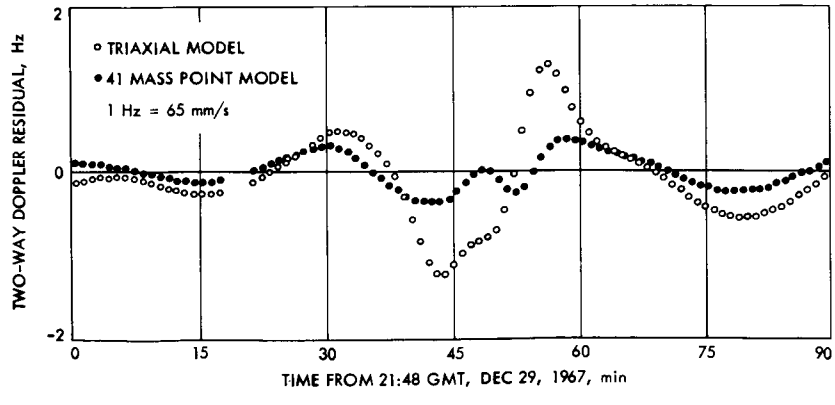

Fig. 12. Residuals over Mare Imbrium

On November 8, 1968, 509 s after the opening of the launch window at 09:38 GMT, *Pioneer D* (*Pioneer IX*) was launched on a very nearly nominal trajectory. After coasting for 670 s in an elliptical parking orbit, the spacecraft was injected into an escape trajectory, and the step I orientation maneuver was begun. This maneuver, performed with sun sensors, placed the spin axis of the spacecraft normal to the sun–probe line to permit maximum output from the solar panels. The step II orientation maneuver, performed during the second pass over the Echo DSS, placed the spin axis of the spacecraft approximately normal to the ecliptic plane. This orientation allows the high-gain antenna to illuminate the earth continuously throughout the mission.

2. Orbit Determination

The first station to view the spacecraft was Johannesburg DSS at 00:26:30 after launch (design value 00:26:21). At 10:12:59 GMT, receiver lock for one-way doppler acquisition was achieved after encountering a 9-s delay. Two-way lock was achieved at 10:30:06 GMT and lasted until the Echo DSS rise at 21:30:02 GMT.

The first estimate of the spacecraft orbit was based on early angle data from Tidbinbilla DSS and Johannesburg DSS, including 35 min of two-way doppler data from the latter. This preliminary orbit (PROR) was computed 3 h after launch. A second early estimate of the spacecraft orbit was made (ICEV) based on an additional hour of doppler data from Johannesburg DSS. These two solutions are shown in Table 3 and compared to the current best estimate of the initial spacecraft orbit (Post 9101). This current orbit (Post 9101) contains two-way doppler data only from acquisition up to the time a partial step II orientation maneuver was begun. As can be seen in Table 3, all three solutions are in close agreement.

On November 9, 1968, 01:30:00 GMT, a command to start a partial step II maneuver was transmitted to the spacecraft from the Echo DSS. This partial maneuver, which was to place the spacecraft spin axis normal to the ecliptic plane, lasted for 90 min. The effect of this orientation on the doppler observables can be readily seen in Fig. 13, which shows a doppler change of 2.5 Hz after completion. This corresponds to a change of 16.7 cm/s in radial velocity. At 23:05:00 GMT of the same date, the final step II maneuver was initiated. The maneuver lasted for 5 h and upon termination the spacecraft was placed in its final orientation which optimized both the solar energy received and the high-gain antenna signals.

Table 3. Estimate of *Pioneer IX* state vector based on initial orbit determinations, epoch 10:07:16.3 GMT, Nov. 8, 1968

State vector[a]	PROR	ICEV	Post 9101
X, km	−6812.9889	−6814.3257	−6815.4811
Y, km	504.7417	502.9972	502.4691
Z, km	−366.8079	−363.4530	−368.2250
$\dot{X}$, m/s	−744.4980	−744.2672	−738.3623
$\dot{Y}$, m/s	−9056.1595	−9055.8865	−9054.3559
$\dot{Z}$, m/s	−6267.5175	−6266.4689	−6267.6209

[a]Coordinate system is geocentric equatorial inertial of date.

Because of discontinuities introduced to the spacecraft trajectory due to step II orientations, the state vector at the end of step II orientation maneuvers was calculated based on pre-step II and post-step II data and the solutions compared in Table 4. The computed difference in radial velocity between the two solutions is 44.25 cm/s, which is in close agreement with the total doppler shift of 6.5 Hz or 43.3 cm/s observed in Figs. 13 and 14 covering both parts of the step II orientation maneuver.

Table 4. Estimate of *Pioneer IX* state vector pre- and post-step II maneuvers for epoch 05:00:00 GMT, Nov. 10, 1968

State vector[a]	Post 9101	Post 9202
X, km	402625.45	402603.44
Y, km	−235748.37	−235748.16
Z, km	−118808.43	−118804.28
$\dot{X}$, m/s	2280.9663	2280.6133
$\dot{Y}$, m/s	−1182.3424	−1182.4626
$\dot{Z}$, m/s	−568.2934	−567.4705
$\dot{r}$, m/s	2626.6743	2626.2318

[a]Coordinate system is geocentric equatorial inertial of date.

3. Actual Trajectory

The actual *Pioneer IX* trajectory was so close to the nominal one targeted by McDonnell Douglas engineers that the preflight nominal predicts could be used for initial acquisition and no search patterns were required. Tables 5 and 6 show a comparison of the important trajectory and mission parameters.

Table 5. Elements of the escape hyperbola

Parameter	Nominal	Actual
C_3 (twice total energy per unit mass), $(km/s)^2$	5.257	5.2655
Semimajor axis, km	−75,816	−75,700
Eccentricity	1.0887	1.0895
Inclination to earth's equator, deg	34.5	34.93
Right ascension of ascending node, deg	348.72	351.04
Argument of perifocus, deg	181.8	181.5
True anomaly at injection, deg	3.82	4.40
Radius of closest approach, km	6832.6	6833.6

Table 6. Elements of the heliocentric orbit

Parameter	Nominal	Actual
Semimajor axis, km	130,509,000	130,502,000
Eccentricity	0.1359	0.13544
Inclination to ecliptic, deg	0.007	0.0871
Longitude of perihelion ($\Omega + \omega$), deg	225.35	229.40
Epoch of perihelion passage	Apr. 5, 1969	Apr. 7, 1969
Epoch of aphelion passage	Sep. 1, 1969	Sep. 3, 1969
Period, days	297.6	297.6
Perihelion distance, km	112,779,000	112,827,000
Aphelion distance, km	148,240,000	148,165,000
Superior conjunction, days from launch	768	770

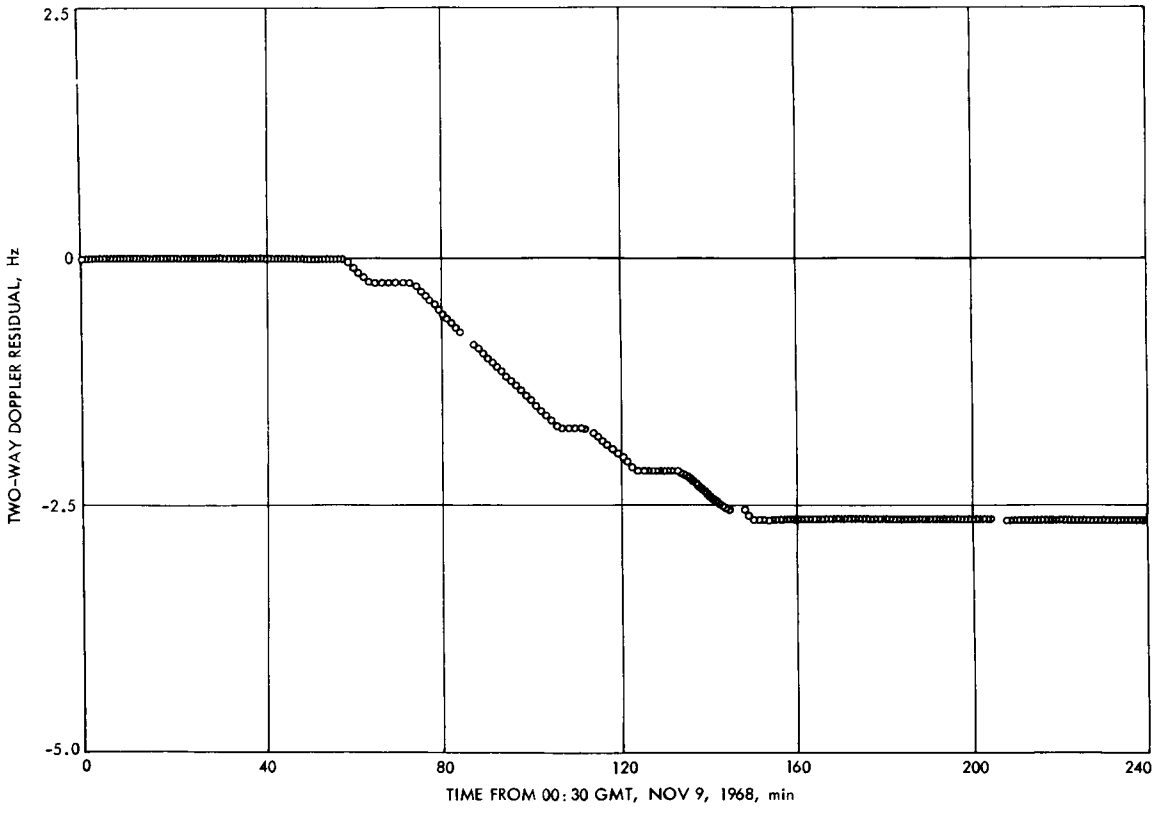

Fig. 13. Doppler residuals during partial step II maneuver over Echo DSS

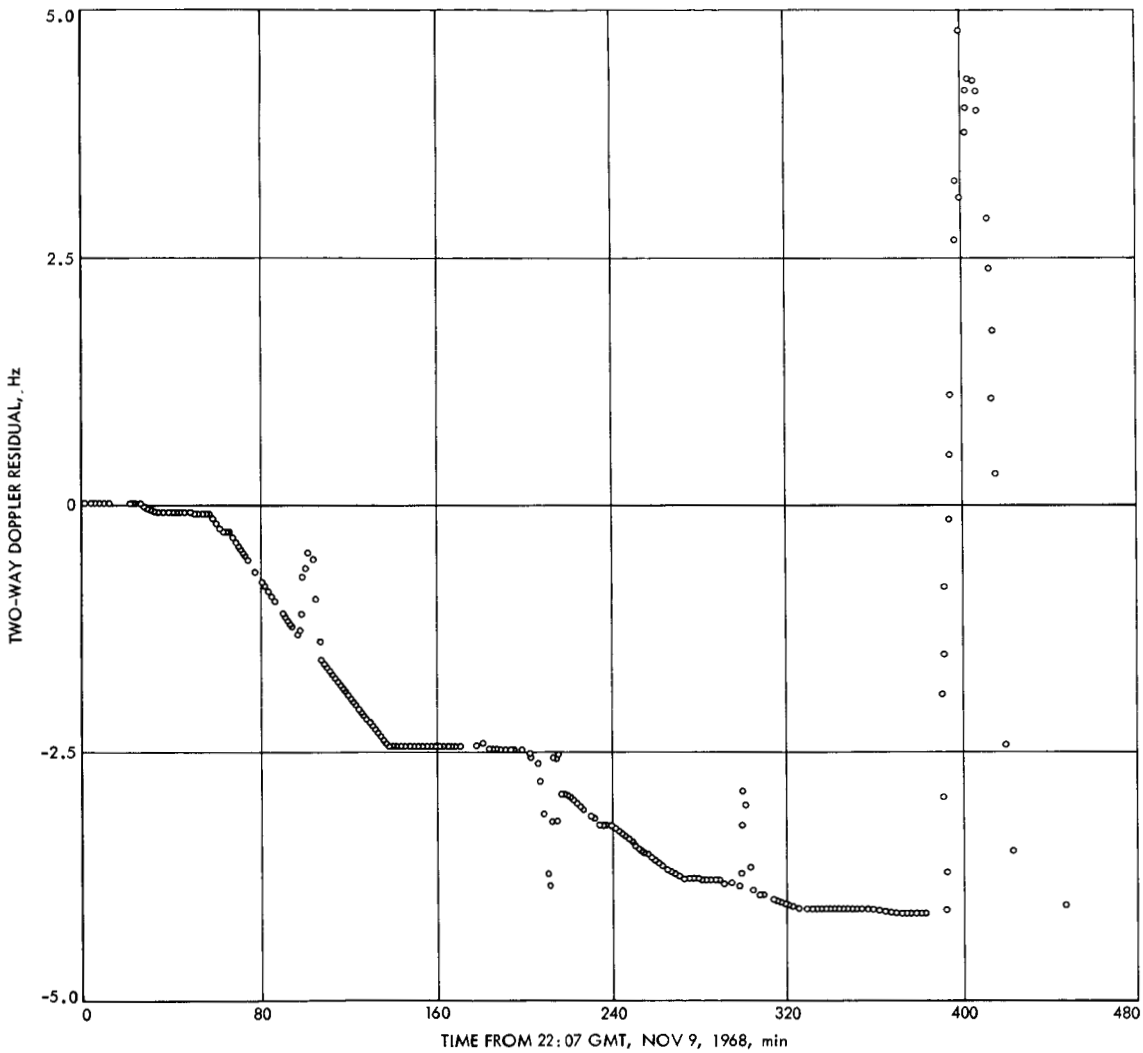

Fig. 14. Doppler residuals during step II maneuver over Echo DSS

IV. Advanced Engineering: Communications Systems Research

A. Low Data Rate Communication: Block-Coded Frequency Shift Keying, *R. M. Goldstein*

1. Introduction

As coherent communication systems are forced to lower signal-to-noise ratios, a point is reached where too much power must be used to establish synchronization; therefore, noncoherent systems appear more efficient.

A good candidate for such a system is block-coded frequency shift keying. In this system, p data bits are collected and then one of 2^p pure carrier tones is transmitted continuously for T sec, while p more bits are being collected. The receiver measures the power spectrum of the signal in order to estimate which tone was transmitted. FSK telemetry has received much attention in the recent literature, and the interested reader is referred to Refs. 1–4, SPS 37-48, Vol. III, pp. 256–264, and SPS 37-50, Vol. III, pp. 338–342. (See also Footnote 1.)

[1]Boyd, D. W., "Performance of FSK Systems With Large Uncertainty in the Carrier Frequency and Linear Envelope Detectors," July 25, 1967 (JPL internal document); Yuen, J. H., "A Note on Practical Design Considerations in Implementing a M-ary Frequency Shift-Keying Communication System," Nov. 15, 1968 (JPL internal document).

This article is concerned with one realization of this signalling method. The receiver is a small computer with an analog-to-digital converter, programmed with the Cooley–Tukey (Ref. 5) fast Fourier transform algorithm. We consider three problems which arise in any practical system: (1) matching of the receiver to the spectral characteristics of the transmitter; (2) utilizing the data stream itself to find the correct timing of the keying and also to track frequency drifts; and (3) computation of the probability of error as a function of all of the system parameters. Finally, we present design charts, so that such systems can be synthesized to fit any desired set of constraints.

2. Spectral Matching

If the tones last T sec, one would ordinarily space them $1/T$ Hz apart. For the cases which we consider as low data rate, however, we must account for the frequency jitter of the transmitter–receiver system. Let the effective spectral width of the transmitted tone be $\widehat{\Delta f}$ Hz. Then the tones must be spaced by at least $\widehat{\Delta f}$. It is easily shown that the best "filter" characteristic of the spectrum analyzer must match the spectral shape of the received tone. A perfect match is not important and, indeed, is probably not possible. However, an approximate match is important, so that $\widehat{\Delta f}$ becomes one of the central parameters of the system design.

Spectral matching is obtained in this system by breaking up each T-sec signal word into k blocks and averaging the k resulting spectra. The filter characteristic is then determined by the time duration of each block.

Let the successive samples of the signal (separated in time by T_0) be x_i. Let each spectrum be computed from N samples. The power spectrum $P(n)$ is then computed according to the formula

$$P(n) = \left| \frac{2}{N} \sum_{i=0}^{N-1} x_i \exp\left(j \frac{2\pi}{N} i n\right) \right|^2,$$

$$n = 0, 1, \cdots, N/2 \tag{1}$$

Figure 1a is a plot of the nth filter response normally provided by the fast Fourier transform to a sine wave signal. The received spectrum can be thought of as observations of the signal through a set of $N/2$ such filters, stagger-tuned across the band.

Although the characteristic of Fig. 1a is quite satisfactory for detection, it does not allow convenient frequency tracking of the signals. We have assumed that all predictable frequency drifts have already been removed (doppler, thermal drift, etc.). However, other drifts will surely remain, and it is necessary to track these in any practical system.

In order to accommodate this requirement, we use twice as many signal samples per spectrum. We then average adjacent points in the power spectrum, which restores the filter characteristic to approximately the same width as before.

$$P(n) = \left| \frac{1}{N} \sum_{i=0}^{2N-1} x_i \exp\left(j \frac{\pi}{N} i n\right) \right|^2 + \left| \frac{1}{N} \sum_{i=1}^{2N-1} x_i \exp\left[j \frac{\pi}{N} i (n+1)\right] \right|^2,$$

$$n = 0, 2, 4, \cdots, N \tag{2}$$

Figure 1b is a plot of this filter characteristic. Use of Eq. (2) instead of Eq. (1) requires only a small increase in the total number of computations because of the nature of the fast Fourier transform. However, it does double the data memory requirements of the computer.

3. Frequency Tracking

If the two terms of Eq. (2) are subtracted, a very satisfactory S-curve is produced for frequency tracking:

$$F_n = \left| \frac{1}{N} \sum_{i=0}^{2N-1} x_i \exp\left(j \frac{\pi}{N} i n\right) \right|^2 - \left| \frac{1}{N} \sum_{i=0}^{2N-1} x_i \exp\left[j \frac{\pi}{N} i (n+1)\right] \right|^2,$$

$$n = 0, 2, 4, \cdots, N \tag{3}$$

Figure 2 is a plot of this S-curve, F_n. Note that very little extra computation is needed, since the terms have already been computed. Operationally, the system works as follows: After each block of T/k sec is received, a power spectrum (Eq. 2) is computed. After k spectra are computed and averaged, the largest $P(n)$ is selected. The corresponding n is the estimate of the transmitted data. The corresponding F_n is an estimate of the current frequency error. It is filtered and used to correct the local oscillator tuning as in any frequency-locked loop.

During initial acquisition, the signal frequency may fall between the effectively stagger-tuned filters of Fig. 1b. In that case the odd values of n must be used in Eqs. (2) and (3). Since the true situation would be unknown during acquisition, both the even and odd values must be considered. Note that this, also, requires only a very small amount of additional computation.

4. Word Tracking

The receiver is required to establish and maintain correct word timing. Our method is similar to that of Ref. 2. Spectra P are accumulated in step with the transmitted signals, and an additional set Q is accumulated with a timing lag of $T/2$. Figure 3 illustrates the situation where each word is broken into two pieces ($k = 2$). A new spectrum is taken for each interval marked in the figure. Spectra 1 and 2 are averaged to produce the first in-step spectrum. Spectra 3 and 4 produce the second, etc. The first delayed spectrum is computed by averaging spectra 2 and 3, the second by averaging 4 and 5, and so on. Notice the economy of computation when k is an even integer. Because of this simplicity, we require that k be even.

In the absence of noise, the receiver will always select the correct frequency. However, the magnitude of the measured spectral peak depends on the word timing error. Figure 4 is a graph of this dependence. The magnitude is

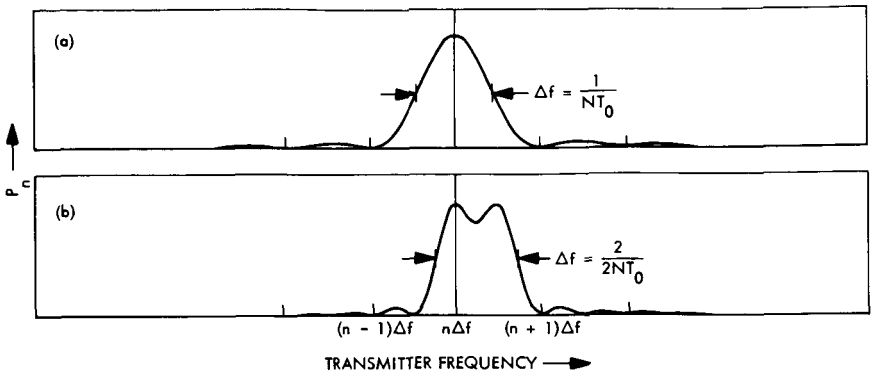

Fig. 1. Filter response characteristic: (a) amplitude of spectral computation, (b) sum of adjacent spectral points [double resolution of Part (a)]

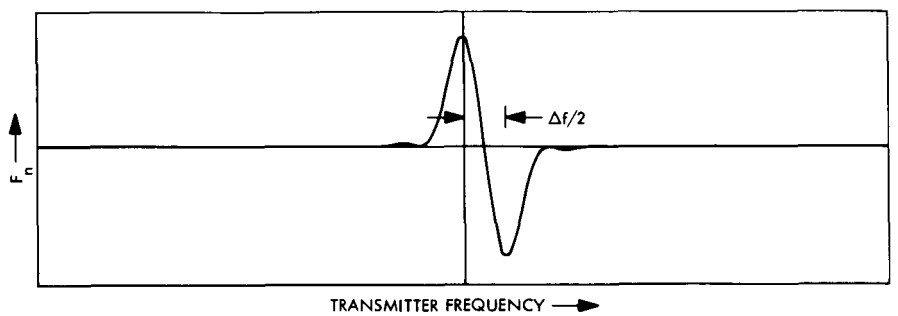

Fig. 2. Frequency-tracking S-curve formed by differencing adjacent spectral points

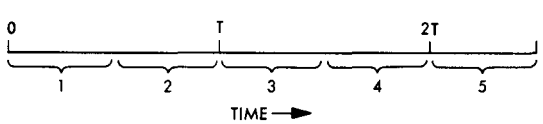

Fig. 3. Timing intervals during which subspectra are being accumulated

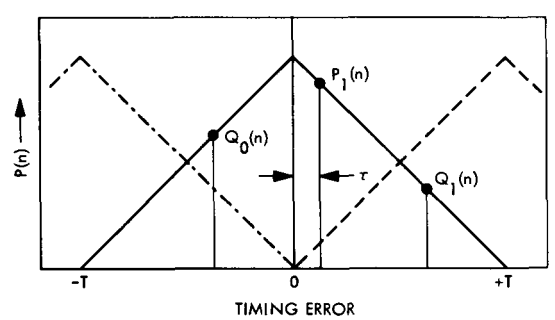

Fig. 4. Amplitude of spectral computation as timing phase is varied

maximum when the timing error is zero and drops to zero as the error reaches $\pm T$.

The in-phase spectrum $P(n)$, the spectrum which has the maximum response, is used to select n, the transmitted frequency. The two adjacent delayed spectra $[Q_0(n)$ and $Q_1(n)]$ provide a tracking S-curve simply by differencing them:

$$G_n = Q_0(n) - Q_1(n)$$

G_n, filtered through an appropriate time constant, is used to acquire and track any word time variations.

Two factors tend to disrupt this timing loop: (1) The transmitter may not change frequencies every word time, and then the curve of Fig. 4 would not apply; and (2) under noisy conditions an error may be made in choosing n. The first problem can be solved by checking adjacent values of n. If they are different, everything is all right; but if not, G_n should simply be set to zero. In the second case, the loop will be disturbed by extra noise, and we must account for it.

5. Tracking Loop Performance

The S-curve value F_i is the result of subtracting two noisy spectral computations. As long as the frequency error is small, F_i can be written

$$F_i = \begin{cases} af_i + n_i, & \text{if no error is made} \\ m_i, & \text{otherwise} \end{cases} \tag{4}$$

where f_i is the actual frequency displacement, n_i and m_i are noise terms, and a is the slope of the average S-curve at the origin. This equation implies the common linear-loop assumption.

For our method of obtaining an S-curve, the slope

$$a = \frac{64k}{\pi^2 \Delta f}\left(\frac{P_s}{N_0 \Delta f}\right) \tag{5}$$

where P_s is the signal power, Δf equals $2k/T$, and N_0 is the one-sided noise density.

We close the loop by changing the frequency by a small amount, proportional to F_i

$$f_{i+1} = f_i - b\,F_i \tag{6}$$

where b is a constant which controls the bandwidth of the loop. We have assumed that there has been negligible transmitter frequency drift during the T sec. Equations (4) and (6) yield the transient performance of the loop, for the noise-free case

$$f_i = (1 - ab)^i f_0$$

That is, given an initial displacement, the loop returns to zero exponentially with a time constant

$$\tau = \frac{-T}{\ln(1 - ab)} \tag{7}$$

where T is the word time.

In the presence of noise, the frequency displacement f will be a random quantity. It can be shown from the equations above that the variance of f_i

$$\sigma_f^2 = \frac{ab}{(2 - ab)} \frac{\left(\sigma_n^2 + \sigma_m^2 \dfrac{p_e}{(1 - p_e)}\right)}{a^2} \tag{8}$$

where σ_n^2 and σ_m^2 are the variances of n and m, respectively, and p_e is the probability of an incorrect choice.

Expressions for σ_n^2 and σ_m^2 are easily found from the probability distributions of the following *Subsection 6*. When they are substituted into the equation above, the result is

$$\frac{\sigma_f^2}{(\Delta f)^2} = \frac{ab}{2 - ab}\left[\frac{\pi^4}{512k(1 - p_e)}\left(\frac{\Delta f N_0}{P_s}\right)^2 + \frac{\pi^2}{64k}\left(\frac{\Delta f N_0}{P_s}\right)\right] \tag{9}$$

It is interesting to note that σ_f^2 depends only weakly on the probability of error; thus, the loop will track to thresholds below any we care to use.

A practical design limits σ_f^2 to a value such that the degradation can be considered negligible, say $\leq 0.01\,\Delta f^2$. Then, with the system parameters $p_e, k, P_s/N_0\Delta f$ previously determined, Eq. (9) gives the product ab which is needed. Equation (7) then gives the resulting time constant of the loop, which can be used as a specification or constraint on the oscillator stability.

A similar formulation holds for the time tracking loop. The only differences are a change in the slope of the S-curve, and a slightly altered noise variance. The results are

$$a = \frac{4k}{T}\left(\frac{P_s}{\Delta f N_0}\right) \tag{10}$$

$$\frac{\sigma_\tau^2}{T^2} = \frac{ab}{(2 - ab)}\left[\frac{1}{(1 - p_e)k}\left(\frac{\Delta f N_0}{P_s}\right)^2 + \frac{1}{2k}\left(\frac{\Delta f N_0}{P_s}\right)\right] \tag{11}$$

6. Probability of Error

Let the received signal be of the form

$$s(t) = a\cos w_n t + b\sin w_n t + n(t) \tag{12}$$

where $n(t)$ is the noise, and the signal power P_s equals $(a^2 + b^2)/2$. Then the spectrum computed for the correct frequency will be the average of k terms, such as

$$P(n) = (a + x)^2 + (b + y)^2 \tag{13}$$

where x and y are independent gaussian variables of variance N_0k/T. For the incorrect frequencies, the terms will have the similar form

$$P(m) = x^2 + y^2 \tag{14}$$

It is necessary to find the probability densities for these cases in order to compute the probability of error. Lindsey (Ref. 6) has derived these densities from their Fourier transforms. The probability density corresponding to Eq. (13) is

$$\text{prob}(P) = \frac{\exp\left(-\dfrac{P + kn^2}{2}\right) P^{2k-1}}{4\pi\, 1\cdot 3\cdot 5 \cdots (4k - 3)} \times \int_0^{2\pi} \sin^{4k-2}\theta \exp\left[(kP)^{1/2} M\cos\theta\right] d\theta \tag{15}$$

where M^2 equals $2P_s/N_0\Delta f$. The corresponding Fourier transform is

$$\text{Ave}\,[\exp(j\omega P)] = \frac{\exp\left[\dfrac{kM^2}{2(1-2j\omega)} - \dfrac{kM^2}{2}\right]}{(1-2j\omega)^{2k}} \tag{16}$$

This Fourier pair can be found for the case $k=1$ directly from their defining equations. Extension to other values of k can be accomplished by successive differentiation with respect to the parameter M.

The probability of error is found from Eq. (15), with some manipulation:

$$P_e = \frac{\exp\left(-\dfrac{pS}{2}\right)}{2\pi\, 1\cdot 3\cdot 5\cdots(4k-3)} \int_0^\infty y^{2k-1} \int_0^\pi \sin^{4k-2}\theta \exp\left[-\frac{y}{2} + (ypS)^{1/2}\cos\theta\right] d\theta \left\{1 - \left[1 - \exp\left(-\frac{y}{2}\right)\sum_{i=0}^{2k-1}\frac{\left(\frac{y}{2}\right)^i}{i!}\right]^{2p-1}\right\} dy \tag{17}$$

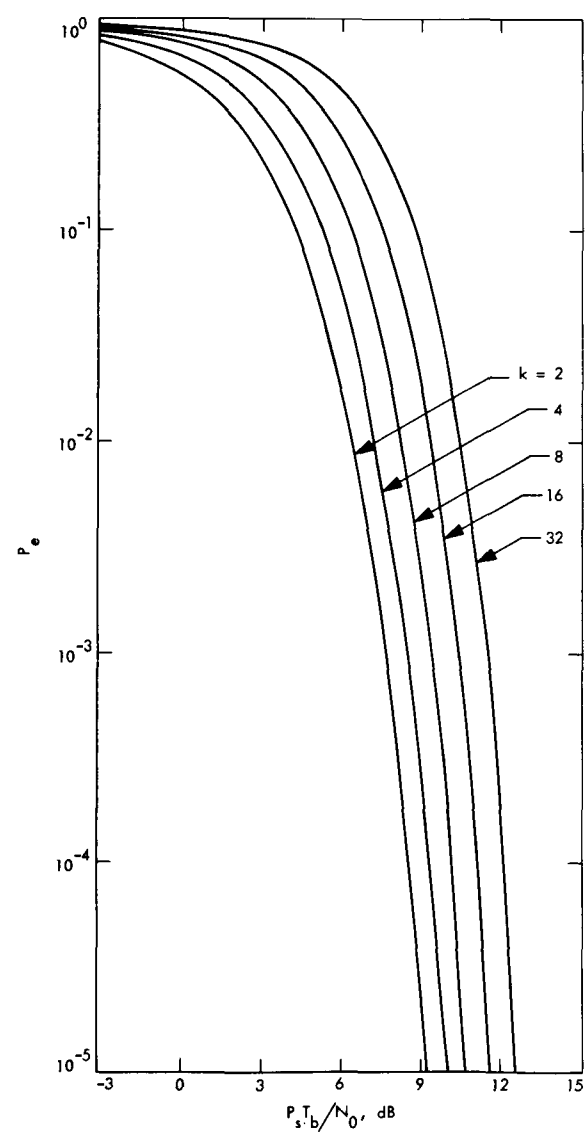

Fig. 5. Plot of P_e against signal-to-noise ratio P_sT_b/N_0, with $p = 4$

where k is the number of spectra averaged, p is the number of bits per word, and S is the signal-to-noise ratio $2P_sT_b/N_0$.

We have evaluated P_e numerically from Eq. (17) rather than pursue it further analytically. The results are given in Figs. 5, 6, and 7 for different values of p. P_e is plotted against S, with k as a parameter.

7. Design Procedures

The spectral width of the transmitter receiver system, $\widehat{\Delta f}$, has already been identified as a design constraint. Other constraints are the data rate R; the probability of error P_e; and the time required for the receiver to compute a single spectrum of $2N$ frequencies, C_{2N}. C_{2N} depends not only on the speed of the computer but also on the skill of the programmer.

From these constraints, we desire to find the following system parameters: the number of bits/word p ($N = 2^p$ frequencies in the signalling alphabet); the word time T; the number of subspectra averaged in one word time k; and the required signal-to-noise ratio P_sT_b/N_0.

Our method of matching the response of the receiver to the spectrum of the transmitter requires

$$\widehat{\Delta f} \leq 2k/T \tag{18}$$

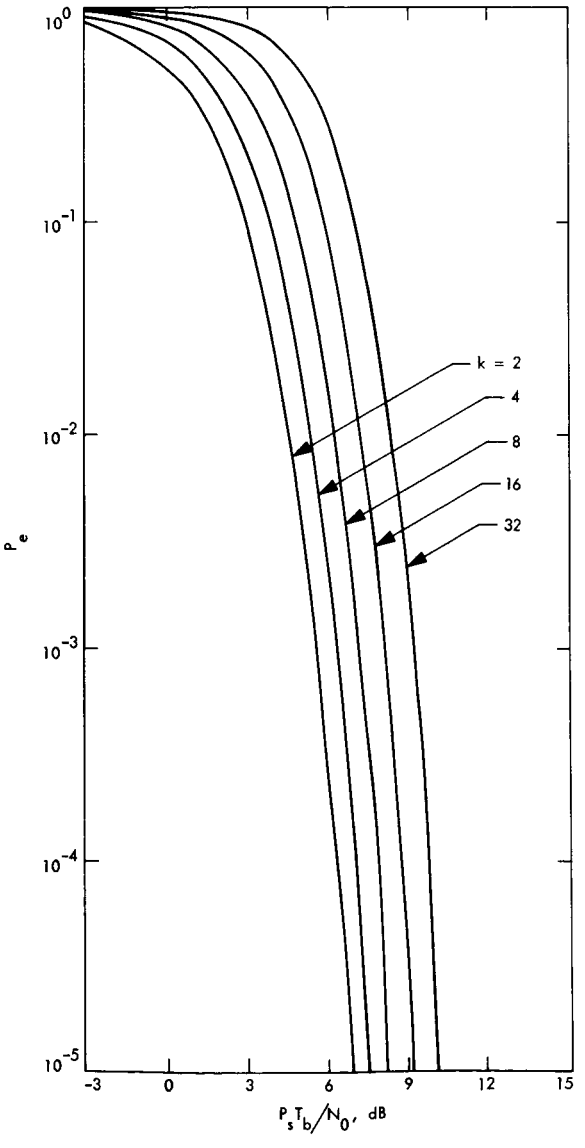

Fig. 6. Plot of P_e versus P_sT_b/N_0, with $p = 8$

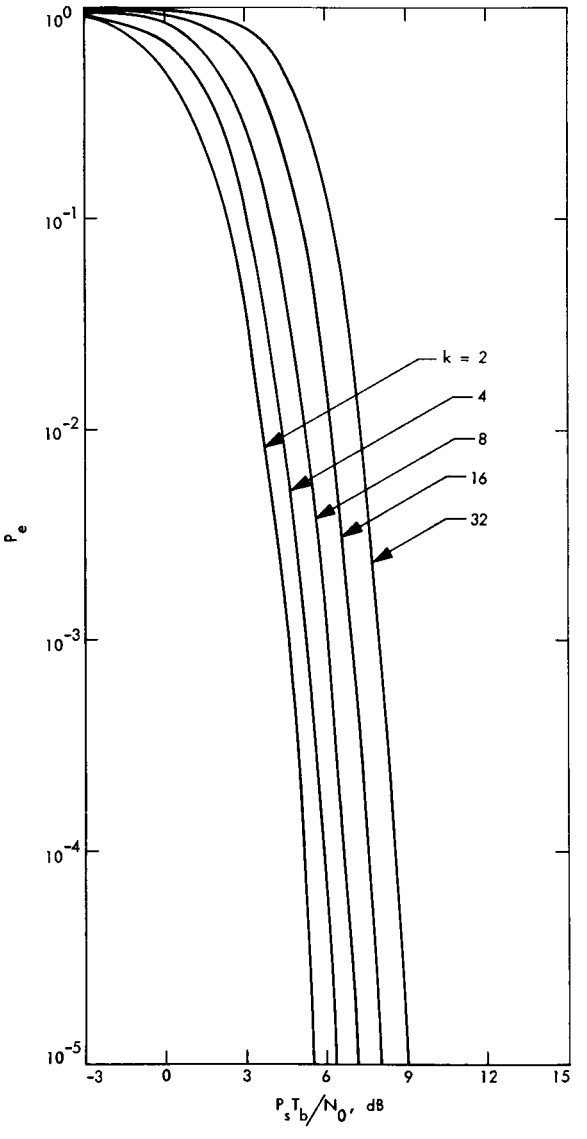

Fig. 7. Plot of P_e versus P_sT_b/N_0, with $p = 12$

When $\widehat{\Delta f} < 1/T$, the frequency jitter is too small to be important. This case is referred to as "high data rate." The system we propose here will be useful for high data rate (if not too high) as well as for low. There is no essential limit to the lower end of the scale.

The time required for computation must be less than the time available, hence

$$C_{2N} \leq T/k \tag{19}$$

R, the signalling rate, is defined as

$$R = p/T \tag{20}$$

Equations (19) and (20) yield

$$\frac{C_{2N}}{p} \leq \frac{1}{Rk} \tag{21}$$

Our design procedure, then, is as follows: first choose the largest p satisfying Eq. (21), assuming $k=2$. If Eq. (18) is not satisfied, repeat the first step with larger k (k an even integer). This procedure converges very rapidly. The required P_sT_b/N_0 can then be read from the probability of error graphs for the appropriate p and k.

With these parameters determined, the specifications for the time constraints of the two tracking loops can be found by using Eqs. (11), (9), and (7) of *Subsection* 5.

As an example, consider a situation similar to *Mariner IV* at encounter. Assume the transmitter line width $\widehat{\Delta f}$ is 4 Hz. (Our experience has shown that if the up-link is locked $\widehat{\Delta f} < ½$ Hz.) Assume also that $R = 10$ bits/s. An SDS 930 computer has been programmed to compute 512 point spectra in 0.3 s.

Then application of the above procedure yields

$$p = 8 \text{ bits/word}$$
$$k = 2$$
$$T = 0.8 \text{ sec}$$
$$\widehat{\Delta f} < 5 \text{ Hz}$$

A signalling alphabet of $2^8 = 256$ frequencies is indicated. Referring to Fig. 6, we see that, for a 0.001 probability of error, $P_sT_b/N_0 = 5.4$ dB. This figure is 11.3 dB below the *Mariner IV* sum of the negative tolerances.

In order to track frequency and timing with negligible error, the loop time constants must be greater than 1 and 3 sec, respectively. The drifts of frequency and timing must be kept slower than these values.

References

1. Reiger, S., "Error Rates in Data Transmission," *Proc. IRE*, Vol. 46, p. 919, May 1958.
2. Goldstein, R. M., and Kendall, W. B., "Low Data Rate Telemetry," *Proceedings of the American Astronautical Society Symposium on Unmanned Exploration of the Solar System*, pp. 501–516, Feb. 1965.
3. Springett, J. C., and Charles, F. J., "The Statistical Properties of the Spectral Estimates Used in the Decision Process by a Spectrum Analyzer Receiver," paper presented at National Telemetering Conference, San Francisco, Calif., 1967.
4. Ferguson, M. J., "Communication at Low Data Rates—Spectral Analysis Receivers," *IEEE Trans. Comm. Tech.*, Vol. COM-16, No. 5, pp. 657–668, Oct. 1968.
5. Cooley, J. W., and Tukey, J. W., "An Algorithm for the Machine Computation of Complex Fourier Series," *Math. Comput.*, Vol. 19, pp. 297–301, 1965.
6. Lindsey, W. C., "Error Probabilities for Rician Fading Multichannel Reception of Binary and N-ary Signals," *IEEE Trans. Inf. Th.*, Vol. IT-10, pp. 339–350, Oct. 1964.

B. Frequency Generation and Control: Programmable RF Attenuator, *S. Fisher*

1. Introduction

A remotely controllable S-band signal source of improved accuracy is needed for DSN system upgrading, as well as for implementation of digital control to facilitate eventual computer control of receiver checkout.

The specified output power stability of the present test transmitter is ±0.5 dB. To obtain better results, it is currently necessary to monitor the RF power level at the transmitter with a Hewlett-Packard 531 power meter and make corrective adjustments. This method does not lend itself to remote operation.

The variable attenuator in the test transmitter is a PRD Electronics, Inc., type 198. There are no published specifications on the linearity tolerance of this unit, but it is estimated to be ±1%. Substitution of a better S-band attenuator appears unfeasible, because none is known which has significantly better linearity and a range approaching 100 dB.

The approach presently being investigated appears likely to circumvent both of these limitations without introducing major compensating disadvantages. Output signal power stability is dependent primarily on that of a 30-MHz oscillator run in saturated mode. Variable

attenuation is provided by a high-precision 30-MHz unit whose calibration is traceable to NBS. *Subsection 4* describes the method in more detail.

2. Prior Work

Initially, investigation was made to determine whether a PIN diode attenuator operated at S-band was stable enough to use open loop. Attenuation stability measurements on two commercial PIN diode attenuators were described in SPS 37-50, Vol. II, pp. 69–70. The units tested were both Hewlett-Packard, type 8732-B. The attenuation range of 95 dB was satisfactory, but attenuation consistently drifted about 0.25% (in dB) in 10 min, which was unsatisfactory. In one of the units, the original PIN diodes were replaced by passivated PIN diodes, which was expected to improve stability.

3. Passivated Diode Results

The PIN attenuator using passivated diodes has shown markedly improved stability. In Fig. 8, the contrasting performance of the new and old units is evident. The test circuit is shown in Fig. 9. Maintenance of a null balance greater than 64 dB for the duration of the test shows an attenuation stability of 0.01 dB to be very likely. Signal

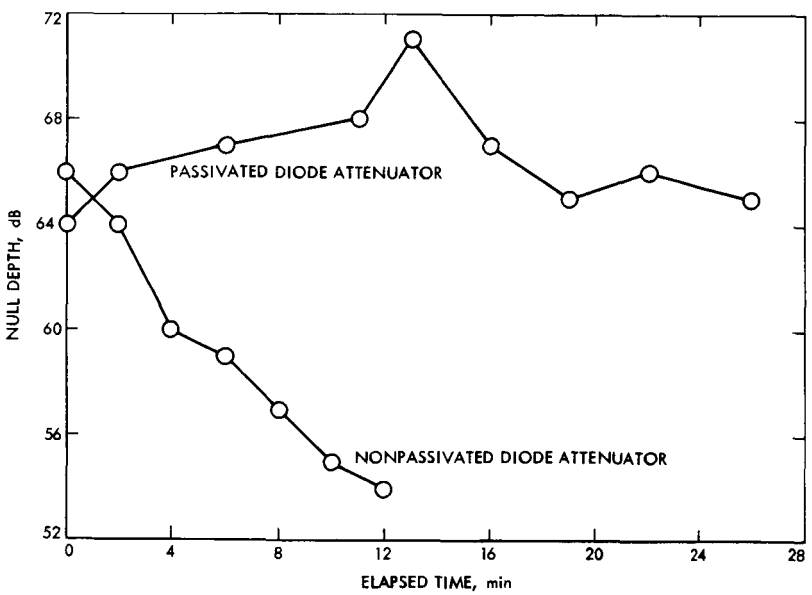

Fig. 8. Drift of attenuators using passivated and nonpassivated PIN diodes in circuit of Fig. 9

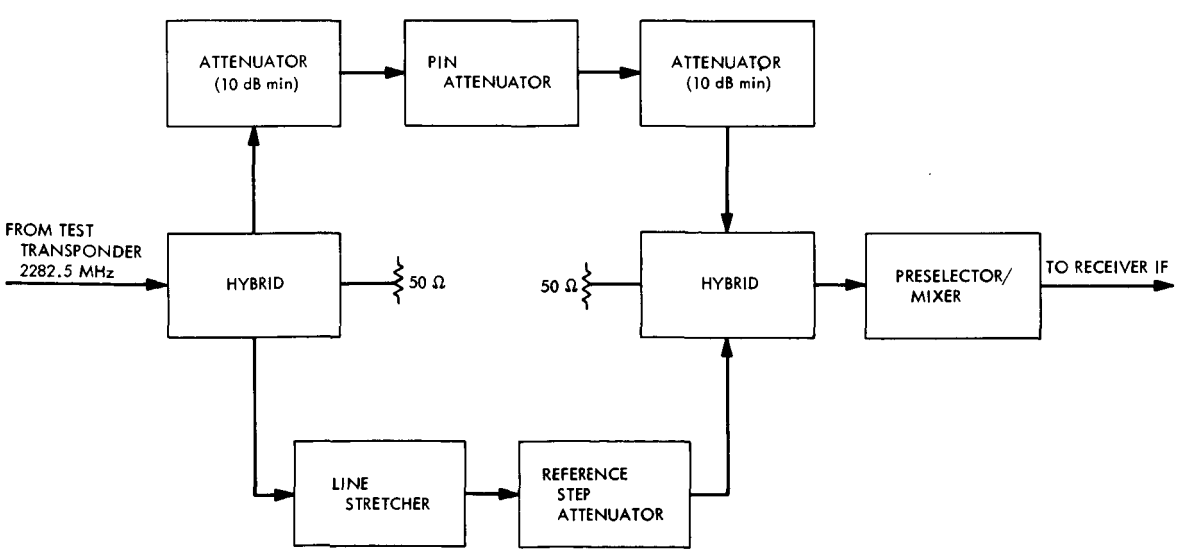

Fig. 9. Circuit for measuring PIN attenuator drift

level drift during a measurement should not be a significant problem in a finished attenuator.

Two other factors undesirably affecting PIN attenuator use are long-term stability and temperature sensitivity.

Long-term stability depends upon the same factors that affect the stability of all semiconductor devices. This indicates difficulty in achieving very high repeatability over an extended period of time. The effects of passivation, preaging, etc., as means toward this end would have to be examined carefully.

Attenuation varies with temperature. When biased from a constant current source, for example, the attenuation changes about 0.11 dB/°C according to Hewlett-Packard data (Ref. 1) and as much as 0.2 dB/°C according to recent JPL measurements (SPS 37-51, Vol. II, p. 84). At constant voltage the attenuation changes in the opposite direction, so that first-order temperature compensation is possible by proper selection of bias source resistance. However, the nonuniform separation between curves of attenuation versus bias current at different temperatures reported in SPS 37-51, Vol. II suggests that good compensation can be obtained over only a small temperature range: perhaps 5 or 10 deg. Furthermore, bias source resistors would have to be selected individually, and effectiveness would differ appreciably from unit to unit.

4. Feedback Stabilized Attenuator

A method not dependent on these factors is needed. Such a method, shown in Fig. 10, encloses the parallel input (PIN) attenuator in a feedback loop. It operates by passing a portion of the PIN attenuator output signal through an isolator to a mixer whose output is at 30 MHz. This signal is one input of a single-pole double-throw chopper; the other input is the output of a precision attenuator acting on a stable 30-MHz reference signal. The amplitude of the square-wave modulation seen on the chopper output is proportional to the difference in input signal levels; the phase depends upon the relative signal amplitudes. This composite is amplified by an IF amplifier with automatic gain control and then synchronously detected. The resulting error signal is amplified and applied as bias to the control input of the PIN attenuator.

With the feedback loop closed, the S-band signal level is controlled by the output level, and hence the setting, of the precision 30-MHz attenuator. Digital positioning of this attenuator will allow remote manual or computer control of the S-band output.

The stability and accuracy of the S-band signal are almost entirely dependent upon the amplitude stability and accuracy of the precision attenuator and the 30-MHz reference signal, and on the mixer linearity.

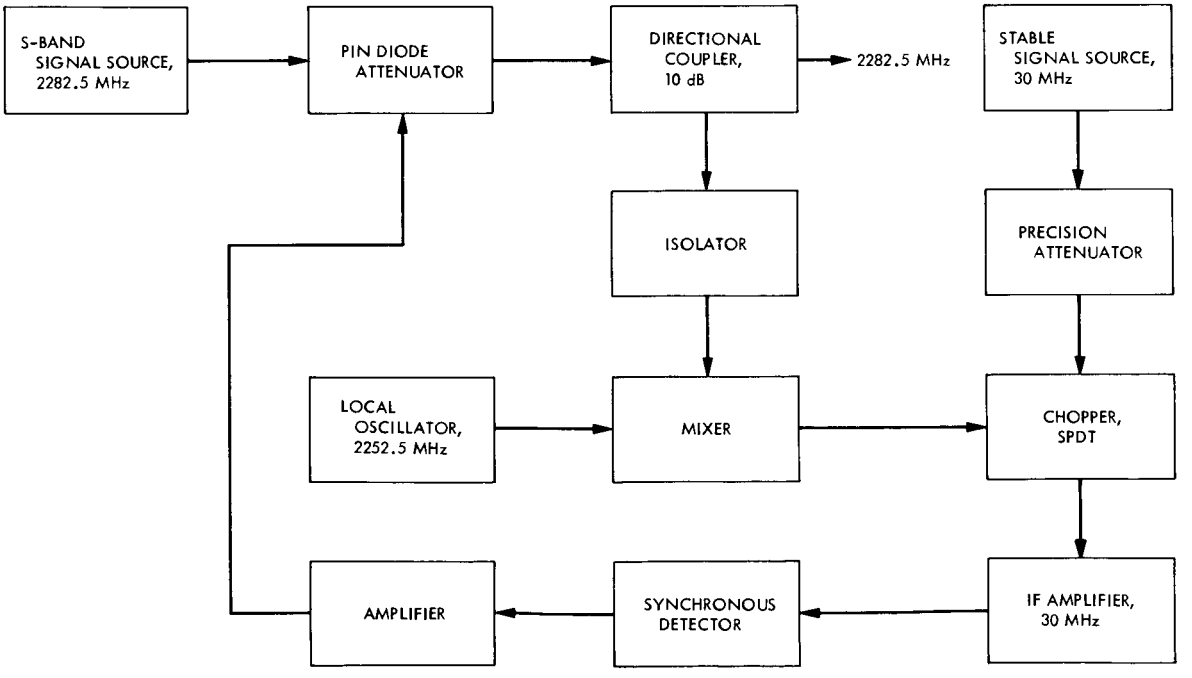

Fig. 10. Block diagram of feedback-stabilized PIN diode attenuator feasibility model

5. Feasibility Test Model

A feasibility test model was built which performs very satisfactorily. Its output signal at 2282.5 MHz is smoothly adjustable from −14 to −94 dBmW with a calculated linearity error ≤0.4 dB. Amplitude stability is in the neighborhood of 0.02 dB, short and medium term. Long-term stability is expected to be comparable. The only spurious output frequency is 30 MHz away at a level of −78 dBmW. About 50 dB further reduction in this level is expected by cascading two more 27-dB isolators at the mixer signal input.

Lower signal levels for system testing can be obtained by introducing fixed attenuation. For example, use of 90 dB additional attenuation with the feasibility unit would give an output signal range of −104 to −184 dBmW, with the spurious level at −168 dBmW reducible probably to well below −200 dBmW (dependent, of course, on shielding and filtering efficacy).

6. Future Work

The relationship between dynamic range and signal nonlinearity for several types of mixers will be determined in the next step in this investigation, and work will be started on digital positioning of the 30-MHz precision attenuator.

Reference

1. "PIN Modulators," Appendix II, p. II-7, *8403A Modulator Operating and Service Manual.* Hewlett-Packard Corp., Palo Alto, Calif.

C. Multiple-Mission Command: Considerations for Command Communications, *R. C. Tausworthe*

1. Introduction

In the design of any telecommunication system requiring high performance, the engineer is naturally faced with finding an optimal solution under given constraints. For example, the primary limitation in data rate in deep-space communications today is the received signal-power/noise-density ratio S/N_0. Under this constraint, it is natural to inquire what system configuration will maximize the amount of data return. The answer as to what the optimum system is has not been found, except asymptotically in the regions of very high and very low values of S/N_0: at large S/N_0, coherent PSK; and at very small S/N_0, noncoherent FSK. This article investigates the intervening region to make comparisons between some various alternatives for low-rate binary communications, such as might be used on command links.

2. Coherent Phase Demodulation by Residual Carrier Tone

Let us examine first the performance of a binary-modulation, phase-shift-keyed (PSK) system utilizing coherent demodulation by a reference derived from a phase-locked loop tracking a residual carrier component. The receiver input is taken to be one of the form

$$x(t) = A\,2^{1/2} \sin(\omega_0 t + \psi(t) + \theta_0) + n_i(t) \tag{1}$$

where A is the rms signal amplitude, ω_0 is the carrier frequency, θ_0 is a uniformly distributed random variable, $n_i(t)$ is wide-band noise with (two-sided) density N_0 over the band of interest, and $\psi(t)$ is a binary angle process with

$$|\psi(t)| = \psi_0 \tag{2}$$

The *data modulation index* (that fraction of the power allocated to data)

$$I^2 = \sin^2 \psi_0 \tag{3}$$

The information process $\psi(t)$ is a square-wave subcarrier modulated by binary symbols, which can either be coded or uncoded. We shall suppose that maximum likelihood detection (matched filtering) is implemented, that the integration is over m symbols of duration t_0 each, that $T = mt_0$, and that the carrier loop bandwidth is w_L. The normalized communication word rate δ is defined as

$$\delta = \frac{2}{w_L T} \tag{4}$$

Ideally, we would prefer to choose the modulation index such that the probability of correct reception exceeds some fixed design parameter

$$P_c = Pr\{\text{word correct} \mid \text{no slip}\}\, Pr\{\text{no slip}\} + Pr\{\text{word correct} \mid \text{slip}\}\, Pr\{\text{slip}\} \tag{5}$$

and to operate at the maximum rate for the given A^2/N_0. However, because of the difficulty arising in optimizing this index, we shall deviate somewhat in our approach.

It is noteworthy that below some critical value of loop signal-to-noise (SNR), the factor controlling δ is the slip probability, and above this SNR, the controlling factor is the bit error probability, since slips essentially cease to occur.

When $\delta << 1$, the optimum allocation of power between carrier and data for linear loop operation (no cycle slips) is that maximizing $I^2 [E(\cos\phi)]^2$, viz.,

$$I^2 = 1 + \frac{1}{2\rho_L}(1 - [1 + 4\rho_L]^{1/2}) \tag{6}$$

where ρ_L is the SNR which would be apparent if all power were concentrated in the carrier tone:

$$\rho_L = \frac{A^2}{N_0 w_L} \tag{7}$$

Equation (6) is valid whenever $\delta << 1$ and when the loop phase error σ^2 is small enough that the linear loop theory is intact. The possibility of cycle slips in the loop are ignored.

However, at very small values of ρ_L, there is the distinct possibility that the carrier loop may lose lock, slipping cycles during the reception of part of the message. Such would not be unpredictably detrimental if the loop relocked immediately, but it could be abortive if the loop did not. Convenient evaluations of the effects of phase error are based on zero-detuning formulas. As is always the case, the tracking loop is somewhat stressed, so the "zero-detuning" assumption is slightly in error. The effect is only slight, however, when the loop is locked; but when slips occur, the effect can be very large. A subsequent article will treat this case in more detail. Hence, we shall make the pessimistic assumption that, if the loop slips, the word is most surely detected in error, and thus we shall demand, as a design restriction, that the probability of slipping a cycle during a word not exceed some value P_s. We shall assume, for convenience, that cycle slips are essentially independent from word to word. Hence, we can approximate the time between slips by the first-slip time. At reasonable SNR's (> 3 dB) in the loop, the first-slip time t_s is distributed in a near-Poisson fashion (SPS 37-43, Vol. III, pp. 76–80)

$$p(t_s) = \frac{1}{\mu}\exp(-t_s/\mu) \tag{8}$$

where $\mu = E(t_s)$ is the mean first-slip time

$$\mu \approx \frac{K}{w_L}\exp[\gamma\rho_L(1 - I^2)] \tag{9}$$

The values K and γ depend on the order of the loop, its damping factor, etc. For example, in the first-order loop, $K = \pi/2$ and $\gamma = 2$. Experimental measurements for the second-order loop with 0.707 damping produce $K \approx 3.5$ and $\gamma \approx 1.2$. We shall assume these latter values in what follows.

The probability that there was a slip during the T-sec word is then

$$P_s = \int_0^T \exp(-t/\mu)\frac{dt}{\mu} = 1 - \exp(-T/\mu) \tag{10}$$

so that the required condition for integrity in the tracking function is

$$\rho_L(1 - I^2) \geqq \frac{1}{\gamma}\ln\frac{2}{\delta K \ln\left(\frac{1}{1 - P_s}\right)} \approx \frac{1}{\gamma}\ln\left(\frac{2}{\delta K P_s}\right) \tag{11}$$

At low values of δ, Eq. (6) restricts ρ_L and δ to values such that

$$\left.\begin{aligned} \rho_L &\geqq \frac{1}{4}\left\{\left[\frac{2}{\gamma}\ln\left(\frac{2}{\delta K P_s}\right) + 1\right]^2 - 1\right\} \\ \delta &\geqq \frac{2}{K P_s}\exp\left\{\frac{\gamma}{2}[1 - (1 + 4\rho_L)^{1/2}]\right\} \end{aligned}\right\} \tag{12}$$

The matched filter output SNR (which is related to the word error probability given no slip) for any I^2 is

$$R_{eq} = \frac{A^2 I^2 E^2(\cos\phi)\,T}{(2N_0)} = \frac{\rho_L I^2 E^2(\cos\phi)}{\delta} \tag{13}$$

Setting a given error probability fixes the value of R_{eq}. As a result, during times when the loop error is small, the word rate satisfies the equation

$$\delta = \frac{\rho_L I^2 E^2(\cos\phi)}{R_{eq}} \approx \frac{\rho_L I^2 \exp(-\sigma^2)}{R_{eq}} \tag{14}$$

for $\delta << 1$.

When $\delta >> 1$, the value of I^2 should be replaced by (Ref. 2)

$$I^2 = 1 - \frac{k\rho_L - \delta + [(k\rho_L - \delta)^2 + 4\rho_L\delta(\delta + k)]^{1/2}}{2\rho_L(\delta + k)} \tag{15}$$

in terms of the parameter

$$k = \begin{cases} 2, & \text{uncoded bits} \\ 1, & \text{orthogonal code words} \end{cases} \tag{16}$$

and the value of R_{eq} should be replaced by (SPS 37-54, Vol. III, pp. 195–201)

$$R_{eq} = \frac{2}{k}\left(\operatorname{erfc}^{-1}\left\{2\int_0^{\pi}\operatorname{erfc}\left[\left(\frac{k\rho_L I^2}{2\delta}\right)^{1/2}\cos\phi\right]p(\phi)\,d\phi\right\}\right)^2 \tag{17}$$

For a fixed R_{eq}, the error probability for a dictionary-size M is approximately (exact for the uncoded case)

$$P_E(R_{eq}) \approx \frac{M-1}{2}\operatorname{erfc}\left[\left(\frac{kR_{eq}}{2}\right)^{1/2}\right] \tag{18}$$

The behavior of the rate δ as a function of ρ_L is thus as follows: At very low ρ_L, when the loop cannot track, the data is much degraded, so δ is small, merely because of word-error likelihood. However, because of the long words, slips are extremely likely. As ρ_L is raised, it reaches a critical value such that the loop tracking becomes very efficient; consequently, slips are infrequent enough to allow some of the power to be put in the data, so δ rises until, finally, it is asymptotic to

$$\delta \sim \frac{\rho_L}{R_{eq}}, \qquad \text{as } \rho_L \to \infty \tag{19}$$

We may plot the error probability due to slips and due to matched-filter SNR (i.e., Eqs. 12 and 14) to show which error is the limiting factor in performance. These appear in Fig. 11.

3. Costas Loop Demodulator

We now set ψ_0 of *Subsection* 2 to $\pi/2$, completely suppressing the residual carrier tone. To effect a coherent detection, a Costas (or squaring) loop is implemented. The phase error in the loop is related to an equivalent loop SNR, ρ_{eq}, in the same way the ordinary loop is related to its SNR:

$$\rho_{eq} = \frac{\rho_L}{4}\left(1 + \frac{w_H}{\eta w_L \rho_L}\right)^{-1} \tag{20}$$

where w_H is the premultiplication (or presquaring) bandwidth, which must be assumed much larger than the loop bandwidth w_L, and the factor η is a filter-form factor: $\eta = 4$ for a single-pole characteristic, $\eta = 2$ for the ideal bandpass case.

The linear-theoretical loop error Φ has variance

$$\sigma_\Phi^2 = \frac{1}{\rho_{eq}} \tag{21}$$

The amplitude detector, however, sees the error as $\phi = \Phi/2$, so that its linear-theoretical error variance is

$$\sigma^2 = \frac{1}{\rho_L}\left(1 + \frac{w_H}{\eta w_L \rho_L}\right) \tag{22}$$

It is clear that there is an advantage in having a narrow w_H. However, the expression for ρ_{eq} was derived on the supposition that w_H was wide enough to pass all the data. Accounting for this fact and dismissing the limitation $w_H >> w_L$ leads to an optimum value of w_H specified by (SPS 37-37, Vol. IV, p. 120)

$$\frac{w_H}{\eta w_L} \approx \frac{1}{2} m\delta \tag{23}$$

However, as we have said, the ratio $w_H/\eta w_L$ must be larger than some value, say W_0, merely for loop stability reasons. We thus shall set

$$\frac{w_H}{\eta w_L} = \begin{cases} W_0, & \text{for } \delta < 2W_0/m \\ \frac{1}{2} m\delta, & \text{for } \delta > 2W_0/m \end{cases} \tag{24}$$

In accordance with the tracking requirement for the loop,

$$\rho_{eq} \geq \frac{1}{\gamma}\ln\left[\frac{2}{\delta K}\ln\left(\frac{1}{1-P_s}\right)\right] \approx \frac{1}{\gamma}\ln\left(\frac{2}{\delta K P_s}\right) \tag{25}$$

which then sets the approximate limit

$$\rho_L \geq \frac{2}{\gamma}\ln\left(\frac{2}{\delta K P_s}\right)\left[1 + \left(\frac{\gamma W_0}{\ln(2/\delta K P_s)}\right)^{1/2}\right] \tag{26}$$

Above this value of ρ_L, the primary limitation is in the bit-error rate.

Again, when the phase error is small, the value of R_{eq} regulating the error probability is

$$R_{eq} = \frac{\rho_L E^2(\cos\phi)}{\delta} \approx \frac{\rho_L \exp(-\sigma^2)}{\delta} \tag{27}$$

for $\delta << 1$, so that the rate of operation above the ρ_L bound is approximated by

$$\delta = \frac{\rho_L}{R_{eq}}\exp\left[-\frac{1}{\rho_L}\left(1 + \frac{w_H}{w_L \eta \rho_L}\right)\right] \tag{28}$$

The equation becomes transcendental in δ as soon as ρ_L is large enough that $\delta \geqq 2W_0/m$. Asymptotically, however, the rate approaches

$$\delta \sim \frac{\rho_L}{R_{eq}}, \qquad \text{as } \rho_L \to \infty \tag{29}$$

just as did the carrier-tone-reference demodulator.

4. Noncoherent Binary FSK

The third alternative we consider is merely the noncoherent FSK receiver with two known frequencies and bit intervals T sec long. The error rate for an optimized receiver is (Ref. 3)

$$P_E = \frac{1}{2} \exp\left(\frac{1}{2} R_{eq}\right) \tag{30}$$

in which R_{eq} is now merely

$$R_{eq} = \frac{\rho_L}{\delta} \tag{31}$$

so that the rate increases linearly in ρ_L

$$\delta = \frac{\rho_L}{R_{eq}} \tag{32}$$

Because of the absence of a loop, there is no added degradation at very low values of ρ_L.

5. Comparison of Results

Figure 11 is a plot of the performance of the three communications systems for the simple uncoded-word case. Both the bit error and slip-during-bit probability are set at 10^{-5}, as might be used for a command system. The first-order Fokker-Plank theory is used as a model for the loop error, both in the carrier-tone loop and in the squaring loop, along with their detection degradations (Ref. 2)

$$\begin{aligned} E(\cos\phi) &= \frac{I_1[\rho_L(1-I^2)]}{I_0[\rho_L(1-I^2)]}, && \text{carrier loop} \\ &= \frac{I_2(\rho_{eq})}{I_0(\rho_{eq})}, && \text{squaring loop} \end{aligned} \tag{33}$$

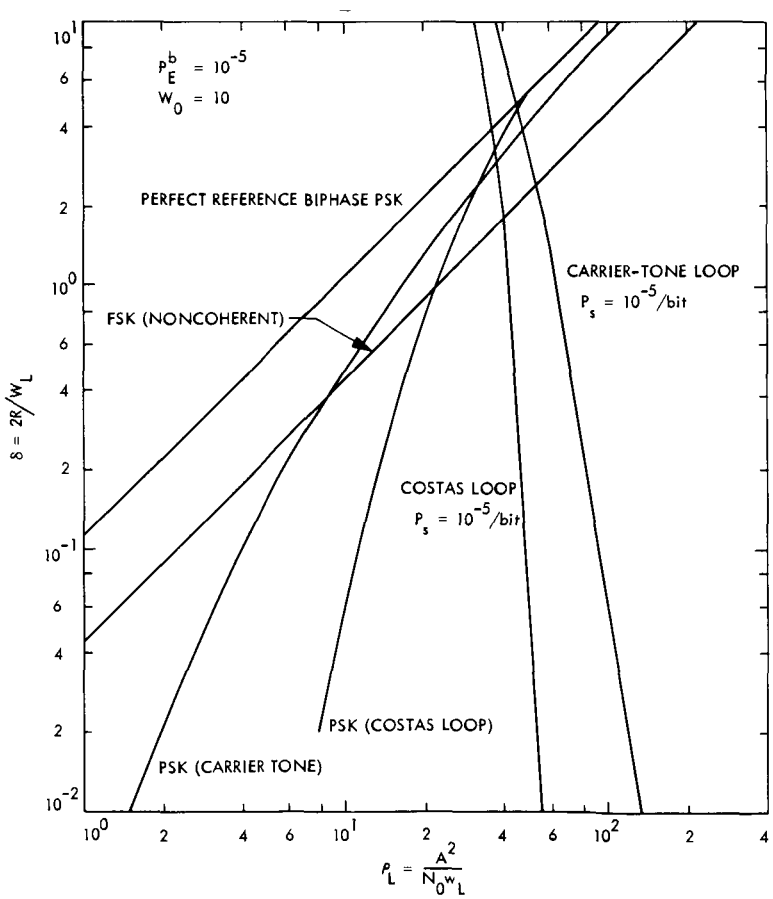

Fig. 11. Comparison of low-bit rate communications schemes

It is interesting to note that on the basis of error rate alone, there are regions in which the data rate is maximized by each system: below $\rho_L \approx 8.5$, FSK is superior; between $\rho_L \approx 8.5$ and 30 the carrier-tone PSK excels; and beyond $\rho_L \approx 30$ the squaring-loop scheme prevails. However, the addition of the loop cycle-slip requirement makes it necessary, in either of the two loop-schemes, to operate at $\rho_L > 36$. The conclusion is thus that for $\rho_L < 36$, some form of noncoherent FSK is needed, and that beyond $\rho_L > 36$, squaring-loop reference is preferable.

The three systems analyzed are highly idealized. The FSK system assumed that the frequencies of reception were known exactly, but not in phase. An actual FSK system would be somewhat degraded according to the frequency uncertainty. The carrier-tone system consideration omitted the subcarrier-tracker and its degradation (which only makes it less attractive). However, the Costas-loop scheme requires no subcarrier, so its performance is essentially as indicated.

References

1. Lindsey, W. C., "Determination of Modulation Indexes and Design of Two-Channel Coherent Communications Systems," *IEEE Trans. Com. Tech.*, Vol. COM-15, No. 2, Apr. 1967, pp. 229–237.
2. Lindsey, W. C., "Design of Block-Coded Communications Systems," *IEEE Trans. Com. Tech.*, Vol. COM-15, No. 4, pp. 525–534, Aug. 1967.
3. Wozencraft, J. M., and Jacobs, I. M., *Principles of Communication Engineering*, Sect. 7.3, John Wiley & Sons, New York, 1965.

V. Advanced Engineering: Communications Elements Research

A. Low Noise Receivers: Microwave Maser Development, *R. Berwin*

1. Introduction

Primary investigations associated with the development of solid-state masers must include a thorough study of crystal materials which show promise in maser applications. Included as desirable properties of maser materials are a zero-field splitting comparable to the signal frequency, a moderate magnetic field requirement, large signal and pump transition probabilities, and low relaxation rates between the signal-energy levels to avoid low-level saturation.

This article reports on the work in progress pertaining to the crystals being investigated for the microwave maser, particularly at the signal frequency of 15.3 GHz, with future application at 90 GHz. The methods used in these preliminary investigations are also given.

2. Discussion

The properties of ruby, and iron-doped rutile and zinc tungstate are being investigated as maser materials for operating at 15.3 GHz. For this purpose, computer programs have been developed for the IBM 7094 to solve the spin-Hamiltonian and transition probability matrices for the energy levels and transition matrix elements of each of the materials. The diagonalization of the spin-Hamiltonian is implemented by a routine SYMEIG[1] which uses the Givens–Householder method for real symmetric matrices. Since the spin-Hamiltonian is Hermitian, the $n \times n$ matrix is expanded into a $2n \times 2n$ real symmetric matrix. The routine output gives the eigenvalues and orthonormal eigenvectors of the matrix equation $H\Psi = \lambda\Psi$. Based on the results of these calculations, an experimental investigation is being conducted to verify or improve the calculated values which are favorable for signal amplification, and to categorize some operating schemes for maser performance.

3. Experimental Method and Apparatus

The experimental method used is the reflection-type cavity maser system. Figure 1 shows a cavity maser in a

[1]Hanson, R. J., *A Linear Algebraic Computational Package for Use With FORTRAN IV on the IBM 7090/7094*, Mar. 6, 1967 (JPL internal document).

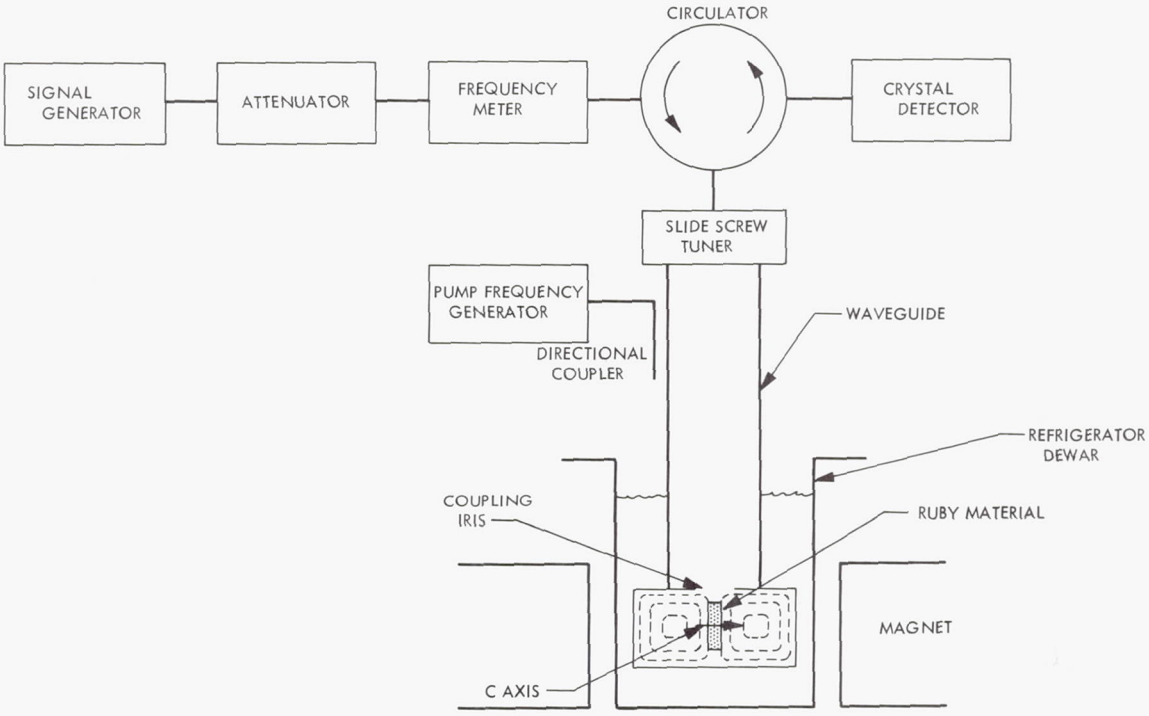

Fig. 1. Experimental arrangement for cavity maser

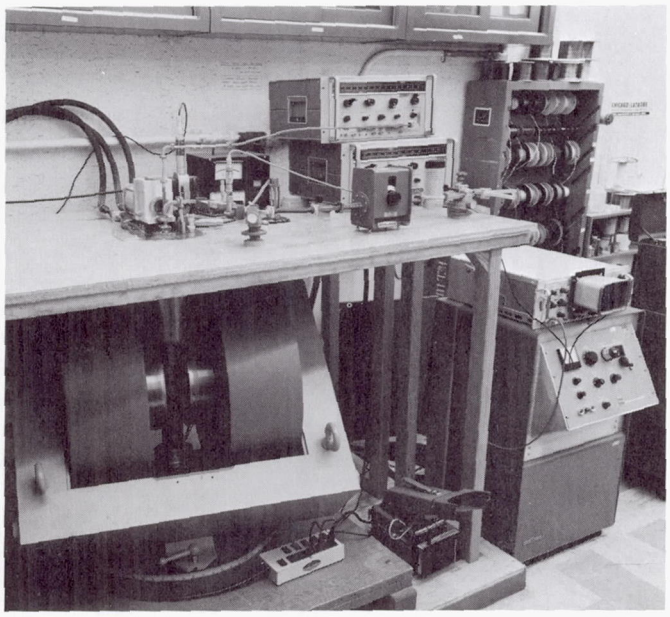

Fig. 2. Cavity maser apparatus

TE201 mode coupled to the waveguide by an iris. The dotted lines show the RF magnetic field distribution, and the ruby material is mounted in the center of the cavity with the *C*-axis along the "*a*" dimension of the cavity. The pump power is fed directly down the *Ku*-band waveguide and through the iris. Another method of coupling is to utilize the crystal itself as a dielectric resonator. Both methods of coupling have been successful, and specific results will be reported in subsequent SPS issues.

A closed-cycle refrigerator (Ref. 1) has been constructed and mounted on the electromagnet, as shown in Fig. 2. The refrigerator directly liquefies helium gas and maintains a liquid helium bath in a cylindrical tube which extends between the poles of the electromagnet. This refrigerator is one of the features of the system, since it eliminates the need for stored liquid helium to be supplied to the dewar.

Reference

1. Higa, W. H., and Wiebe, E., "A Simplified Approach to Heat Exchanger Construction for Cryogenic Refrigerators," *Cryogenic Technology*, Vol. 3, No. 2, p. 15, Mar.–Apr., 1967.

B. Determination of Antenna Temperatures and Flux From Cygnus-A Observations at S-Band,

R. E. Cormack

1. Introduction

Using results of the 210-ft Advanced Antenna System (AAS)/*Surveyor I* gain test (SPS 37-44, Vol. III, pp. 100–

105) and recent observations of Cygnus-A and 3C123, a 100% efficient antenna temperature was determined from observations of Cygnus-A with a 210-ft reflector at 2295 MHz under stated conditions. Under these same conditions, the 100% efficient antenna temperature was derived for an 85-ft reflector and a Cygnus-A flux density.

2. Calculations Using 210-ft Antenna

Based on the *Surveyor I* gain measurement, which assumed a gain standard horn gain of +21.85 dB and a tolerance of ±0.38 dB, 3 σ, the S-band multifrequency cone (SMF) was determined to produce a system efficiency of 59.16% at the maser reference flange.

The radio source 3C123 was repeatedly found to increase the system temperature, defined at the same reference flange, by 21.26°K with a resolution of ±0.53°K, 3 σ. At this time, the S-band cassegrain ultra cone (SCU) was installed; observations of 3C123 repeatedly increased the system temperature, defined at the maser reference flange, by 21.96°K with a resolution of ±0.57°K, 3 σ. Cygnus-A was observed to repeatedly increase the system temperature at the maser reference flange by 610°K with a resolution of ±6°K, 3 σ.

From the 3C123 data, it is determined that the SCU produces a system efficiency of 61.10% at the maser reference. This value represents 0.14-dB additional gain over the SMF. Ground insertion loss tests performed with outstanding accuracy had previously given the insertion loss difference as 0.12 dB. It is assumed that the additional 0.02 dB measured is due to lower mismatches in the SCU, and 0.14 dB ± 0.02 dB is accepted as the true difference.

The above data were all collected during the period from December 1967 to June 1968 at a 35-deg elevation angle with the 210-ft antenna matched to right-handed circular polarization within an ellipticity of 0.5 dB and having a 0.140-deg beamwidth. Then, the Cygnus-A flux available at the earth surface, specifically at the Mars DSS at approximately 3500-ft elevation, with a 100% efficient 210-ft antenna of 0.140-deg beamwidth looking from a 35-deg elevation angle, was such as to produce an antenna temperature of

$$\frac{610°\mathrm{K}}{0.6110} = 998.4°\mathrm{K} \pm 124.1°\mathrm{K}, 3\,\sigma$$

3. Calculations Using 85-ft Antenna

Considering an 85-ft antenna under the same conditions as given in *Subsection 2*, a 100% efficient antenna temperature may be derived in a scaled manner by using beam correction factors (BCF). Taking Cygnus-A to be two point sources separated by 118 arc sec and having a power ratio of 1.2:1, a 210-ft antenna BCF of 1.037 and an 85-ft antenna BCF of 1.007 are obtained. Then, the Cygnus-A flux available at the earth surface, specifically at the Mars DSS at approximately 3500-ft elevation, with a 100% efficient 85-ft antenna of 0.346-deg beamwidth, is such as to produce an antenna temperature of

$$998.4°\mathrm{K} \times \frac{1.037}{1.007} \times \frac{(85\ \mathrm{ft})^2}{(210\ \mathrm{ft})^2} = 168.4°\mathrm{K} \pm 20.9°\mathrm{K}, 3\,\sigma$$

Further, an antenna-independent flux value at the earth surface may be derived for 2295 MHz at the Goldstone DSCC, while observing at a 35-deg elevation angle and by using 998.4°K, the BCF for the 210-ft antenna, and the area of the 210-ft reflector. This value is 888.2 ± 110.4 f.u., 3 σ.[2]

4. Error Analysis

Error sources that are considered are given in Table 1. Possible errors due to impedance and polarization mismatches, the beam correction factors, and differences in wavefront decorrelations across the different apertures are neglected as being small in comparison to the errors considered. For other sites extrapolations in terms of altitude, meteorology, and elevation angle will be necessary.

In conclusion, feedcone changes made at the Mars DSS necessitated consideration of several error sources.

[2]f. u. = flux unit.

Table 1. Error sources and 3-σ tolerances

Error source	3-σ tolerance, dB
(1) Accuracy of SMF–*Surveyor* test	±0.405
(2) Accuracy of SMF–SCU gain difference	±0.020
(3) Repeatability of SMF/3C123 temperatures	±0.107
(4) Repeatability of SCU/3C123 temperatures	±0.111
(5) Repeatability of SCU/Cygnus-A temperatures	±0.042
(6) Accuracy of 21°K temperature determination	±0.054[a]
(7) Accuracy of 610°K temperature determination	±0.258[a]
Overall accuracy rss	±0.509 = 12.4%

[a]With a 20°K total operating temperature without source.

For example, a direct measurement of Cygnus-A might have been accomplished with the SMF. Elimination of error sources 2, 3, 4, and 6 would then improve the overall rss accuracy to 0.484 dB. It is interesting to note the greatest source of error remains the gain standard horn calibration of 0.38 dB in the AAS/*Surveyor I* test.

C. Efficient Antenna Systems: X-Band Gain Measurements, 85-ft Antenna, *R. A. Norman*

1. Introduction

The 85-ft az–el reflector at the Venus DSS was operated at X-band, 8448 MHz, during October 1968 for the purpose of evaluating recent structural changes to the antenna. The antenna was previously operated at X-band during June 1967 (SPS 37-49, Vol. II, pp. 65–67). Since that time, a transmitter room was added to the antenna, the counterweights modified, and the backup structure was rebolted (SPS 37-52, Vol. II, pp. 99–105). A small improvement was also made in the waveguide switch in the X-band cassegrain experimental cone (XCE).

Two celestial sources, Cygnus-A (3C405) and Virgo-A (3C274), were observed during the tests. This article discusses the results of those observations.

2. Tests and Results

After the XCE was installed on the antenna, a measurement of the total operating noise temperature was made. At zenith, the total operating noise temperature was approximately 55°K. A noise temperature of 30°K had been expected. The degradation in performance was traced to the maser preamplifier, which had been physically disturbed due to thermal cycling. Although laboratory tests on both the maser and the waveguide switch indicated improvements had been attained, the field tests proved these were nonstable. For purposes of evaluating the antenna performance, the higher operating noise temperature made little difference, particularly for the case of Cygnus-A. The goal of demonstrating an improved noise performance with the XCE was not realized.

The paraboloidal focal length as a function of elevation angle was examined. While tracking a source, the subreflector was moved in and out axially, and the position giving maximum operating temperature noted. It was found that the focal length changed less than 0.25 in. as the antenna moved between horizon and zenith, so the subreflector was left at a fixed position during later star tracking runs. A setting of −35 deg on the control room synchro indicator was selected as best for all elevations.[3] This corresponds to a subreflector movement of 0.875 in. away from the main reflector, relative to the setting for maximum gain at S-band. This effect has been found in previous work on both 85- and 210-ft antennas. A possible explanation is the best fitting between paraboloid surface and distorted illumination which is caused by the large-sized beamshaping flange at X-band.

Data were also taken to examine beam pointing. Figures 3 and 4 are plots of offset data obtained while tracking Virgo-A and Cygnus-A. These plots are consistent with data taken while tracking other sources. However, the azimuth offsets obtained from Cygnus-A are significantly different from those of any source which has been previously examined. It appears the difference is due to an inaccuracy in the source coordinates which are input to the ephemeris program.

Figure 5 is a plot of 599 measured excess system temperatures referenced to the maser input flange for Virgo-A. The figure includes a second-order polynomial curve which was fit to the data without weighting. Figure 6 is a plot of 1380 excess system temperatures measured on Cygnus-A. Figure 6 also includes a second-order polynomial curve. For both sources, the maximum temperature is measured near 45-deg elevation. For Virgo-A the maximum temperature is 3.9 ± 1.7°K, 3 σ, and for Cygnus-A, it is 17.1 ± 4.3°K, 3 σ. On the basis of the previously selected Cygnus-A flux value (SPS 37-49, Vol. II, pp. 65–67), a system efficiency of 50.3% is obtained.

3. Conclusion

An excess system temperature of 15.7°K on Cygnus-A was reported after the June 1967 tests. The present figure of 17.1°K indicates that the structural work done on the antenna significantly improved the surface tolerance. The rebolting also improved the focal length stability of the antenna to the point where refocussing of the hyperbola is not necessary with changing elevation angle.

All measurements were made with a total operating temperature of approximately 55°K due to a degradation within the XCE.

There remains a serious problem in pointing ability. The pointing jitter is large enough to seriously hamper possible future work at shorter wavelengths.

[3]Private communication with V. Lobb has revealed that machine-reduced civil engineering data also indicates less than a 0.25-in. best fit focal length change, following rebolting.

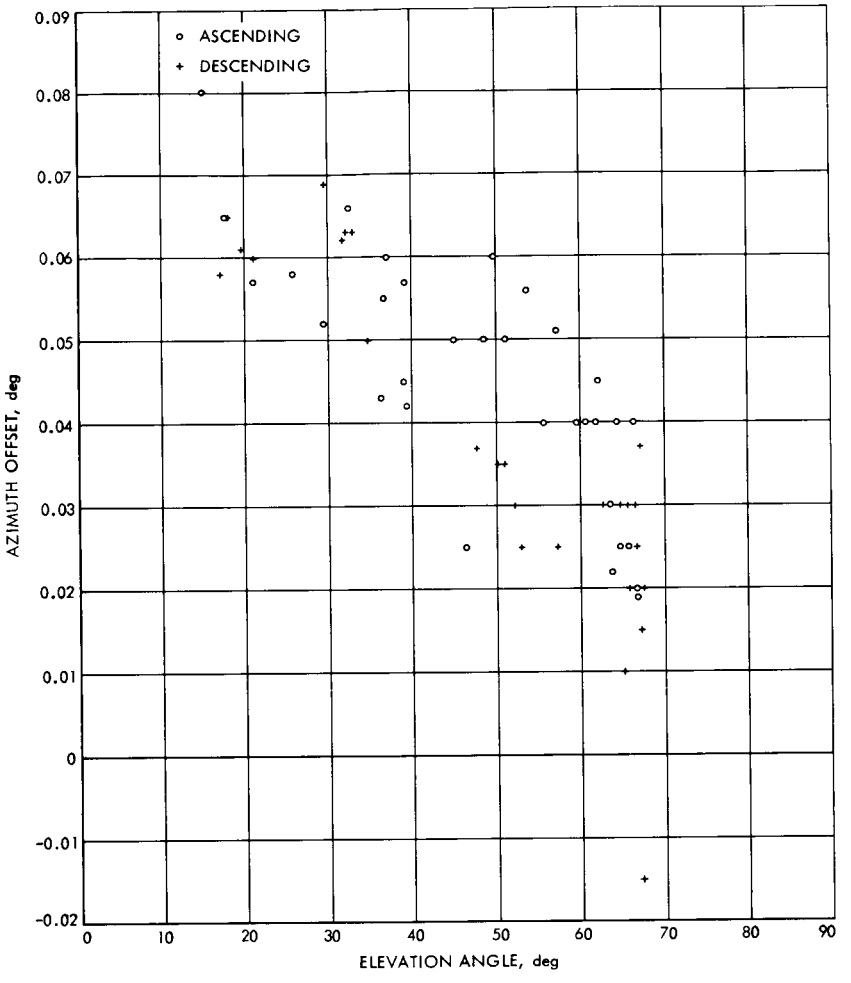

Fig. 3. Azimuth offsets vs elevation angle (Virgo-A, 85-ft antenna, 8448 MHz)

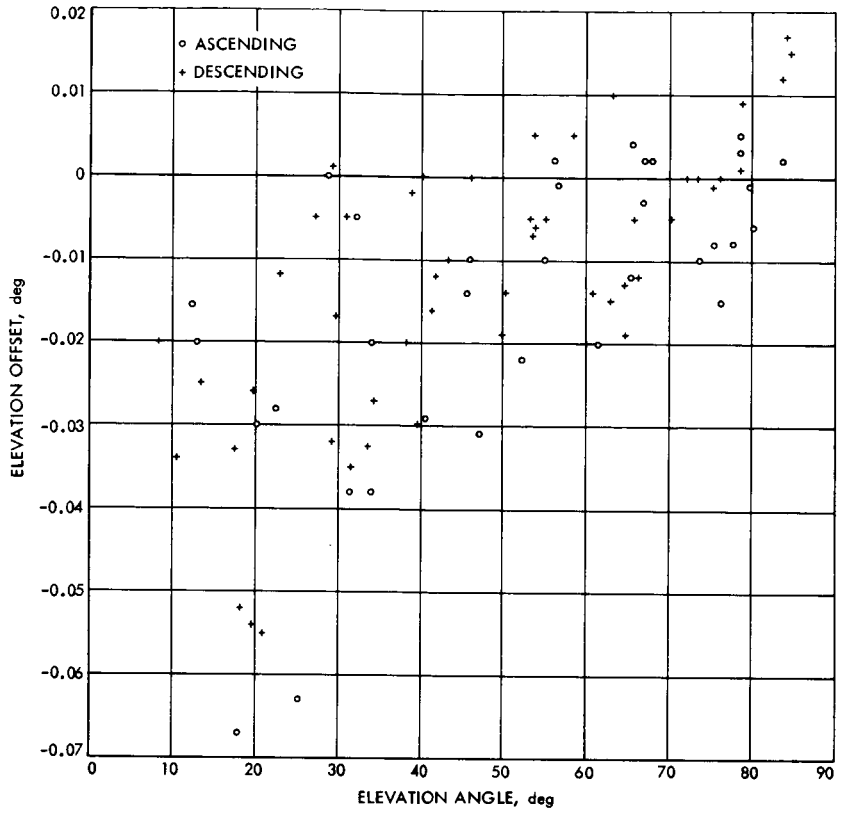

Fig. 4. Elevation offsets vs elevation angle (Cygnus-A, 85-ft antenna, 8448 MHz)

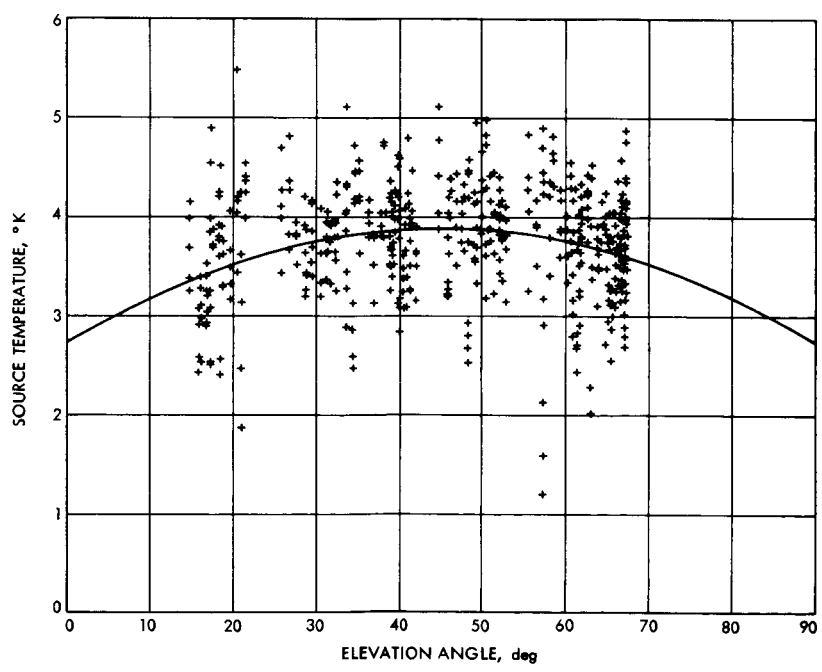

Fig. 5. Source temperature vs elevation angle (Virgo-A, 85-ft antenna, 8448 MHz)

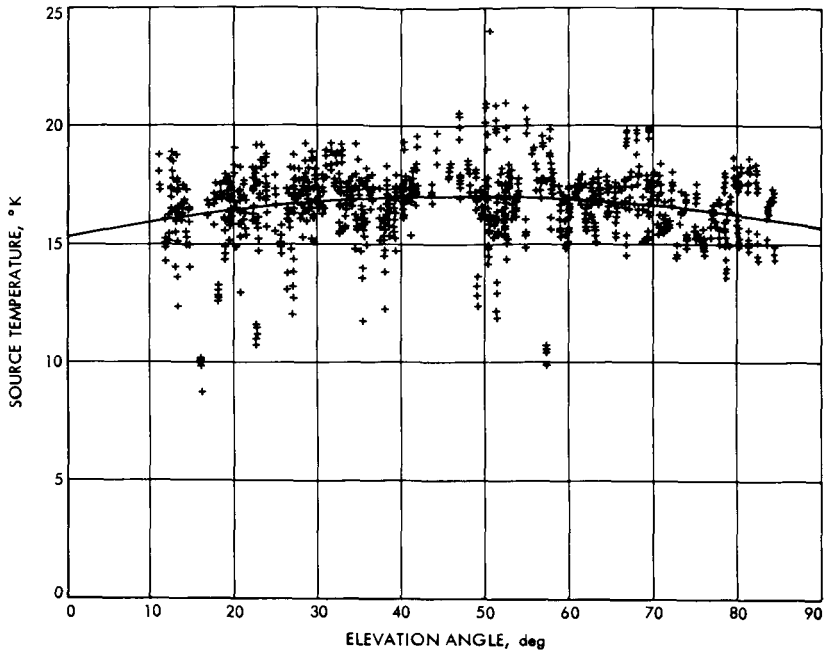

Fig. 6. Source temperature vs elevation angle (Cygnus-A, 85-ft antenna, 8448 MHz)

D. Efficient Antenna Systems: X-Band Gain Measurements, 210-ft AAS, *D. A. Bathker*

1. Introduction

In February 1968, a series of RF tests at X-band, 8448 MHz, was made on the advanced antenna system (AAS) at the Mars DSS. A previous reporting (SPS 37-52, Vol. II, pp. 78–86) outlined the methods used to predict the overall RF system efficiency as well as showing overall measured efficiency. This article will show overall measured efficiency for the individual radio sources used and will discuss the assumed flux values, source sizes, and beam correction factors. Finally, the rms surface tolerance is obtained from the radio measurements and compared with the predicted.

2. Radio Source Characteristics

Three nonthermal sources, 3C123, 3C274, and 3C405, were selected as primary flux standards for the 210-ft antenna X-band evaluation. Factors affecting these choices were:

(1) Strength—sources producing a 5°K or greater change in antenna temperature were sought.

(2) Visibility—sources producing a wide range of elevation angles were sought.

(3) Distribution—point sources were desired. In the absence of stable point sources meeting the above criteria, sources with moderate beam correction factors were sought.

Table 2 gives the source sizes, distributions, and flux values accepted for the advanced antenna system X-band evaluation. The beam correction factors and the antenna temperature increase for a 100% efficient 210-ft antenna operated at 8.448 GHz are given. Note that for 3C123 and 3C274 the beam correction factors are small. In the case of Cygnus-A, 3C405, the double source separation is nearly the half power beamwidth of the antenna. For this reason, the beam correction factor is large (nearly −2 dB) and, therefore, possibly unreliable in the case of antenna beamwidth changes with elevation angle, for example. Cygnus-A was retained, however, because of previous observations as an 85-ft antenna calibrator at the same wavelength.

Table 2 also gives a derived 8.448-GHz flux for the variable 3C273 based on temperature measurements made during focussing tests. The planet Venus was used as a calibrator, although the observed temperature increase (Fig. 7) is characterized as rather scattered. The mean value of 2.4°K at a 25-deg elevation angle is consistent with the other measurements, indicating the assumed

Table 2. Source characteristics at 8448 MHz (epoch 1968.1)

Characteristic	Source			
	3C123	3C273	3C274	3C405
Type	2-dimensional gaussian	Quasar	1-dimensional gaussian	2 points
Size, arc sec	20	Point	1 × 45	116-arc-sec separation
8.448-GHz flux S, $W/M^2 \cdot Hz \times 10^{26}$	9.4	42.5 (variable)	42	187.6
Spectral index	−0.86	—	−1.02 halo −0.44 core	−1.2
[a]Beam correction C_s	1.021	1.000	1.055	1.56
[b]Antenna temperature T_A 100%, °K	10.7	49.5	46.4	140.1

[a]137-arc-sec half-power beamwidth selected.
[b]T_A 100% = 1.1655 S/C_s, S in f.u. (flux units).

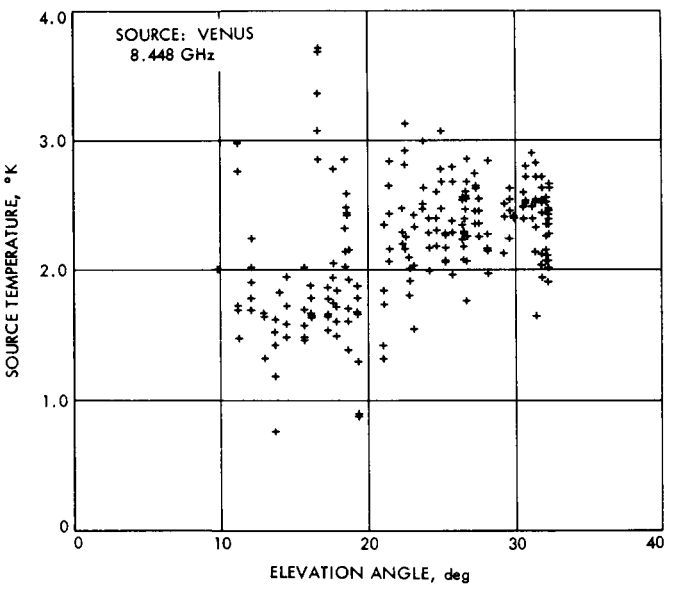

Fig. 7. Source temperature vs elevation angle (XCE feed, 210-ft AAS)

600°K blackbody is not in serious error. The planet Jupiter, subtending approximately 44-arc-sec compared with the 137-arc-sec beamwidth, was found to produce an observed temperature increase of 9.3°K at 45-deg elevation.

Figures 8a, b, and c show the X-band 210-ft antenna system efficiency obtained, based on the flux values accepted in Table 2, using 3C123, 3C274, and 3C405, respectively. Although the weakest of the three, 3C123 was given priority on the basis of a superior source distribution. Individual best-fit curves are in good agreement.

Based on computed RF optics efficiencies obtained previously (SPS 37-52, Vol. II, pp. 78–86) and the 3C123 data in Fig. 8a, Fig. 9 was derived. Figure 9 gives the mean and standard deviation limits for the rms surface tolerance as determined from the radio measurements. The standard deviation limits include only the measurement scatter. Figure 9 includes the predicted rms surface tolerance points based on the work of M. S. Katow (Ref. 1, also SPS 37-52, Vol. II, pp. 86–92). To obtain the radio data shown in Fig. 9, it is necessary to sort out the atmospheric loss contribution. This was done by accepting the usual flat earth secant law, which is applicable above about a 10-deg elevation angle, and by accepting a selected 0.036-dB atmospheric loss when pointing at zenith.

As Fig. 9 shows, the radio measurements indicate a better surface tolerance than expected at zenith; however, the horizon surface tolerance appears somewhat worse. This is a sensitive function of the selected zenith loss, however, and preliminary calculations indicate a selected value of 0.055 dB at zenith with the secant dependence will force perfect agreement between predicted and measured rms data at 10-deg elevation.

Zenith losses of 0.055 and 0.036 dB are shown in Fig. 10, which compares calculated and measured total operating temperatures. Both calculations assume an effective physical temperature of 290°K for the atmosphere. Using an improved density weighted average for the effective physical temperature, 0.060 dB and 260°K yield the same agreement as 0.055 dB.

It is concluded that the zenith attenuation, based on Fig. 10, is approximately 0.055 dB, and the surface tolerance near horizon, based on Fig. 9 with 0.055-dB zenith

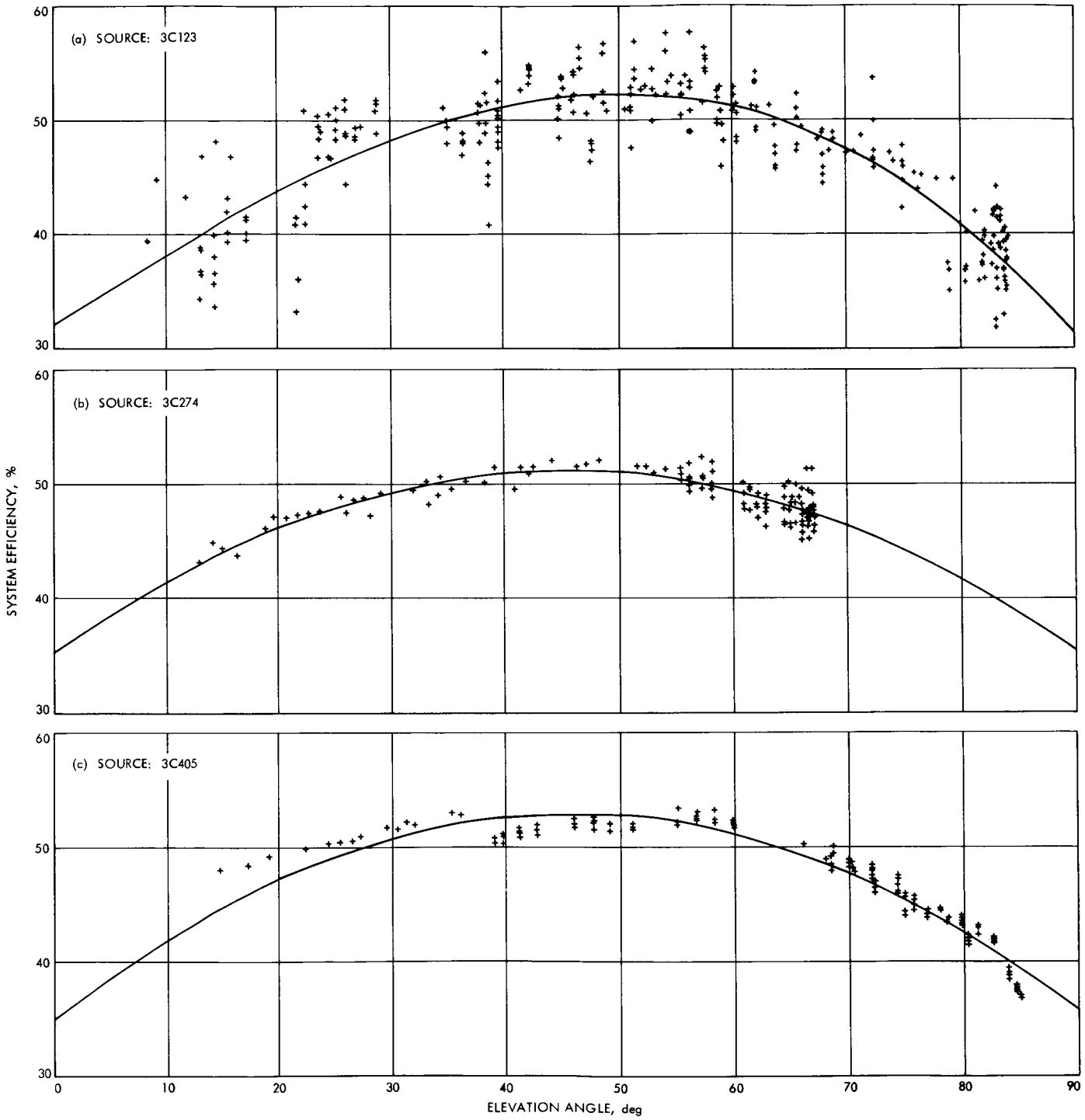

Fig. 8. System efficiency vs elevation angle (XCE feed, 210-ft AAS, 8.448 GHz)

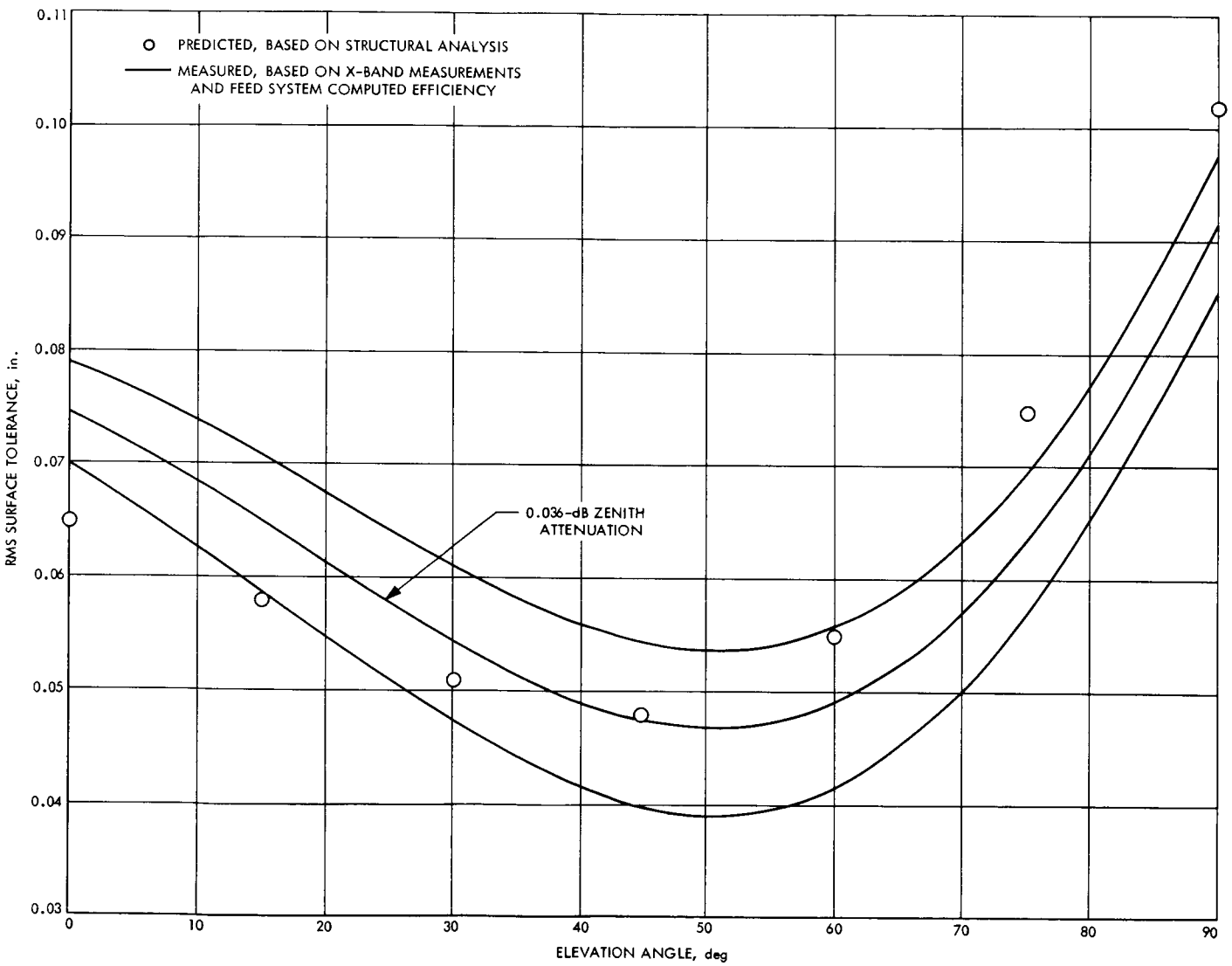

Fig. 9. Computed and measured surface tolerance vs elevation angle (XCE feed, 210-ft AAS)

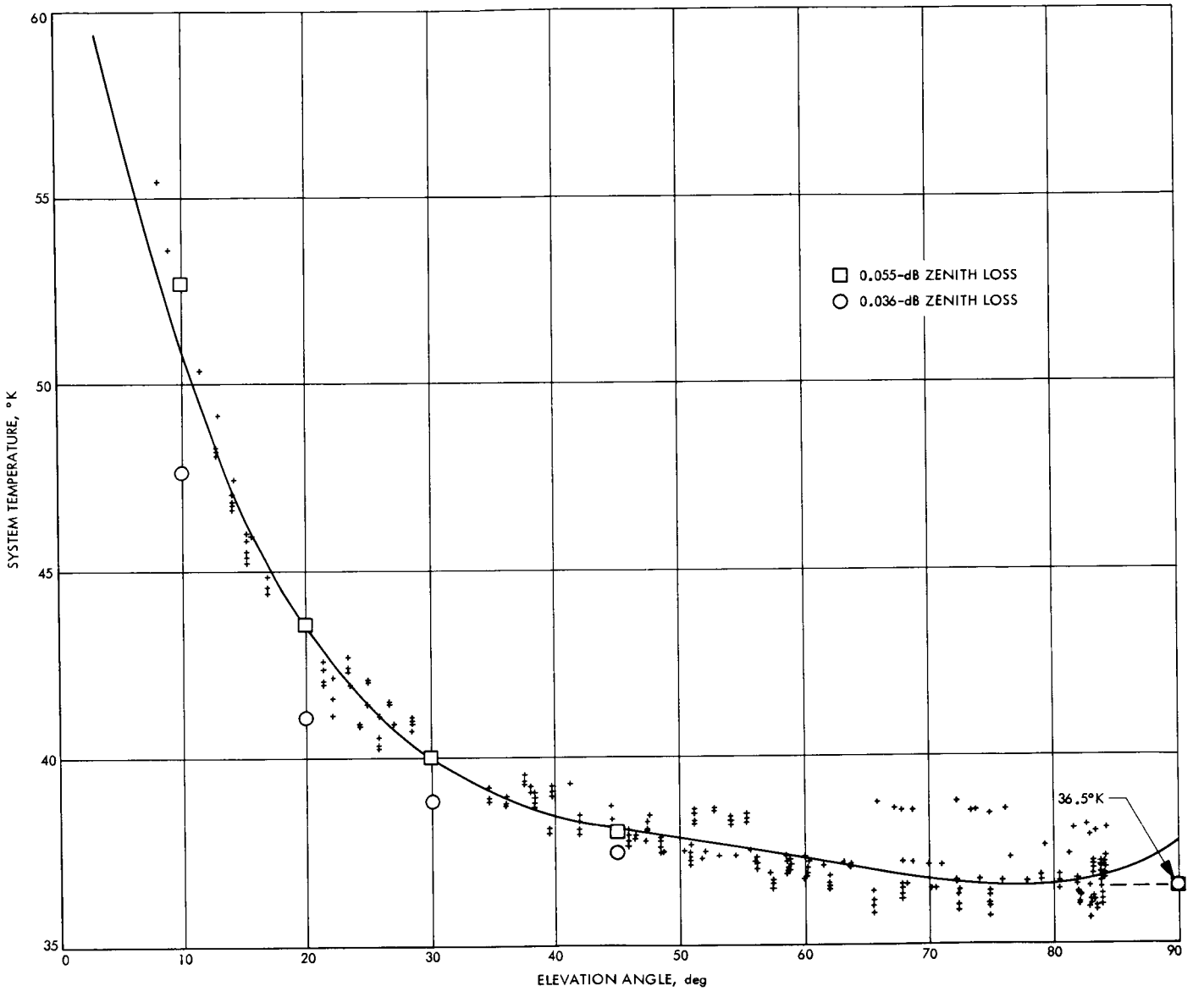

Fig. 10. System temperature vs elevation angle (XCE feed, 210-ft AAS, 8.448 GHz)

attenuation, is essentially that calculated by structural means (Ref. 1).

Reference

1. Katow, M. S., "Techniques Used to Evaluate the Performance of the NASA/JPL 210-Ft Reflector Structure Under Environmental Loads," presented at the International Symposium on Structures Technology for Large Radio and Radar Telescope Systems, Massachusetts Institute of Technology, Cambridge, Mass., Oct. 18–20, 1967.

E. Efficient Antenna Systems: Comparison of the Calculated Gain of the AAS With a Unicone Feed to the Gain With a Tricone Feed,

S. A. Brunstein

1. Introduction

An asymmetrical cassegrainian feed system using three feed cones (tricone) has been proposed for the advanced antenna system (AAS) (SPS 37-45, Vol. III, pp. 48–51). The tricone would replace the present feed system (unicone), which is symmetrical about the parabola axis and uses a single cone. The tricone would have three cones mounted simultaneously on the AAS in such a manner that any one of the three could be made the operational feed for the AAS in a matter of minutes. Previously, the change from one operational cone to another required the complete dismounting of one cone and the remounting of another. This procedure took the better part of a day. Thus, the primary advantage of the tricone is the speed with which configuration changes can be made, and the resultant enhancement of multimission capability.

An analysis of the comparative gain of the AAS with each system has been performed for a frequency of 2295 MHz. To date, the analysis has only been conducted for circular, dual-mode horns of the type presently used on the AAS. The analysis was performed in two ways. One approach utilized primarily theoretical calculations while the other made greater use of experimental data. This article reports the analytical techniques applied and the results of the analysis.

2. Analytical Techniques and Results

The overall analysis was based on techniques previously developed for symmetrical cassegrainian systems (SPS 37-42, Vol. III, pp. 37–40) with suitable modifications for the asymmetrical tricone. The analysis made use of a number of computer programs that were previously developed for the performance analysis of symmetrical antenna systems (Ref. 1). In addition, use was made of a scattering program for asymmetrical configurations recently developed by Ludwig (Ref. 2).

The analysis was begun by integrating the measured pattern of the AAS multifrequency feedhorn to determine the percentage of radiated power that was intercepted by the unicone subreflector and by the tricone subreflector. The same horn pattern was then input to the Rusch symmetrical scattering program and the Ludwig asymmetrical scattering program. These programs computed the theoretical scattered pattern from the unicone and tricone subreflectors, respectively. The unicone scattered pattern was then used to calculate the aperture efficiency for the main reflector.

At the same time, the method of Ruze (Ref. 3) was used to calculate the gain loss due to structural deviations of the antenna from the desired shape. These calculations, in conjunction with the useful percentage of horn radiated power, were used to calculate an expected gain for the AAS, neglecting the effect of aperture blockage by the subreflector support structure (quadripod). At the present state of the art, the effect of quadripod blockage can only be estimated. Since the preceding analysis is firmly based on accepted practice, the estimate of quadripod blockage loss was made by comparing the computed gain with the measured gain for the unicone system (SPS 37-44, Vol. III, pp. 100–105). The comparison gave a quadripod gain loss figure of 0.83 dB. (It is interesting to note that this corresponds to a loss of aperture area of 1.4 times the physical cross section of the quadripod.) This estimate of quadripod loss was then used throughout the remainder of the analysis. Analyzing the expected gain for the AAS with the tricone, including the effect of quadripod loss, gave a gain loss of 0.06–0.08 dB over the unicone configuration.

While these analytical calculations were being performed, measurements were being made of the scattered pattern from ½ scale models of the unicone and tricone subreflectors. A comparison of typical computed and measured amplitude and phase patterns is shown in Figs. 11 and 12. The agreement between the predicted and measured patterns is considered outstanding. The measured patterns were then used to again calculate the AAS gain for the unicone and tricone configurations. For this calculation, the gain loss for the tricone was 0.07–0.09 dB over the unicone.

The gain based on the experimental pattern for the unicone subreflector was 0.10 dB less than for the theoretical pattern value. The same comparison for the tricone

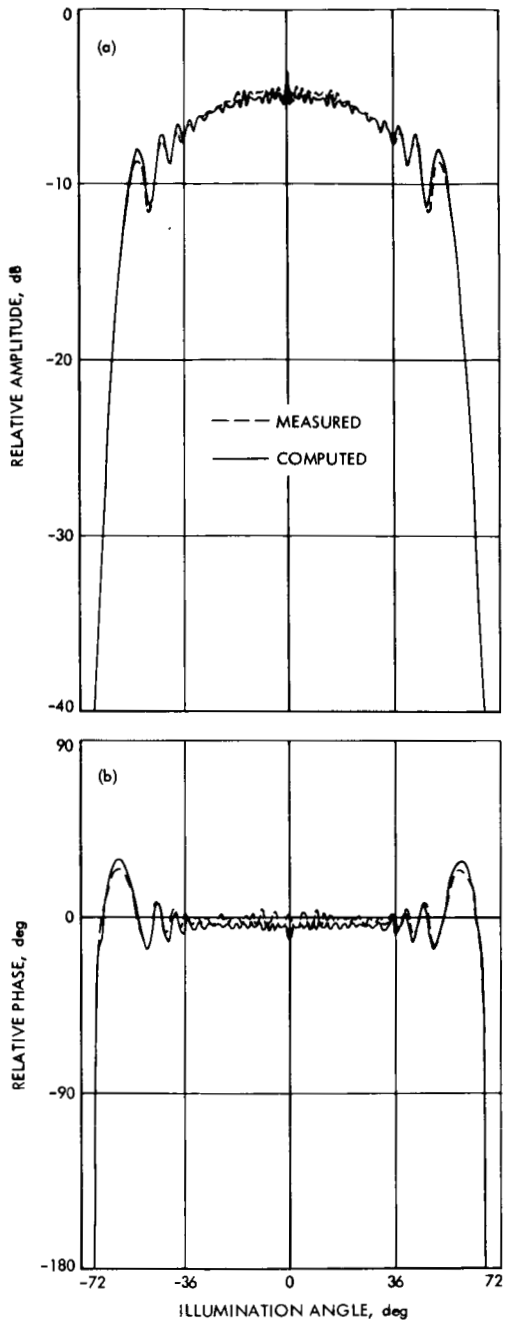

Fig. 11. AAS unicone feed typical measured and computed patterns: (a) relative amplitude vs illumination angle, (b) relative phase vs illumination angle

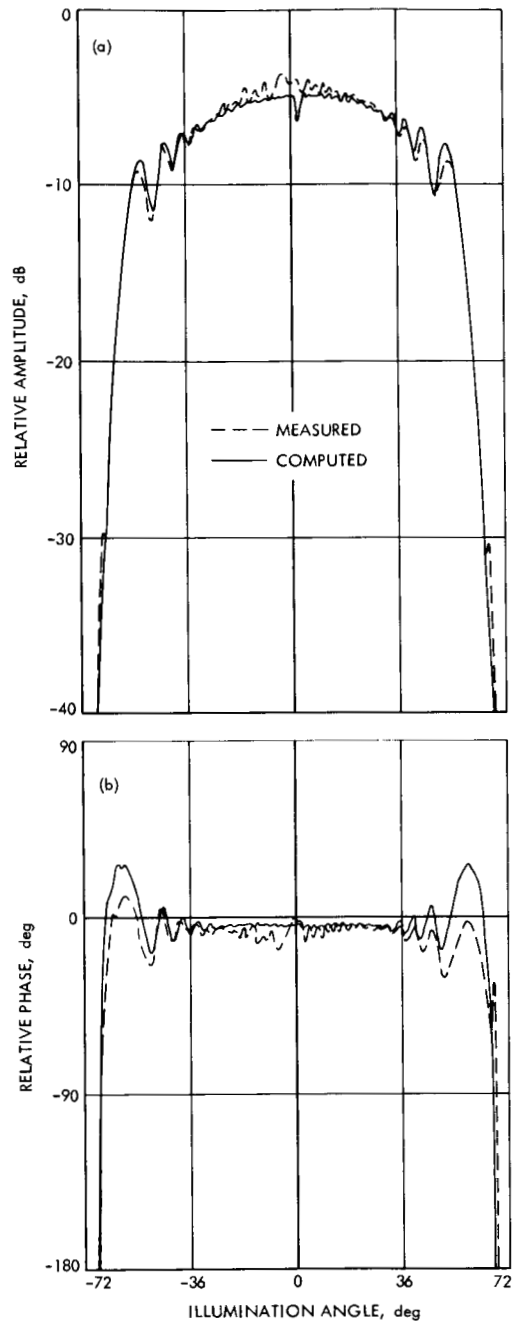

Fig. 12. AAS tricone feed typical measured and computed patterns: (a) relative amplitude vs illumination angle, (b) relative phase vs illumination angle

showed a similar difference of 0.11 dB. It is felt that the difference represents a consistent pattern measurement error on the antenna range, and the close agreement of the performance difference between the unicone and tricone is the important consideration. The most likely cause of such a consistent error would be reflections from the structure used to support the subreflector and horn during pattern measurement. Table 3 gives the calculated AAS gain for each configuration and technique.

Based on the above results, it is felt that the gain loss of the tricone over the unicone is negligible in comparison to the operational advantages.

Table 3. Calculated gains for the AAS

Elevation angle, deg	Theoretical pattern		Measured pattern	
	Unicone gain, dB	Tricone gain, dB	Unicone gain, dB	Tricone gain, dB
0	61.48	61.41	61.38	61.30
45	61.62	61.56	61.52	61.45
90	61.39	61.31	61.29	61.20

References

1. Ludwig, A., *Computer Programs for Antenna Feed System Design and Analysis, Volumes I and II*, Technical Report 32-979. Jet Propulsion Laboratory, Pasadena, Calif., Apr. 15, 1967.

2. Ludwig, A., "Computation of Radiation Patterns Involving Double Numerical Integration," *IEEE Trans. Ant. Prop.*, Nov. 1, 1968.

3. Ruze, J., "Antenna Tolerance Theory—A Review," *Proceedings of the IEEE*, Vol. 54, No. 4, Apr. 1966.

F. *Pioneer VI* Faraday Rotation Solar Occultation Experiment, *G. S. Levy, C. T. Stelzried, T. Sato, and B. L. Seidel*

1. Introduction

In the second half of November 1968, the *Pioneer VI* probe's orbit resulted in a line of sight from the probe to the earth that caused the RF signal to pass through the solar corona and to be occulted by the sun. The polarization of the *Pioneer* probe is linear, and it is spin-stabilized with respect to the plane of the ecliptic. The plane of polarization of the signal received from the *Pioneer VI* spacecraft was measured. Faraday rotation produced by the interaction of the RF signal with the solar corona will be inferred from those measurements.

2. Experiment

On September 18, the modified multifrequency cone was reinstalled on the 210-ft antenna at the Mars DSS. The modifications are described in SPS 37-53, Vol. II, pp. 69–71. Essentially, these modifications permitted closed-loop tracking of the angle of the plane of polarization. The initial installation permitted manual positioning of the polarizer and the obtaining of an error signal. Initially, data was taken manually. The plane of polarization was deduced by observing the time-of-error-signal zero crossing for a given position of the polarizer. On October 26, the polarization servo tracking loop was closed and auto-tracking data of the plane of polarization of the signals received from *Pioneer VI* was obtained. During this time, the effects of the diurnal variations of the earth's ionosphere were clearly observed.

Figure 13 shows the data taken on October 31. The time in day number is plotted against the measured spacecraft polarization angle with respect to the plane of the ecliptic. The dark line in the beginning of the tracking period occurred before acquisition. The polarizer was stationary. However, since the antenna is azimuth–elevation mounted, a coordinate transformation occurred and the polarizer angle relative to the plane of the ecliptic was moving, even though the servo was locked down to its position relative to the antenna.

At 305.70, auto-tracking commenced and the noisiness of the data can be seen. Points were taken at fixed intervals of 10 s. These points were recorded on digital tape and then put through an IBM 7094 program to perform the appropriate coordinate transformation. The dark line at approximately 305.94 is due to temporary loss of lock, and the servo was inactive during that period of time. This is fairly normal looking data recorded after the coordinate transformation was performed but before any further processing.

Figure 14 shows an event which occurred on November 4 for a period of approximately 2 h. Normal polarization, which was approximately 97 deg (due to the combination of the spacecraft's orientation of 90 deg to the plane of the ecliptic and the earth's ionospheric effects of approximately 7 deg) swung dramatically to approximately 65 deg. This event occurred when the line of sight to the spacecraft was at approximately 10 solar radii from the limb of the sun. Several other events were also observed during the experiment. As the line of sight approached the solar limb, what appeared to be a steady-state rotation seemed to occur. This data is now being processed and will be interpreted.

On November 17, the last signals were obtained as the line of sight approached the sun. The solar side lobes caused large increases in system temperature at the same time the solar corona caused spectral broadening. These two effects made it impossible to track any further. From November 21 to 25, the spacecraft was physically occulted by the sun. It was not possible to reacquire the spacecraft signal until November 29. From November 29 through December 8, the spacecraft was again tracked. On December 8, the experiment was terminated.

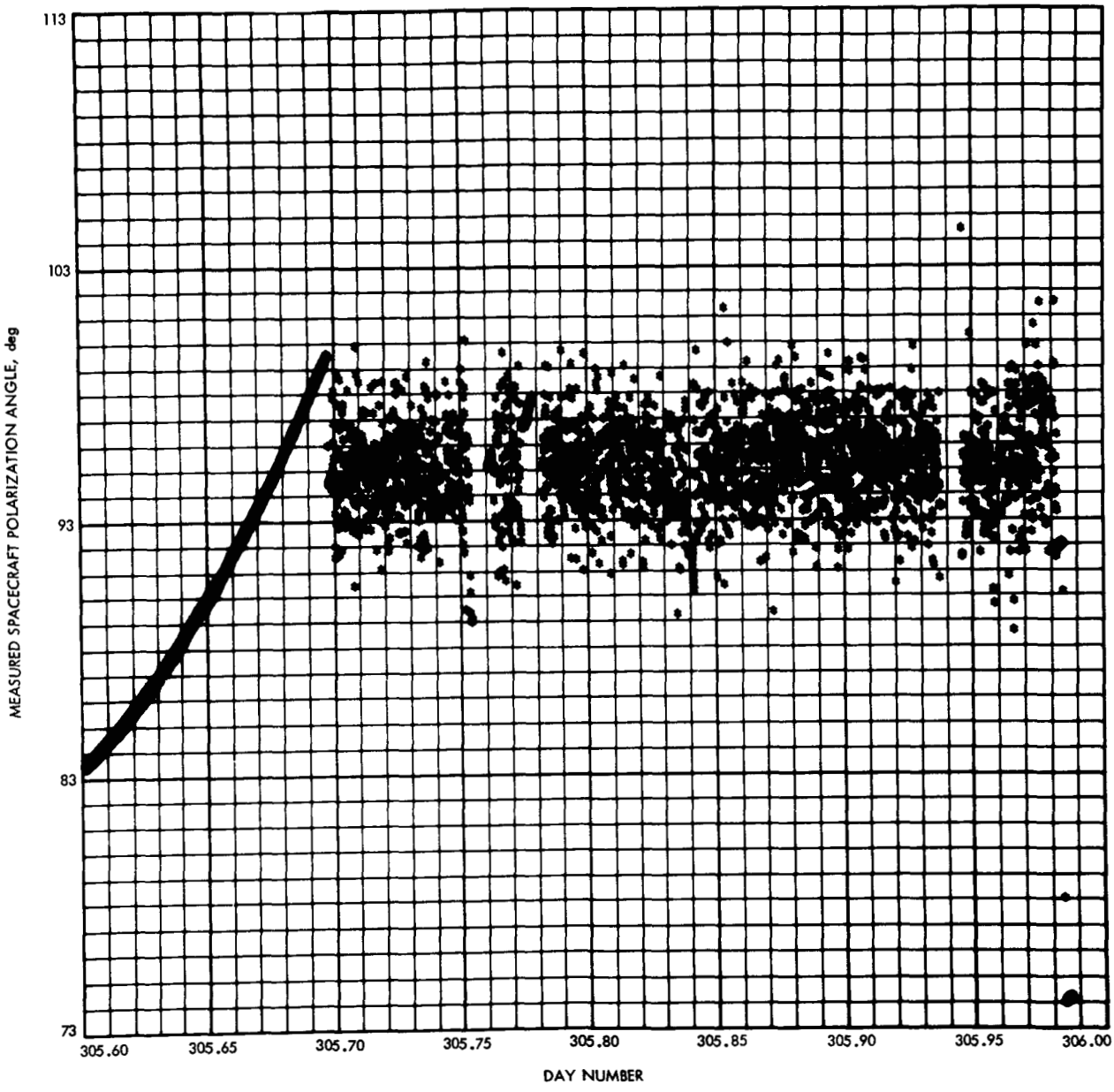

Fig. 13. PN-6 signal polarization closed-loop data (Oct. 31, 1968)

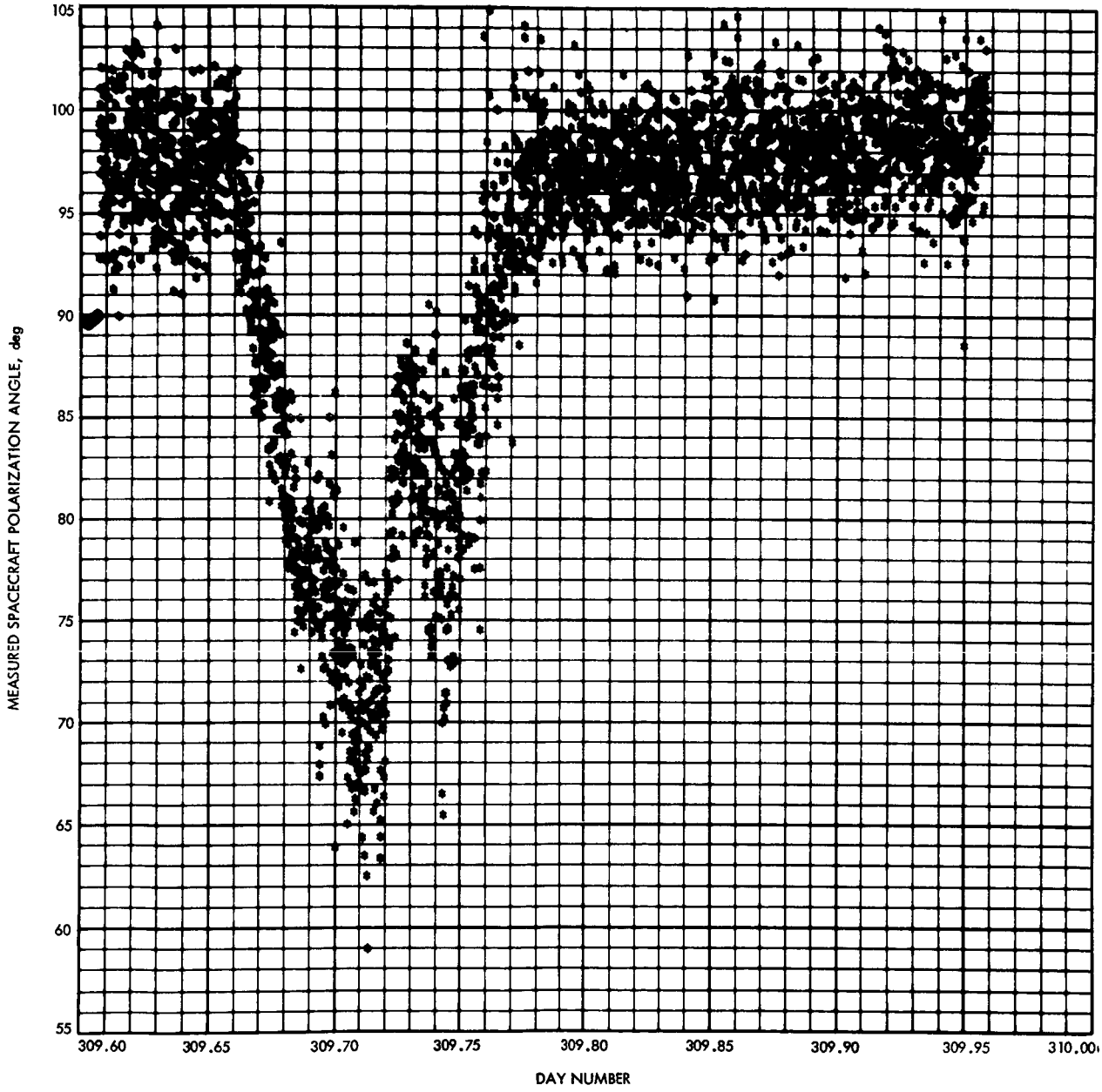

Fig. 14. PN-6 signal polarization closed-loop data (Nov. 4, 1968)

VI. Advanced Engineering: DSN Programming

A. Mission-Independent Telemetry Decommutation, *S. Mandell and F. Lesh*

1. Introduction

The objective of this research is to discover decommutation methods of sufficient generality that the decommutation program in the input/output processor in the SFOF could be made mission-independent. If this can be done, then only tables describing data formats would have to be changed from one mission to another and a great deal of program redevelopment cost could be eliminated.

It is hopeless to seek an algorithm that would decommutate a data stream with any format and any type of data transmission errors. But if one defines a class F of possible data formats and a class E of allowable errors, then it may be possible to develop an algorithm capable of decommutating any data stream with a format in F and errors in E. If F and E can be defined broadly enough, then such an algorithm might be applicable to the decommutation of actual data streams at JPL.

2. Approach to be Tried

Class F will be defined by describing a language L_1 in which the data format must be describable. The set of statements in L_1 that describe the data format will be called the *format description*. Class E will be defined by listing the types of allowable errors and the ranges of the parameters involved in their description. A language L_2 will be developed in which the "content" of the data can be described. The pseudonoise (PN) sequence, for example, might occur in several adjacent telemetry words. The data content description for these words would simply say that the content should be a given sequence of bits with high probability. The content of a given telemetry word might be a counter that increments by one in each successive word. The content description would have to somehow state that fact.

A *frame pointer* is defined as an indicator that points to a bit in the telemetry stream which is hoped to be the first bit of a frame of data. *Pseudo-correlation* is some numerical measure of similarity between the actual data bit stream and a simulated data stream generated from the format and content description. This similarity will depend on having the frame pointer set to the right bit.

The basic approach will be to seek frame synchronization by shifting the frame pointer until the pseudo-correlation between the simulated and actual data streams is maximized.

3. Progress

Class E has been tentatively established and a rather primitive language L_1 has been developed in which data formats can be described. A set of simple Fortran programs, which process language L_1 and generate appropriate sequence of telemetry data channels, has been examined. These programs are not much different in general approach from a set of ASI 6050 programs written in machine language for *Mariner* Mars 1969 telemetry processing. The class of allowable error types, the method of format description with the language L_1, and the subroutines for processing that language are described below.

4. Class E of Allowable Data Errors

Data bar. Data bar exists when all 1's have been received as 0's and vice versa. This happens when the phase detector of the receiver locks on the carrier 180 deg out of phase. The transition probability p_1 is the probability per bit of the telemetry going from the data state to the data bar state, or vice versa. This probability would normally range from 10^{-4} to 10^{-8}.

Bad bits. Isolated bits may be received incorrectly. Conditions may exist in the receiver that cause 1's to be received as 0's with one probability p_2, but 0's to be received as 1's with another probability p_3. Normally both p_2 and p_3 might range from 10^{-2} to 10^{-5}.

Missing or added bits. The receiver may drop a bit with a probability per received bit of p_4 or add a bit with probability per received bit of p_5. Both p_4 and p_5 would normally range from 10^{-4} to 10^{-8}.

Random data. If phase lock is lost in the receiver, bits will continue to be generated in almost exactly the right rate. They will be equally likely to be 0's or 1's. The probability per bit p_6 of losing lock would normally be much less than the probability per bit p_7 of regaining lock. Reasonable ranges might be $10^{-4} \geq p_6 \geq 10^{-6}$ and $10^{-1} \geq p_7 \geq 10^{-2}$.

Having established the allowable error types in class E, the probabilities $p_1, \cdots, p_7$ define the error statistics. These probabilities are a function of the signal-to-noise ratio. The values given above are typical of normal operation, and could be greatly degraded in an anomalous situation.

5. Mariner Mars 1969 Commutator

Figure 1 is a schematic of the *Mariner* Mars 1969 commutator and Fig. 2 shows the channel addresses in 40 subframes produced by that commutator (reading from left to right). Channel address 100 in Fig. 2 is considered to contain the 15-bit PN sequence so channel 101 is not listed. Deck 210 is subcommutated in channel 104 of deck 100. Decks 400 and 410 are in turn subcommutated to channel 211 of deck 210. The effect of this subcommutation on the sequencing of transmitted data can be seen from Fig. 2. Note that, in order to have sent data from each commutator segment at least once, a total of 4000 (or $20 \times 10 \times 20$) channels must be sent. This number of channels is called a "frame" of data. Each line in Fig. 2 is one subframe.

6. Language L_1

Language L_1 is intended to be adequate to describe the method in which channel addresses are sequenced in telemetry data. The *Mariner* Mars 1969 format is taken to be typical of the allowable data formats. Language L_1 consists of the following instructions:

PUT N, M. This instruction means "output the channel address N and the number of its bits M." For example, we generate the first two channels of deck 100 in Fig. 1 with the instructions

```
PUT  100,15
PUT  102,6
```

CAL J. This instruction is used when a channel is subcommutated. The program calculates the next channel number by processing the appropriate instruction out of the commands for deck J.

REP N, M, J. This instruction is shorthand for a set of PUT instructions. Instead of writing

```
PUT  100,7
PUT  101,7
PUT  102,7
  :
PUT  109,7
```

the single REP (repeat) instructions

```
REP  100,7,10
```

can be used.

END. This instruction indicates the end of the commands for a given commutation deck.

FIN. This instruction signals the end of all commands for a commutator.

The set of instructions in L_1 that completely define *Mariner* Mars 1969 engineering telemetry is shown in Table 1. The command sequences for the individual decks must be in the same order as the deck numbers themselves. Only 26 commands are needed to completely specify the sequencing produced by this commutator.

Table 1. Language L_1 instructions for *Mariner* Mars 1969 commutator

Deck	Instruction in L_1
1	PUT 100,15
	PUT 102,6
	CAL 2
	CAL 3
	REP 105,7,5
	CAL 4
	REP 111,7,9
	END
2	REP 200,7,2
	CAL 7
	REP 203,7,7
	END
3	PUT 210,7
	CAL 6
	CAL 5
	REP 213,7,7
	END
4	REP 220,7,10
	END
5	REP 420,7,20
	END
6	REP 400,7,20
	END
7	REP 300,7,10
	END
	FIN

7. Subroutines PROCES and COMUTE

Subroutines PROCES and COMUTE have been developed to accept commands in L_1 and output channel addresses and the associated number of bits. COMUTE operates interpretively on the PUT, CAL, and REP commands, and outputs one channel address and the associated number of bits each time it is called. The relationship between PROCES and COMUTE is illustrated in Table 2.

Since COMUTE is written entirely in Fortran IV, it is most convenient for its input to be a sequence of integers, one to a computer word. For this reason, a PUT instruction is encoded as a 1, a CAL as a 2, a REP as a 3, etc.

Table 2. Input commands for PROCES and COMUTE

PROCES	COMUTE
PUT 100,15	1
	100
	15
PUT 102,6	1
	102
	6
CAL 2	2
	2
CAL 3	2
	3
REP 105,7,5	3
	105
	7
	5

It is most convenient for the user to input commands by simply punching them one to a card as shown on the left side of Table 2.

PROCES was written to read commands from cards in this format and to output a sequence of integers as shown on the right side of Table 2 for input to COMUTE. This sequence of integers is stored in a memory array named COMAND. In order for COMUTE to interpret this sequence of integers, it must know where in the sequence the commands for each deck begin. This information is stored in the beginning of the COMAND array by PROCES. PROCES also gives appropriate diagnostics if any detectable errors are made in the Hollerith input cards.

PROCES consists of 163 Fortran IV statements that compile into 1048 computer locations. However, PROCES need only be in memory during initialization. COMUTE, which is active during execution, consists of only 51 Fortran IV statements and compiles into 255 locations.

In order to control the positioning of the simulated commutator, COMUTE has two special entries. Entry WHIRL enables the user to advance any deck to any given commutator segment without disturbing the deck to which it is subcommutated, if any. Entry RESET enables the user to reset the entire commutator to its initial point. The calling sequences for the subroutines are

```
CALL PROCES (COMAND)

CALL COMUTE (COMAND,CHAN,NBITS)
    CALL WHIRL (COMAND,J,CHAN)
    CALL RESET (COMAND)
```

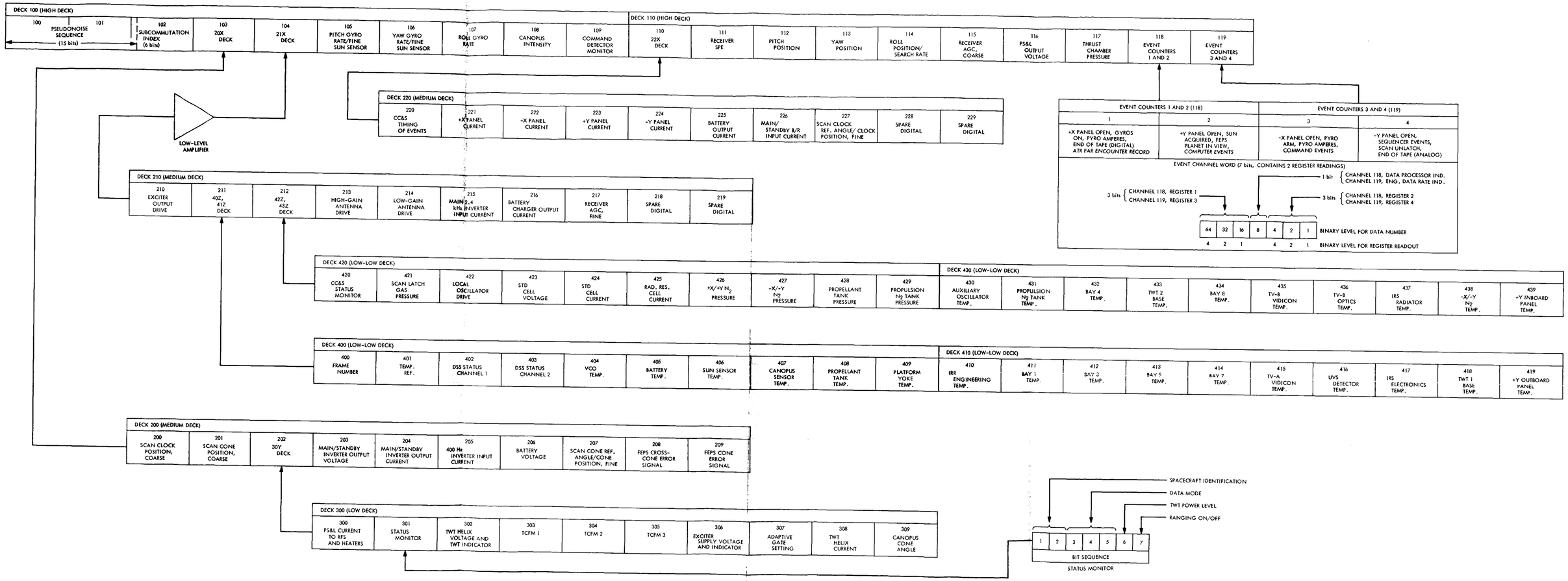

Fig. 1. *Mariner Mars 1969 commutator diagram*

			DECK 200	DECK 210						DECK 220									
	100	102	200	210	105	106	107	108	109	220	111	112	113	114	115	116	117	118	119
DECK 400	100	102	201	400	105	106	107	108	109	221	111	112	113	114	115	116	117	118	119
	100	102	300	420	105	106	107	108	109	222	111	112	113	114	115	116	117	118	119
DECK 300	100	102	203	213	105	106	107	108	109	223	111	112	113	114	115	116	117	118	119
	100	102	204	214	105	106	107	108	109	224	111	112	113	114	115	116	117	118	119
	100	102	205	215	105	106	107	108	109	225	111	112	113	114	115	116	117	118	119
	100	102	206	216	105	106	107	108	109	226	111	112	113	114	115	116	117	118	119
	100	102	207	217	105	106	107	108	109	227	111	112	113	114	115	116	117	118	119
	100	102	208	218	105	106	107	108	109	228	111	112	113	114	115	116	117	118	119
	100	102	209	219	105	106	107	108	109	229	111	112	113	114	115	116	117	118	119
	100	102	200	210	105	106	107	108	109	220	111	112	113	114	115	116	117	118	119
	100	102	201	401	105	106	107	108	109	221	111	112	113	114	115	116	117	118	119
	100	102	301	421	105	106	107	108	109	222	111	112	113	114	115	116	117	118	119
DECK 420	100	102	203	213	105	106	107	108	109	223	111	112	113	114	115	116	117	118	119
	100	102	204	214	105	106	107	108	109	224	111	112	113	114	115	116	117	118	119
	100	102	205	215	105	106	107	108	109	225	111	112	113	114	115	116	117	118	119
	100	102	206	216	105	106	107	108	109	226	111	112	113	114	115	116	117	118	119
	100	102	207	217	105	106	107	108	109	227	111	112	113	114	115	116	117	118	119
	100	102	208	218	105	106	107	108	109	228	111	112	113	114	115	116	117	118	119
	100	102	209	219	105	106	107	108	109	229	111	112	113	114	115	116	117	118	119
	100	102	200	210	105	106	107	108	109	220	111	112	113	114	115	116	117	118	119
	100	102	201	402	105	106	107	108	109	221	111	112	113	114	115	116	117	118	119
	100	102	302	422	105	106	107	108	109	222	111	112	113	114	115	116	117	118	119
	100	102	203	213	105	106	107	108	109	223	111	112	113	114	115	116	117	118	119
	100	102	204	214	105	106	107	108	109	224	111	112	113	114	115	116	117	118	119
	100	102	205	215	105	106	107	108	109	225	111	112	113	114	115	116	117	118	119
	100	102	206	216	105	106	107	108	109	226	111	112	113	114	115	116	117	118	119
	100	102	207	217	105	106	107	108	109	227	111	112	113	114	115	116	117	118	119
	100	102	208	218	105	106	107	108	109	228	111	112	113	114	115	116	117	118	119
	100	102	209	219	105	106	107	108	109	229	111	112	113	114	115	116	117	118	119
	100	102	200	210	105	106	107	108	109	220	111	112	113	114	115	116	117	118	119
	100	102	201	403	105	106	107	108	109	221	111	112	113	114	115	116	117	118	119
	100	102	303	423	105	106	107	108	109	222	111	112	113	114	115	116	117	118	119
	100	102	203	213	105	106	107	108	109	223	111	112	113	114	115	116	117	118	119
	100	102	204	214	105	106	107	108	109	224	111	112	113	114	115	116	117	118	119
	100	102	205	215	105	106	107	108	109	225	111	112	113	114	115	116	117	118	119
	100	102	206	216	105	106	107	108	109	226	111	112	113	114	115	116	117	118	119
	100	102	207	217	105	106	107	108	109	227	111	112	113	114	115	116	117	118	119
	100	102	208	218	105	106	107	108	109	228	111	112	113	114	115	116	117	118	119
	100	102	209	219	105	106	107	108	109	229	111	112	113	114	115	116	117	118	119

Fig. 2. ***Mariner* Mars 1969 subcommutation sequence**

In each of these calling sequences, COMAND is the name of the array containing the commutator commands. Since this name appears in each calling sequence, it is possible for this set of programs to simulate several commutators simultaneously. CHAN is the channel address and is an output variable for COMUTE, but an input variable for WHIRL. NBITS is the number of bits associated with channel CHAN and is an output variable in COMUTE. The J is the deck number and is an input variable to WHIRL. WHIRL and RESET have no outputs; their effect is to modify the contents of the COMAND array in such a way as to have the desired effect on the later outputs of COMUTE.

The commutator output channel sequence of Fig. 2 was produced by this set of subroutines using the commutator description of Table 1.

Thus far, the commutator that has a prescribed format F has been simulated. The next phase of this research will be the development of an algorithm that decommutates, in a mission-independent way, telemetry with errors of class E present.

B. Data Recovery From a Noisy Telemetry Channel: An Algorithm to Smooth Doubly Contaminated Data, *R. Lewis*

1. Introduction

At the receiver end of some telemetry systems, a phase-modulated subcarrier is multiplied by a sinusoidal reference of the same frequency. The reference phase is either the same as that of the phase-modulated subcarrier or

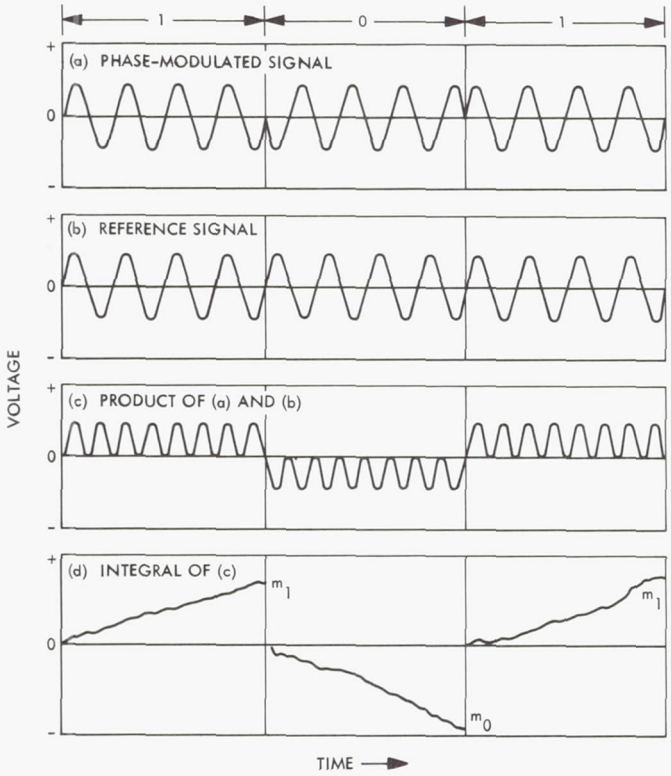

Fig. 3. Phase modulation

180 deg different (see Fig. 3). The product is integrated over one bit time. If the output of the integrator is positive, the bit is taken to be a 1; if negative, a 0. Figure 3 illustrates this situation when the subcarrier is noise-free. If the magnitude of the noise on the phase-modulated signal begins to approach the magnitude of the signal itself, the output of the integrator must be treated as a random variable with some variance σ^2. If the bit being received is a 0, the mean of the integrator output will be m_0; if the bit is a 1, the mean will be m_1. Because the integrator output is a random variable, 1's and 0's will sometimes be mistaken for each other. The magnitude of the integrator output gives some indication of the likelihood of this happening. If the integrator output is zero, for instance, it is equally likely to have been caused by a 1 or a 0.

Two assumptions have been made for this study:

(1) Many values of a telemetered variable (such as tank pressure), which vary in a smooth, polynomial-like way over time, are received at equally separated times.

(2) The bits representing these values are themselves represented by the integrator outputs rather than just the signs of these outputs.

A computer algorithm has been developed to determine the correct bits from the integrator outputs and from the knowledge that correctly interpreted telemetered information must represent a smooth function.

2. A Mathematical Model

Assume that the transmitted variable $y(t_i)$ can be represented as the sum of a low order polynomial $p(t_i)$ and a measurement error ϵ as follows:

$$y_i = y(t_i) = p(t_i) + \epsilon$$

$$p(t) = a_1 + a_2 t + a_3 t^2 + \cdots + a_{k+1} t^k$$

$$t_i = t_0 + i\Delta t, \qquad i = 1, \cdots, m$$

where $p(t)$ has been normalized such that $0 \leq p(t) < 1$ for all $t \in [t_1, t_m]$ and where ϵ is normally distributed with mean 0 and variance σ_y^2. The variable y_i is converted into n bits $b_{ij}, j = 1, \cdots, n$, so that

$$y_i = .b_{i1} b_{i2} \cdots b_{in} = \sum_{j=1}^{n} \frac{b_{ij}}{2^j}$$

The bits b_{ij} $(i = 1, \cdots, m;\ j = 1, \cdots, n)$ are transmitted. If $b_{ij} = 0$, the integrator output u_{ij} (a voltage) received is a random sample from a normal population with mean m_0 and variance σ_0^2. If $b_{ij} = 1$, u_{ij} is a random sample from a normal population with mean m_1 and variance σ_1^2 (see Fig. 4).

Even though $y_i = p(t_i) + \epsilon$ and is therefore continuous, its binary representation is discrete. It is the discrete b_{ij} and not the continuous y_i that are transmitted. Therefore, y_i will be rounded off to n bits of accuracy and will be considered discrete. The symbol y_i will henceforth refer to

$$\sum_{j=1}^{n} \frac{b_{ij}}{2^j}$$

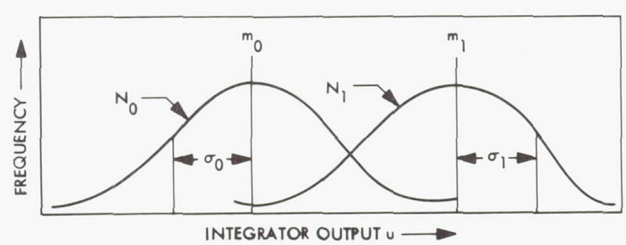

Fig. 4. Distribution of integrator output

In practice, $\sigma_0 = \sigma_1$. The possibility of inequality was considered in the interests of generality.

Given k, m, n, t_0, Δt, m_0, σ_0, m_1, σ_1, σ_y, and $\{u_{ij}\}$, the problem is to find the set $S = \{a_r, b_{ij} | r = 1, \cdots, k+1; i = 1, \cdots, m; j = 1, \cdots, n\}$ such that the likelihood function is maximized. The values of t_0 and Δt are arbitrary in the sense that the shape of the estimator curve $\tilde{p}$ will be the same for any initial time and constant interval of time between successive measurements, but the coefficients of $\tilde{p}$ do depend on the actual t_0 and Δt.

a. The likelihood function. The likelihood function L is a function of the coefficients of p and the bits. If we let

$$\mathbf{A} = (a_1, a_2, \cdots, a_{k+1})$$

and

$$B = \begin{pmatrix} b_{11} b_{12} & \cdots & b_{1n} \\ b_{21} b_{22} & \cdots & b_{2n} \\ \vdots \quad \vdots & & \vdots \\ b_{m1} b_{m2} & \cdots & b_{mn} \end{pmatrix}$$

then $L = L(\mathbf{A}, B)$. For the remainder of this article, L is considered to be a function of the bit matrix B only; i.e., $L = L(B)$. Inconsistency is avoided by defining the function $f: B \rightarrow \mathbf{A}$ according to

$$f(B) = \text{the } \mathbf{A}$$

such that

$$\left\{ \sum_{i=1}^{m} \left[\mathbf{A} \cdot \mathbf{T}_i - \left(\sum_{j=1}^{n} \frac{b_{ij}}{2^j} \right) \right]^2 \right\}$$

is minimized, where $\mathbf{T}_i = (1, t_i, t_i^2, \cdots, t_i^k)$. Then $L(B)$ is really $L[f(B), B] = L(\mathbf{A}, B)$. The coefficient vector $\mathbf{A}$ is nothing more than the least-squares coefficient vector; this is more easily recognized if we note that

$$p_i = p(t_i) = \mathbf{A} \cdot \mathbf{T}_i$$

and

$$y_i = \sum_{j=1}^{n} \frac{b_{ij}}{2^j}$$

Then $f(B) =$ the $\mathbf{A}$ such that

$$\sum_{i=1}^{m} (p_i - y_i)^2$$

is minimized.

The probability π_i of observing u_{ij} and of having these u_{ij} come from the y_i (for a given i), given $\mathbf{A} = \{a_r\}$, is given by

$$\pi_i = P(y_i | p_i) \prod_{j=1}^{n} P(u_{ij} | b_{ij})$$

where $p_i = p(t_i)$. Integrator output u_{ij} actually is a transmitted representation of b_{ij}, but b_{ij} is uniquely determined for a given j by the value of y_i.

It can be shown that

$$L = \prod_{i=1}^{m} \pi_i = \prod_{i=1}^{m} \frac{\exp[-(y_i - p_i)^2/2\sigma_y^2]}{\sigma_y (2\pi)^{1/2}} \times \prod_{j=1}^{n} \frac{\exp[-(u_{ij} - m_{b_{ij}})^2/2\sigma_{b_{ij}}^2]}{\sigma_{b_{ij}} (2\pi)^{1/2}}$$

The first set of factors of L is similar to the likelihood function for the standard least-squares problem.[1] The second set of factors of L is an extension that is necessary because of the transmission error.

Let

$$Q = a \ln L + b = -\sum_{i=1}^{m} \left(\frac{y_i - p_i}{\sigma_y} \right)^2 - \sum_{i=1}^{m} \sum_{j=1}^{n} \left(\frac{u_{ij} - m_{b_{ij}}}{\sigma_{b_{ij}}} \right)^2 - \sum_{i=1}^{m} \sum_{j=1}^{n} 2 \ln \sigma_{b_{ij}}$$

If L is maximized, $\ln L$ and $a \ln L + b$, where a and b are constants ($a > 0$), will also be maximized. Therefore, we turn our attention to the maximization of Q (which will henceforth be referred to as a likelihood for the sake of notational simplicity).

If $\sigma_0 = \sigma_1$, the last set of terms is not needed; it is a constant. In fact, it is the general case that $\sigma_0 = \sigma_1$; the

[1]Solloway, C., *Elements of the Theory of Orbit Determination*, Section VIII, Dec. 1964 (JPL internal document).

transmission error is a function of such things as distance and transmitting power and is not a function of what is transmitted.

b. Distribution of Q. Since

$$\left(\frac{y_i - p_i}{\sigma_y}\right) \qquad \text{and} \qquad \left(\frac{u_{ij} - m_{b_{ij}}}{\sigma_{b_{ij}}}\right)$$

are normally distributed with mean 0 and variance 1, $|Q|$ is the sum of $m(n+1)$ elements of the form ϵ^2, where $\epsilon \sim n(0,1)$. Therefore, if $\sigma_0 = \sigma_1$, $|Q|$ is distributed as a chi-square variate with $m(n+1)$ degrees of freedom. As such, it has mean $m(n+1)$ and variance $2m(n+1)$. Thus, the likelihood of the supposed maximum likelihood estimator (MLE) of $\{a_r, b_{ij}\}$ can itself be evaluated by comparison with the expected value of Q.

3. The Nature of the Problem's Difficulties

One source of difficulty is that the measurement error affects points and the transmission error affects bits. Thus, the two types of error must be considered separately; they cannot be "lumped."

A second source of difficulty is that Q is defined on a lattice (in m space, with 2^n possible values along each axis). As such, Q lacks continuity, and no algorithm that does not try every combination of b_{ij} can guarantee an absolute maximum of Q. The 2^{mn} possible combinations of b_{ij} make it necessary to restrict our search to some subset of all combinations of $\{b_{ij}\}$. It is this restriction that prevents the guarantee of an absolute maximum by the algorithm. However, the algorithm does yield a local maximum (in the sense that no change of a single bit will improve Q).

The solution determined by the algorithm has a likelihood Q associated with it. Since $|Q| \sim \chi^2(m(n+1))$ if $\sigma_0 = \sigma_1$, we know approximately what likelihood will be associated with the true MLE for $\{a_r, b_{ij}\}$. If the algorithm's Q is near the expected value of Q, the solution probably has been found.

Even if $\sigma_0 \neq \sigma_1$, the value of Q can still be subjectively evaluated by adding to Q the term

$$x(2 \ln \sigma_0) + (mn - x)(2 \ln \sigma_1)$$

where x is the number of 0 bits in the MLE of $\{b_{ij}\}$.

4. The Solution

a. An initial guess. The initial guess mechanism selects $k+1$ evenly spaced points $z_1, \cdots, z_{k+1}$ out of the m data points such that (1) these $k+1$ points span as much of the interval as possible, and (2) the first data point is z_1. One specific value of the form $s/2^n$ (where s is an integer such that $0 \leq s < 2^n$) will be selected for each z_i; these $k+1$ values will be used to uniquely determine a polynomial $\tilde{p}(t)$ of degree k. A value of the form $s/2^n$ has associated with it a specific bit configuration.

This estimate $\tilde{p}(t)$ of $p(t)$ is then tested. If it passes all tests (described below), it becomes our initial guess. If it fails any test, a new set of values for the z's is tried.

The values of the z's are selected as follows: since each z_i is a data point, its value is represented by n bit representations $u_{rj}, j = 1, \cdots, n$ for some r. The 2^n possible values of z_i are ranked in decreasing likelihood order, where the likelihood referred to is that of the u_{rj} being generated by the value. Combinations of the values of $z_1, \cdots, z_{k+1}$ are then ranked in decreasing likelihood order.

The actual ordering is only an approximation of likelihood order. Exact likelihood order could be achieved but is not worth the time it would take to improve on the approximation. The approximation is attained by testing all combinations of the three most likely values of z_i, $i = 1, \cdots, k+1$, then all untried combinations of the six most likely values, and then all untried of the nine most likely values, etc., until all $2^{n(k+1)}$ combinations have been rejected.

When all possible combinations of z_i have been tested and no initial guess accepted, the routine uses as its initial guess the choice one would make if he were examining each u_{ij} individually and selecting the most likely value (0 or 1) for each bit. For example, if $m_0 = -10$, $m_1 = 10$, and $\sigma_0 = \sigma_1 = 10$, any u_{ij} above 0 is said to represent a 1, and any below, a 0.

Combinations of z_i are tested by first interpolating the m numbers $\tilde{p}(t_i)$. If any one violates the boundary condition $0 \leq \tilde{p}(t_i) < 1$, then $\tilde{p}$ cannot be an estimator of p and the combination is rejected.

Second, the $\tilde{p}(t_i)$ values are rounded off to n bit accuracy; while $\tilde{p}(t_i)$ can be calculated to any desired degree of accuracy, n bits are all that is transmitted. When y_i is

compared with $\tilde{p}(t_i)$ to find the measurement error of our guess, numbers of similar accuracy should be compared.

Third, the m data points are scanned one at a time, with several operations being performed on each point. The bit configuration which maximizes

$$Q_i = -\left[\frac{y_i - \tilde{p}(t_i)}{\sigma_y}\right]^2 - \sum_{j=1}^{n}\left(\frac{u_{ij} - m_{b_{ij}}}{\sigma_{b_{ij}}}\right)^2$$

the likelihood associated with the ith point, is calculated and added to the total likelihood Q of all points thus far examined. That bit configuration $b_{i1}b_{i2} \cdots b_{in}$ is then used to define y_i. If the point being considered is one of the $k+1$ points $z_1, \cdots, z_{k+1}$ used to define $\tilde{p}$, then the first term of Q_1 is 0 and the maximum likelihood bit configuration is the binary representation of the value of that z_i.

After operations on each point are performed, Q is tested to see if it is too low. (The meaning of "too low" is discussed in *Subsection 5-a*.) If Q is too low, the combination (of z's) is rejected.

b. Improvement of initial guess. The initial guess is in the form of a vector

$$\mathbf{Y} = (y_1, y_2, \cdots, y_m)$$

and associated matrix of bits

$$B = \begin{pmatrix} b_{11} b_{12} & \cdots & b_{1n} \\ b_{21} b_{22} & \cdots & b_{2n} \\ \vdots \quad \vdots & & \vdots \\ b_{m1} b_{m2} & \cdots & b_{mn} \end{pmatrix}$$

For any vector $\mathbf{Y}$ a set of coefficients $\mathbf{A} = (a_1, \cdots, a_{k+1})$ of $\tilde{p}(t)$ is uniquely determined by least-squares analysis; i.e., $\mathbf{A}$ is the vector that minimizes

$$\sum_{i=1}^{m} (y_i - \tilde{p}_i)^2$$

The improvement process changes the first bit (from 1 to 0 or from 0 to 1) of each point in turn, calculating new $\mathbf{Y}$, $\mathbf{A}$, and Q at each trial change. (Many of the actual computations involved here need only be done once; therefore, these calculations are not particularly time-consuming.) The change that improves the likelihood Q the most is accepted. The process is repeated until there is no change in the first column of B that improves Q.

The above procedure is repeated for the second, third, and nth bits (columns of B).

At this point, there is a user option (see *Subsection 5-e*). If option 0 is selected, the improvement process stops here. If option 1 is selected, the entire process is repeated until Q remains unchanged over two successive of these grand repetitions.

5. Experiments and Results

A subroutine MAXLIK was developed for the IBM 7094 to apply this algorithm to specific cases. Tests were run by generating random numbers from a normal population (according to JPL subroutine GAUSS) to simulate the effects of measurement and transmission errors on data from known polynomials.

The experiments were conducted using seven as the only value of n (number of bits).

a. Variations in v: balancing two time consumers. The quantity v is an input parameter to MAXLIK that is used, in determining an initial guess, to set a lower limit to the acceptable value of the likelihood Q of a potential initial guess. After evaluating the likelihood at r points, $|Q|$ has mean $\mu = r(n+1)$ and standard deviation $\sigma = (2\mu)^{1/2}$. If $Q < -\mu - v\sigma$, it is considered to be too far from what the likelihood of the solution would be; therefore, that combination is rejected as an initial guess. If $Q \geqq -\mu - v\sigma$, the combination is considered further.

If v is high, the initial guess mechanism will accept one of the first combinations it tries; little time will be spent searching for an initial guess but much time may be spent improving it. If v is low, the initial guess mechanism will accept the first combination that meets rigid standards of acceptability. It is possible, however (if v is too low), for all combinations to be rejected. This would prove very time consuming. If, for instance, $\tilde{p}$ is a cubic and $n = 7$, $2^{n(k+1)} = 128^4$ combinations must be rejected. Clearly, then, v can be made so low that time is not saved by decreasing it.

The algorithm does provide a means of yielding an initial guess that is independent of v. In the event that higher values of v yield unsatisfactory results and lower values of v are unable to settle on an acceptable initial guess in a reasonable period of time, the user may insert a statement (as indicated in the deck itself), the execution of which will result in the initial guess one would logically make by merely looking at the bit representation

data matrix u. (This type of "best guess" was introduced in *Subsection 4-a.*)

The results of trial runs using various values of v can be found in Table 3, where

m = number of data points

σ_y = standard deviation of measurement error

$$R = \frac{m_1 - m_0}{\sigma_0 + \sigma_1} = \frac{60 - 40}{10 + 10} = 1 \text{ in all experiments}$$

$$p(t) = 0.61 + 0.13t - 0.07t^2 + 0.01t^3 \text{ in experiments 1–17}$$

$$p(t) = 0.8 - 2.39t + 2.68t^2 - 1.01t^3 + 0.12t^4 \text{ in experiments 23–26}$$

$$\sigma_{\tilde{p},p} = \left\{ \frac{\int_{t_1}^{t_m} [p(u) - \tilde{p}(u)]^2 \, du}{t_m - t_1} \right\}^{1/2}$$

The user should be able to determine his own best v from these data.

Table 3. Variation in v[a]

Experiment	v	m	σ_y	Q	Number of combinations tested	Running time, s	$\sigma_{\tilde{p},p}$
1	1.5	10	0.005	−75.18	3	2.65	0.1501
2a[b]	1.5	10	0.01	−71.94	4	3.42	0.0190
2b[c]	1.5	10	0.01	−68.81	4	5.92	0.0152
3	1.5	10	0.02	−83.04	21	5.57	0.1390
4	1.5	10	0.05	−56.26	1	2.88	0.1088
9	1.5	25	0.005	−189.61	16	9.77	0.0347
10	1.5	25	0.01	−189.64	100	15.40	0.0048
11	1.5	25	0.02	−219.41	273	35.38	0.0356
12	1.5	25	0.05	−134.91	19	23.23	0.0677
17	1.5	100	0.02	−682.94	19	204.48	0.0134
23	1.5	25	0.005	−215.94	255	24.82	0.0441
24	1.5	25	0.01	−189.97	31	13.38	0.0198
25	1.5	25	0.02	−152.07	1	28.05	0.0154
26	1.5	25	0.05	−156.07	1	18.35	0.0389
13	1.0	25	0.005	−189.61	18	9.88	0.0347
14	1.0	25	0.01	−193.16	1336	63.50	0.0050
15	1.0	25	0.02	−203.12	906	64.60	0.0397
16	1.0	25	0.05	−134.91	19	23.27	0.0677
5	0.5	10	0.005	−68.39	16	2.82	0.2563
6	0.5	10	0.01	−68.48	97	6.28	0.0285
7	0.5	10	0.02	−67.16	46	6.58	0.0334
8	0.5	10	0.05	−56.26	1	2.88	0.1088

[a]Results same when MNOP = 0 and 1, except in experiment 2.
[b]MNOP = 0.
[c]MNOP = 1.

b. The point error: variations in σ_y. One would expect that the lower σ_y is, the less will be the root-mean-square deviation $\sigma_{\tilde{p},p}$ of $\tilde{p}$ (our estimate) from p (the true curve). The root-mean-square deviation is equal to

$$\left[\frac{\sum_{i=1}^{m} (p_i - \tilde{p}_i)^2}{m} \right]^{1/2}$$

Because it is desirable that $\tilde{p}$ fit p well over the entire interval $[t_1, t_m]$ and not just at the m points $t_1, t_2, \cdots, t_m$, the continuous version of this deviation was used. Thus,

$$\sigma_{\tilde{p},p} = \left\{ \frac{\int_{t_1}^{t_m} [p(x) - \tilde{p}(x)]^2 \, dx}{t_m - t_1} \right\}^{1/2}$$

While the experiments were unable to determine the existence of a relationship between $\sigma_{\tilde{p},p}$ and σ_y, other relationships were suggested.

Within "reasonable" limits, variations in σ_y are much less significant than the number of data points and the transmission error (see Tables 3 and 4). The likelihood Q is also more significant than σ_y. Q can be thought of as a measure of the trust to be placed in an estimate $\tilde{p}$; an excellent Q and a poor σ_y may well yield a better fit (lower $\sigma_{\tilde{p},p}$) than a poor Q and a low σ_y.

Table 4. Variation in R[a]

Experiment	R	Q	Number of combinations tested	Running time, s	$\sigma_{\tilde{p},p}$
18	$\frac{20 - (-20)}{10 + 10} = 2.0$	−181.24	2	10.65	0.0031
19	$\frac{5 - (-5)}{10 + 10} = 0.5$	−182.12	1	13.50	0.3745
20	$\frac{8 - (-8)}{10 + 10} = 0.8$	−226.31	274	32.85	0.1562
21	$\frac{60 - 40}{15 + 5} = 1.0$	−981.15	10	13.07	0.1709
22	$\frac{1 - 0}{1 + 9} = 0.1$	−720.20	1	46.93	0.2937
27	$\frac{5 - (-5)}{10 + 10} = 0.5$	−162.55	1	9.00	0.0903

[a]$M = 25$; $\sigma_y = 0.02$; $v = 1.5$; $p(t) = 0.61 + 0.13t - 0.07t^2 + 0.01t^3$; results same when MNOP = 0 and 1.

Experiments varying σ_y also indicate that σ_y can be too small. If $\sigma_y = 1/2^n$, the subroutine that improves the initial guess will be more concerned with reducing

$$\sum_{i=1}^{m} (y_i - \tilde{p}_i)^2$$

than in considering what was transmitted. This can be seen more clearly if we consider $\sigma_y = 2^n \cdot 10^{-10}$. A deviation $|y_i - \tilde{p}_i|$ from the curve of only $1/2^n$ (an error in the last bit) will contribute

$$-\left[\frac{2^{-n}}{2^{-n} \cdot 10^{-10}}\right]^2 = -10^{20}$$

to Q. Clearly, the routine will change that last bit so that $y_i = \tilde{p}_i$ regardless of what was transmitted.

In practice, the routine will not accept values of σ_y less than 2^{-n}, but will instead increase σ_y such that $\sigma_y = 2^{-n}$. Even with σ_y as large as this, however, it is still small enough that the effects of a small σ_y appear in $\sigma_{\tilde{p},p}$.

c. The bit error: how distinct are the two normal curves? One of the purposes of MAXLIK was to determine how low the signal-to-noise ratio could be and still permit the transmission of meaningful data. Experiments varying the parameters of the transmission error were conducted with this goal in mind.

Let $R = (m_1 - m_0)/(\sigma_0 + \sigma_1)$. R is related to the signal-to-noise ratio and varies with it; it is also a measure of the separation of the two curves in Fig. 4. The results of experiments varying R can be found in Table 4. Since these experiments used far fewer data points than normally available, and since the transmission noise used was far greater than that which normally occurs, the conclusion is that R can be quite low and yet the data can be meaningful in the sense that they can be reconstructed fairly accurately.

A "crossover bit" is defined as follows: Let x be the voltage at which N_0 and N_1 (in Fig. 4) intersect, $m_0 < x < m_1$. A crossover bit is a transmitted 0 whose representation is greater than x, or a transmitted 1 whose representation is less than x. The expected percentage of crossover bits as a function of R is tabulated for several values of R in Table 5.

d. The number of data points relative to the assumed degree of the polynomial. We now consider the ratio m/k (k = degree of $\tilde{p}$). From experiments summarized in Tables 3 and 4, it could be tentatively concluded that a ratio of 3.3 is almost large enough to reconstruct the bits and estimate p, that a ratio of 8 to 10 provides enough points to give a fairly good curve fit (low $\sigma_{\tilde{p},p}$), and that enough points to yield a ratio of 25 or 30 gives high accuracy but is expensive in terms of machine time.

Table 5. Crossover bits as a function of R

R	$C(R)^a$
0.5	31.0
0.8	21.0
1.0	16.0
2.0	2.3
3.0	0.14

[a] $C(R)$ = expected percentage of crossover bits to transmitted bits.

e. Speed vs precision (MNOP). One of the input parameters to MAXLIK is MNOP. This variable affects the improvement process. When MNOP = 0 (option 0 in *Subsection 4-a*), the improvement routine will only run through the bits once, looking for possible bit changes. When MNOP = 1 (option 1), the routine will continue examining the bits until one complete sweep with no improvement in Q is made. Thus, the routine is slightly faster but may be less precise when MNOP = 0.

The final solution in 16 of 17 experiments was identical when MNOP = 0 and 1. With 10 data points, the second option required an average of 1.05 additional seconds; with 25 data points, 6.25 extra seconds. The one experiment in which different solutions were obtained was experiment 2 (Table 3).

An example of a MAXLIK curve fit is illustrated in Fig. 5, where

$$p(t) = 0.8 - 2.39t + 2.68t - 1.01t^3 + 0.12t^4$$

$$\tilde{p}(t) = 0.7581 - 2.119t - 2.2901t^2 - 0.8199t^3 + 0.0902t^4$$

Other data relevant to this example can be found in Table 3 (experiment 25).

6. Conclusions

MAXLIK seems to have achieved its primary goal of smoothing doubly contaminated data. As a secondary goal, it was also demonstrated that meaning can be derived from poorly transmitted data.

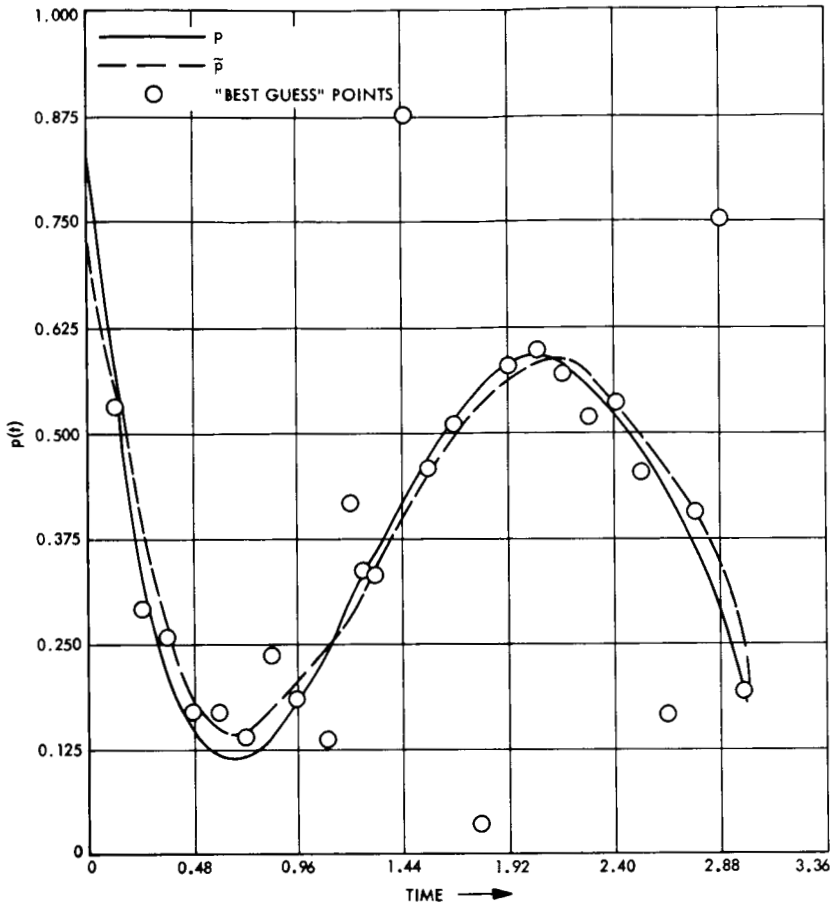

Fig. 5. Sample MAXLIK curve fit

VII. DSIF Development and Operations

A. Surveillance TV Camera for Monitoring Antenna Area, *C. Lundy*

The present Mark II tracking system configuration at the DSIF stations does not allow the antenna servo operator to view the ground area under the antenna for equipment and personnel. This condition constitutes not only a hazardous operating condition for the antenna structure, but also a personnel safety problem.

A solution was sought which would be effective under both night and daytime conditions. One such solution is a surveillance TV system to monitor the antenna area.

TV camera assemblies were set up and tested at possible surveillance locations at the Pioneer DSS. The Kintel 2000 series camera with 10:1 zoom lens and pan and tilt assembly offers the best overall configuration for the intended purpose. Only one camera per station is necessary because of the full view afforded by the open gridwork of the HA–dec antenna structures. The single camera configuration is sufficient to allow the operator to view the entire antenna structure and area with the exception of a small blind spot on the opposite side of the declination room or declination skid, depending on the antenna's position. The 10:1 zoom lens also allows the operator to close in on given areas with sufficient clarity and resolution to ascertain personnel safety.

Present antenna illumination does not afford sufficient nighttime visibility, and the antenna-structure mounted lights constitute hot spots which burn the vidicon tube at maximum sensitivity settings. However, a very satisfactory solution has been found to this problem. Light intensity was tested after the camera was located at one of the light towers, shields placed over the antenna structure lights, and the towers furnished with higher-intensity bulbs (1000 W). The camera needs at least 4.0 ft-cd incident light intensity on the scene for an adequate picture, and the light towers afford, with 1000-W bulbs, about 12 ft-cd incident intensity. The hot-spot problem was eliminated as a result of the shielding and the increase in the area ambient light level, bringing the hot spots within the 10,000-to-1 contrast capabilities of the Kintel system.

The camera assembly should be located about 150 ft from the antenna pedestal center, 15 to 20 ft off the ground, and at about 70 $\pm$ 20 deg from north.

To fulfill the servo operator's needs, the configuration of the monitor control system should be as follows:

(1) The screen should be located directly in front of the servo operator in such a way that it can be viewed from any operator position.

(2) The screen should be 14 in. wide.

(3) The monitor controls should be locked so that the system cannot be turned off or down during antenna operations.

(4) The surveillance TV system should be interlocked with the servo console so that it comes on first, thus restricting the servo operator from moving the antenna until the TV system is in operation.

B. Antenna-Surface Thermal Deflection Study,

V. B. Lobb and M. Kron

1. Introduction

A study of thermally caused antenna surface deflections was made to determine their magnitude and effect on rms surface distortion, boresight shift, and focal length change. The Pioneer DSS 85-ft HA–dec antenna was measured with the reflector in the zenith position so that gravity distortions would not complicate the measurements. Measurements were taken over a 17-h period each day for 13 days from before sunrise to after sunset. Targets mounted on the surface were optically read, the data recorded, and the rms surface distortion computer-calculated. The reduced data were evaluated for cyclic trends and maximum variations in rms surface distortion, boresight shift, and focal length change with respect to variations in solar energy inputs (time-correlated only), ambient air temperatures, and time.

2. Test Setup and Procedure

The Pioneer DSS antenna was chosen, since it is not thermally protected with a thermal coating material and is typical of the galvanized antennas of the DSN. The antenna was held at a fixed position, and the antenna was measured in the morning, afternoon, and at noon to achieve varied sun directions. Two measurements were made without sunlight: one before sunrise and one after sunset. Located uniformly over the dish were 84 triple-dot optical antenna targets, which were read by using a theodolite that was shaded and "bucked in" on the dish datum plane. The reading periods started at 5 a.m., 9 a.m., 12 noon, 4 p.m., and 8 p.m. and took from 20 to 40 min each. Wind, ambient air temperature, and time were recorded at the completion of the reading of each row of 24 targets, which meant that these measurements were repeated seven times during one complete measurement of the surface.

The field data were recorded on data sheets that were oriented for direct computer input. The data were keypunched and processed on the JPL RMS Best Fit computer program.

3. Results and Conclusions

The magnitudes of the thermally caused variations in rms surface distortion, boresight shift, and focal length change encountered in 57 surface measurements on 13 separate days are as follows:

Rms surface distortion. The maximum variation in the rms surface distortion caused by thermal deflection of the parabola was 0.006 in. This was for an ambient air temperature range of 50 to 96°F and a maximum solar energy input of 17 h. The lowest rms value occurred at 5 p.m. with an ambient air temperature of 87°F, and the highest value occurred at 2 p.m. with an ambient air temperature of 78°F. The minimum and maximum occurred on different test days.

Boresight shift. The maximum variation in the boresight shift of the parabola was 0.004 deg. The maximum and minimum occurred on the same test day, over the period of 1 to 5 p.m. with an ambient air temperature variation of only 2°F.

Focal length change. The maximum variation in the focal length change of the parabola was 0.280 in. The minimum focal length change occurred at 6 a.m. with an ambient air temperature of 50°F, and the maximum focal length change occurred at 9 a.m. with an ambient temperature of 80°F. The minimum and maximum occurred on different test days.

The only daily trend found after comparing the above three properties of the parabola versus time was a consistent change in the focal length from a negative, or shorter, length to a positive, or longer, length. This cycle occurred for every test day.

The variations in rms surface distortion and boresight shift with respect to either time or thermal inputs were so random and of such insignificant magnitude that no discernible trends were noted.

The above variations in rms surface distortion, boresight shift and focal length change, at S-band frequency will not impair antenna performance; however, it could be impaired by these same changes at X-band frequency.

C. New Technique for Setting Perforated Plate Panels, *F. W. Stoller and J. Carpenter*

1. Introduction

A new technique has been developed to measure and set the perforated type of antenna reflector surfaces. It has been applied in setting the old-type face panels at the Pioneer and Woomera DSSs, and will be employed in the forthcoming upgrading of the 85-ft HA/dec antenna at the Johannesburg DSS.

A general description of the measurement technique, its features, and its limitations follows.

2. Optical/Mechanical Configuration

a. Reflector mechanical axis primary datum plane. This plane is established by four optical tooling targets placed 90 deg apart and permanently attached to the upper chord members of the box girder at antenna erection (the declination [elevation on an az-el antenna] axis is set to gravity by using two optical mirrors and two Wild theodolites). This plane is 13.000 in. above the primary-reflector vertex. A normal line passing through this plane and to the vertex represents the mechanical axis of the dish. This plane controls the elevation of the theodolite above the dish vertex and is the primary reference for the installation and alignment of the following units of the antenna mechanical subsystem:

(1) Dish.

(2) Hyperbola.

(3) Cassegrain cone.

(4) Optical tracking aid (OTA).

(5) S-band acquisition aid (SAA) antenna.

(6) Optical acquisition aid (OAA).

(7) Spirit levels.

(8) Datex readouts.

(9) Secondary datum plane.

b. Permanent vertex fiducial. This fiducial, which consists of a permanent base plate attached to the antenna center hub at antenna erection, controls the vertex position of the theodolite. The theodolite mount assembly and the theodolite are removable from the structure, but are easily replaced at the original installed position by means of built-in close-tolerance interfaces. The theodolite mount swivel is the interface relative to the vertex for the face-panel contour drill gauges that are used to drill the face-panel target holes at installation. The swivel is also the interface for the tape used in conjunction with the clip-setting jig and the theodolite when setting the face-panel attach clips at installation.

c. Permanent secondary reference plane. This reference consists of four optical tooling targets permanently attached to the antenna structure at antenna installation. The targets are set to gravity when the reflector mechanical axis primary datum plane is set to gravity with all equipment, except for the cassegrain cone, installed on the antenna. Two of these targets are attached to the declination bearing housings, and two are attached to the declination wheel assembly. Two Wild theodolites are used to level these targets to gravity when the OTA, SAA, OAA, spirit levels, and Datex readouts are to be rechecked while the cassegrain cone is in place. When this reference plane is leveled to gravity, the antenna and the reflector mechanical axis are pointing to zenith.

d. Perforated plate face-panel targets. Each face-panel target is a triangular aluminum block with a graduated face in which each division is 0.125 in. (Fig. 1). The targets are held in place at one radius at a time on the face panel by hand or gravity; this eliminates the need for drilling 1300 holes for them in the dish surface.

If off-zenith position measurements are required, the targets can be secured in place by small bolts or screws. The grid scale is clearly visible at the rim of the dish when observed from the vertex theodolite during dish-measurement periods. Because of adverse thermal effects on the structure, dish measurements are made from 2 h after sunset until sunrise.

The zero or center of the scale is the nominal position of the face panel. These panel targets are designed such that rapid measurements can be made to an accuracy of 0.030 in. over a range from the nominal position of ± 1.500 in. when the theodolite line of sight is set at the required setting or measuring angle. It is not necessary to use an optical micrometer or to adjust the line of sight to the center target to compute the target displacement. This target design and measurement technique permits measurement of 1300 panel target positions to the closest

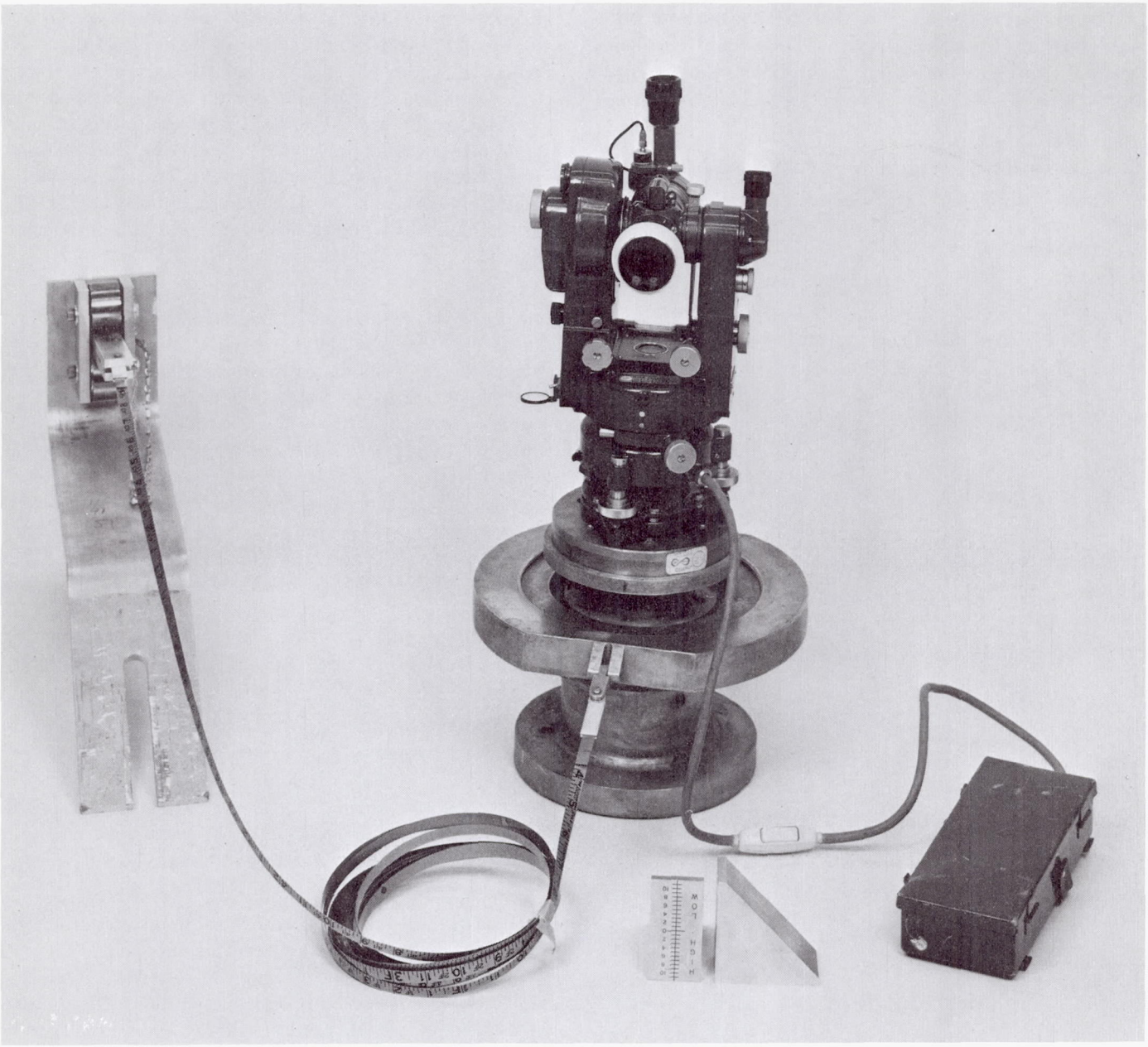

Fig. 1. Face panel contour measurement equipment

0.030 in. in approximately 5 h time. To determine target displacement with methods that use only a single-dot target, either an optical micrometer is required or the angular displacement of each panel target must be measured—both of which are very time-consuming, taking about five times as long.

e. Special instrumentation. In addition to the targets, this dish-measuring technique uses a special, high-precision theodolite and a chord distance measuring tape with built-in metal scribes for scribing dish panels at all target points and a negator spring assembly to hold the chord distance tape with a constant 50-lb pull. The theodolite has special bearings and a hollow azimuth bearing that enable the telescope to look through the theodolite azimuth axis and also allow the theodolite to be used in attitudes other than its normal position. Special calibration and data reduction will permit use of the theodolite for accurately measuring the dish surface at near-horizon attitudes of the antenna.

3. Procedure

a. Individual panel adjustment. The face-panel attach clips are installed at the correct location during installation of the antenna. This is accomplished by using a clip-setting fixture, the theodolite, and the dish mechanical axis primary datum plane. The correct position of the clips allows for a nominal 0.060-in. shim to be installed between the face panel attach plate and the clip. The clip assemblies are made from 0.25-in. structural tees and 0.25-in. angle iron. They are attached to the backup structure with high-strength bolts that minimize movements and deflections of the panels.

When the dish-surface targets are measured and the results recorded on the contour measurement field data sheet, this information is used to change the shim size as required—in 0.030-in. increments—at each panel attach point.

b. Plot plan of dish surface. The same type of data sheet used for the high-performance panels (SPS 37-47, Vol. II, p. 105) is used as a field data sheet to record the results of dish measurements. It shows the location of all panel targets, ribs, and theodolite setting angles, with information on how to record panel target measurements. Provision is made for permanently recording all pertinent field data at the time of observation and measurements.

c. General procedure for measuring the dish surface. The theodolite is mounted on the theodolite mount assembly and adjusted and oriented to the dish mechanical axis datum plane. The face-panel targets are placed at a given radius, and the theodolite is calibrated for elevation angle correction factors. The results are recorded on the field data sheet, and the required instrument elevation angles are computed. The theodolite is set to the required elevation angles and the first row of panel targets is observed; the results are recorded on the data sheet. Each time the telescope sweeps past a mechanical axis primary datum plane target, the telescope is directed to that target and the resulting angle recorded in the appropriate space on the data sheet. This procedure is followed until all face panel targets have been observed and recorded at all desired radii.

D. Venus DSS Activities, *E. B. Jackson, J. D. Campbell, R. M. Gosline, and A. L. Price*

1. Experimentation

During the period October 16 through December 15, 1968 the Venus station, utilizing the 85-ft az–el antenna, conducted monostatic (and with the Mars DSS) bistatic planetary radar experiments. Reception of pulsars continued at S-band (2.388 GHz) and reception was attempted at X-band (8.448 GHz). Reception was not immediately successful at X-band, and postprocessing of signals is continuing in an effort to establish a minimum upper bound on signal strengths which would have been detected.

Utilizing the Venus 85-ft antenna and 450-kW transmitter for transmitting and the Mars DSS 210-ft antenna for receiving, the planet Venus was again successfully ranged on October 25 at a nominal one-way range of 123×10^6 mi. Data indicate that the round-trip range to Venus was 140×10^{-6} s less than predicted.

Utilizing a special antenna (crossed yagi) and dual-channel phase-lock receiver, Faraday rotation phase data are being collected, utilizing the ATS-1 satellite, which is in synchronous orbit approximately over Hawaii, as a source of polarized transmissions at 137 MHz. The phase data are punched onto paper tape every minute, converted to punched cards, and forwarded for reduction and analysis.

The 30-ft az–el antenna continued to be used for clock synchronization transmissions to Tidbinbilla, Australia, although transmissions are now being made at increased power (25 kW) to provide system testing and improved signal-to-noise ratio at the receiver.

By using the special R&D receiver and noncoherent signal detection equipment at the Mars DSS, daily spectrograms were taken of the signals from the *Pioneer VI* spacecraft as it approached the sun, was occulted, and then emerged during November. These spectrograms will yield information about the sun's corona through which the signals have passed.

2. System Performance

a. Digital systems. Tape reader problems which were experienced with the station control and monitor subsystem (SCAM) have been eliminated by reverting to the original slower reading speed of 100 characters/s. The Rheem RR-100R tape readers had been modified to read 300 characters/s but will not operate reliably in the start–stop mode required by the SCAM.

b. X-Band transmitter. Operation of the X-band transmitter at higher power level (20 kW) continues. Testing at 25 kW power level is also taking place. Some waveguide and waveguide switch heating has been noted, and

corrective action is being taken to provide additional cooling and reduce switch insertion loss.

The only failure during this period was that of the waveguide horn diaphragm. During a test at 25 kW output a hole was burned through the diaphragm. The diaphragm was replaced, and subsequent tests at 25 kW have caused no problems.

3. System Improvements

a. Antenna system

85-ft antenna. A program to provide real-time direct computer control of the 85-ft az–el antenna, using the SDS 930 computer as the control element, has been started. The computer, by direction of typewritten input command, will perform static and dynamic tests and then will command the antenna to point at a target and begin tracking. Electrical and hydraulic parameters will be continuously monitored by the computer, and in the event of an anomaly, a descriptive message will be typed out on the typewriter.

The servo amplifier and power supplies have been modified to allow external control and monitoring. An interface unit was constructed to "condition" signals from the servo to make them compatible with the computer. The unit will also house control relays and indicator lamps. A computer program has been written and, along with the hardware, will be tested during the last 2 wk of January 1969.

30-ft antenna. The servo electronics were replaced with a solid-state system of the type used on the 85-ft az–el antenna at the Venus DSS and the 210-ft az–el at the Mars DSS. In reliability and stability, this system has proven to be superior to the vacuum tube unit, resulting in less maintenance time and a simplified premission checkout procedure. Another beneficial result was the elimination of one equipment rack by consolidating the servo amplifier, power supplies, and the boresite television monitor and controls into one enclosure.

b. Digital systems. The clock synchronization program normally used with the X-band system has been modified to allow the clock sync programmed oscillator to be used with S-band planetary radar experiments. The doppler correction can thus be generated directly in real-time from polynomial coefficients, eliminating the intermediate step of generating a doppler drive tape.

A series of diagnostic routines have been written to assist with premission checkout of the SCAM.

Several of the older special tape programmed control and data processing devices at the Venus DSS were built using a line of logic modules developed by Computer Control Co. These logic modules, although obsolete by present-day standards, are used in large quantities at the Venus DSS. In an attempt to increase the reliability of devices utilizing these modules, a logic tester has been constructed for the LE-10 and SM-10 modules. The tester was designed to fit into an existing environmental test chamber and can test modules at various temperatures with deliberately noisy signals structured to provide worst-case operation. A summary of the test data from the initial batch indicates that the LE-10 modules operate more reliably in a relatively warm (85°F) environment. The modules were tested at 50, 85, and 125°F. Outside this range their performance falls off rapidly. The total failures listed in Table 1 exceed 100% because some modules failed at more than one range.

Table 1. Performance of LE-10 modules under noisy signal conditions

No failures	59%
Failed at 50°F	24%
Failed at 85°F	10%
Failed at 125°F	21%

c. X-band transmitter. To reduce waveguide and waveguide switch overheating problems, all the waveguide switches were removed from the 30-ft antenna and returned to the Laboratory where they were modified to reduce insertion loss and tested. Following reinstallation on the antenna, further temperature measurements were made to evaluate the efficacy of the modification. At approximately the same ambient temperature and power level (25 kW) as before, the rotors of the modified switches operate at only 72% of the previous temperature, stabilizing at 155°F.

The old exciter equipment has been modified, repackaged, and installed in the new control cabinet. All the exciter control and monitor functions are now performed automatically upon application of the control power supply voltage.

To prevent heat exchanger damage from coolant water freezing during cold weather, the heat exchanger was modified to permit automatic water heater (15 kW) and water pump operation when the air temperature and

water temperature drop below prechosen points. The modification also prevents the heat exchanger fans from operating at low temperatures.

E. Klystron Characteristics at Reduced Output Levels, *R. C. Chernoff*

1. Introduction

High-power microwave amplifiers are normally designed for operation at or near the rated power output level. The reasons for doing so are that efficiency and bandwidth are both maximized at maximum output. Furthermore, saturation is a positive advantage for an amplifier of phase-modulated signals, since it provides "limiting," i.e., it helps to remove residual AM from the input signal. For these reasons, the present DSIF S-band power amplifiers were specified, designed, and tested for operation at rated output. However, in order to comply with the various spacecraft tracking instructions, DSIF transmitters are required to produce a wide range of up-link power levels. In some cases[1], a range of 27 dB (10 to 0.02 kW) may be called for in the course of a mission. It has therefore become necessary to supplement existing klystron performance data, which consist largely of data for operation at rated output, with data covering a wide dynamic range.

2. Operation at Low Output Levels

The output of a klystron can be controlled by varying either its RF input or beam voltage. At full-rated output power, the klystron is, of course, saturated. When reduced up-link power levels are called for, the presently recommended practice[2] is to reduce the output power by reducing beam voltage and to raise drive power until the klystron is saturated again. On the other hand, field experience and recent measurements (SPS 37-46, Vol. III, pp. 95–101) indicate that, as beam voltage is decreased, the drive required to saturate the klystron over its entire bandwidth increases so rapidly that it soon exceeds the available drive, with the result that the klystron must operate far below saturation over all but the upper 5 or 6 dB of its dynamic range. Since unsaturated operation is unavoidable at low output levels, the assumed advantages of the present method of controlling output by varying beam voltage are called into question.

[1]*Lunar-Orbiter Tracking Instructions Manual (DSIF)*, Fig. 2-10, March 1, 1968 (JPL internal document).

[2]*Technical Manual, Operation and Maintenance, Transmitter Subsystem*, Part I, Para. 3-14, April 1, 1968 (JPL internal document).

The tests described herein are an attempt to compare the advantages and disadvantages of the present method with the simpler method of controlling output power by varying drive power alone with beam voltage left at the level required for rated output. The parameters selected for measurement in these tests are: bandwidth, phase jitter (incidental PM), and incidental AM. A standard DSIF 10-kW transmitter subsystem was used for the tests. The klystron tested is an Eimac model 4KM50SI, a four-cavity tunable klystron which is broad-band tuned to cover the 2110- to 2118-MHz DSN band at rated (10-kW) power. The beam voltage at rated power output is 17.0 to 18.0 kV. The klystron was not retuned during the tests.

3. Testing

a. Bandwidth. Bandwidth was measured over a 17-dB range (10 to 0.2 kW) of output power for each of two modes of output power control:

Mode 1. Output controlled by a combination of beam voltage and drive variation such that the drive level was either the saturation drive at band center or the maximum available drive, whichever was smaller.

Mode 2. Output controlled by drive only; beam voltage held constant at value (17.0 kV) required for rated output.

The bandwidth was measured by sweeping the drive frequency from 2106.4 to 2128.4 MHz. The drive power variation during the sweep was less than 0.3 dB peak-to-peak. Figures 2 and 3 are the data for Mode 1 and Mode 2 operation, respectively.

Figures 2 and 3 indicate that Mode 1 ("saturation") operation gives slightly better bandwidth for the upper 10 to 12 dB of the output range, but that Mode 2 (constant beam voltage, unsaturated) operation is superior below 400 W. They also show that the klystron bandwidth does not cover the entire 2110- to 2118-MHz DSN band below 1.8 kW in either mode. This means that up-link channels close to 2110 or 2118 MHz may be on the skirts of the klystron bandpass at low power levels. Some modulation distortion would occur in such cases.

b. Phase jitter. The phase jitter added by the klystron was measured by the test setup shown in Fig. 4. The setup is essentially a phase modulation (PM) receiver with the scope to view the detected signal. Beam voltage ripple measurements were made in conjunction with these measurements. The phase jitter measurements were made

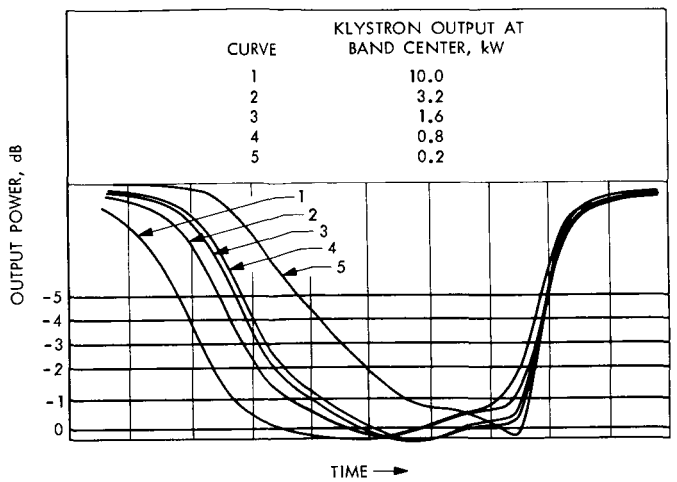

Fig. 2. Klystron bandwidth, Mode 1 operation

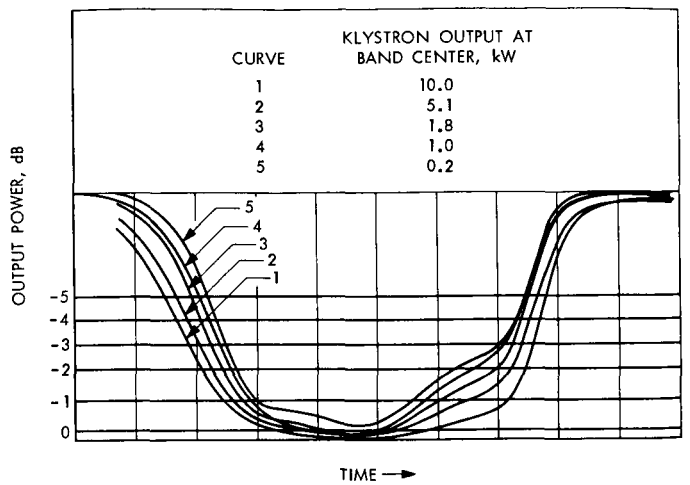

Fig. 3. Klystron bandwidth, Mode 2 operation

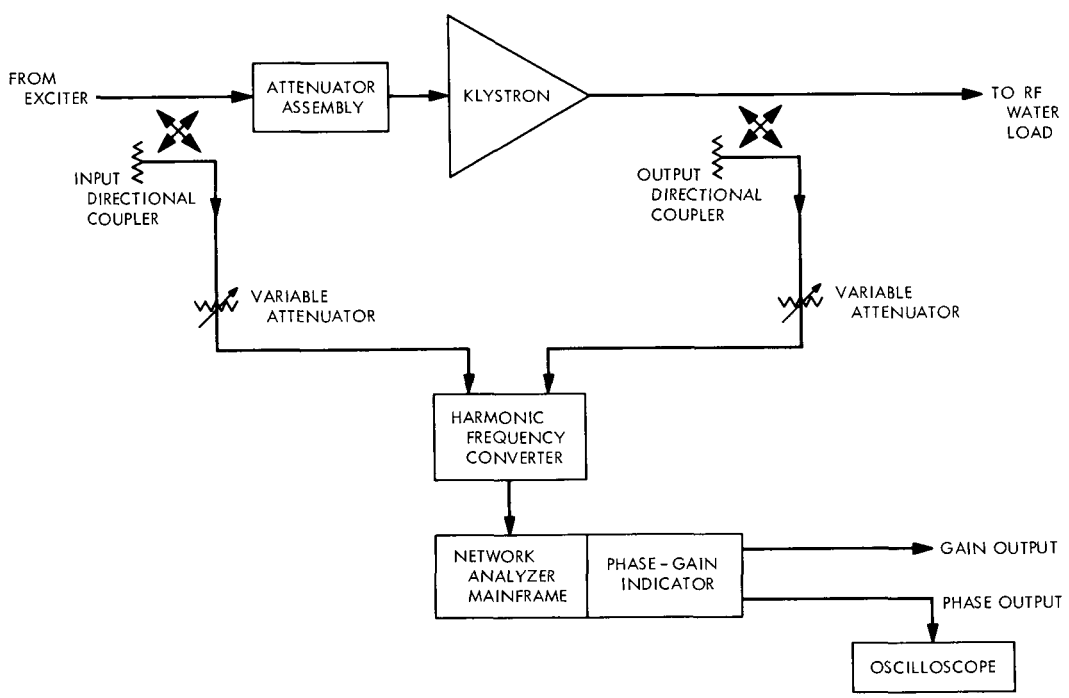

Fig. 4. Test set-up for klystron PM and AM measurements

over a 17-dB output range for both Mode 1 and Mode 2 operation. The results are as follows:

(1) PM frequency was 400 Hz. No other frequency component was apparent.

(2) PM amplitude varied between 1.0 and 2.0 deg peak-to-peak.

(3) No clear correlation was noted between PM and operating mode (Mode 1 or Mode 2).

Figure 5 is a typical oscilloscope picture of PM. The amplitude of the 400-Hz component of the PM was in rough agreement with the amplitude, 16 V peak to peak, of the 400-Hz component of the beam voltage, and the calculated phase pushing factor (0.055 deg/V) of the klystron at 17.0 kV. However, while the beam voltage ripple was predominantly 20 Hz with a somewhat smaller 400-Hz component, no 20-Hz component was visible in the PM. The 20-Hz component of beam voltage ripple is due to a 20-Hz modulation of the field excitation of the 400-Hz

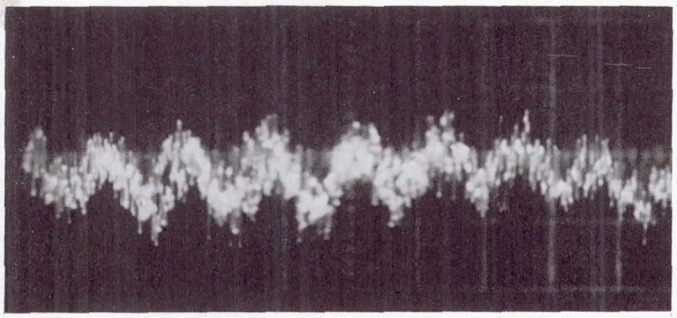

Fig. 5. PM caused by 400-Hz beam voltage ripple

synchronous alternator used as primary power source for the beam power supply. The apparent absence of the 20-Hz component in the PM is due to instrumentation problems which could not be tracked down in the time available. A more extended series of tests is planned in order to resolve this and other inconsistencies in the data presented here. The phase noise superimposed on the 400-Hz PM in Fig. 5 is mostly receiver noise. The test instrumentation used is not suitable for measuring the wide-band phase jitter generated by the klystron beam.

The phase pushing factor of the klystron was measured directly by observing the phase shift caused by successive 1.0-kV increments in beam voltage. The measured phase shift caused by changing the beam voltage from 17.1 to 16.1 kV was 59 deg. The calculated phase shift for this voltage change is 57 deg.

c. Amplitude modulation. Beam voltage ripple induces AM as well as PM in the RF output. The AM due to the klystron was measured with the same (Fig. 4) test setup used to measure PM but with the scope connected to the amplitude jack of the phase-gain indicator. The scope signal represents differential gain in this case. It was found that the AM frequency, like the PM frequency, was 400 Hz with no other visible frequency component. However, it was found that operating mode had a large effect on AM amplitude. For example, with beam voltage at 9.9 kV and with maximum available drive (Mode 1 operation), the AM amplitude was approximately 0.4 dB peak-to-peak. With beam voltage at 17.0 kV but with drive reduced to yield the same output (1.1 kW) as in the previous case (Mode 2 operation), the AM amplitude was less than 0.1 dB peak-to-peak. When saturated at 17.0 kV (10 kW output), AM was below noise level. If we assume that beam voltage ripple is the sole cause of the 400-Hz AM, and if we also assume that RF output is, to first order, proportional to $V^{5/2}$ (where V = beam voltage) the observed levels of AM appear to be too high. For example, the 0.4-dB peak-to-peak AM observed at 9.9 kV would, if due solely to beam voltage ripple, correspond to about 3.6% peak-to-peak ripple. Further tests will be made in an attempt to establish frequency and amplitude correlation between AM and beam-voltage ripple at various beam-voltage levels.

4. Conclusions

The tests of bandwidth, PM, and AM described above show that Mode 2 (constant beam voltage, variable drive) is superior to Mode 1 (variable voltage) operation in some respects. Marked differences in performances between the two modes of operation occur only below 1.0 kW (10 dB below rated output power), and the superiority of Mode 2 over Mode 1 operation at low output levels consists of better bandwidth and lower incidental AM. It must, however, be emphasized that the tests are not entirely conclusive, because they provide no data on AM limiting by the klystron as a function of drive and beam voltage. Since limiting is an important advantage of saturated operation, and since the klystron is, on the average, more saturated for Mode 1 than for Mode 2 operation, the necessity and importance of limiting will have to be evaluated in order to decide which mode to recommend.

Further tests will be made in order to resolve these inconsistencies in PM and AM measurements. As soon as this is done, new instructions for low power operation of the transmitter will be prepared.

F. X-Band Time Synchronization Transmitter,

R. E. Arnold

1. Introduction

During this reporting period, the X-band time synchronization transmitter has been operating with an RF output of 20 to 25 kW at 8.4501 GHz. This report describes the operating characteristics of the high-voltage power supply and the antenna-mounted transmitter.

2. Power Supply Description

Figure 6 is a simplified line diagram of the transmitter power supply and klystron. Major system components consist of the following:

(1) 60- to 400-Hz 500-kW motor–generator (MG) set with motor-starting controls and programmable silicon-controlled rectifier (SCR) dc field power supplies.

(2) High-voltage 400-Hz step-up transformer.

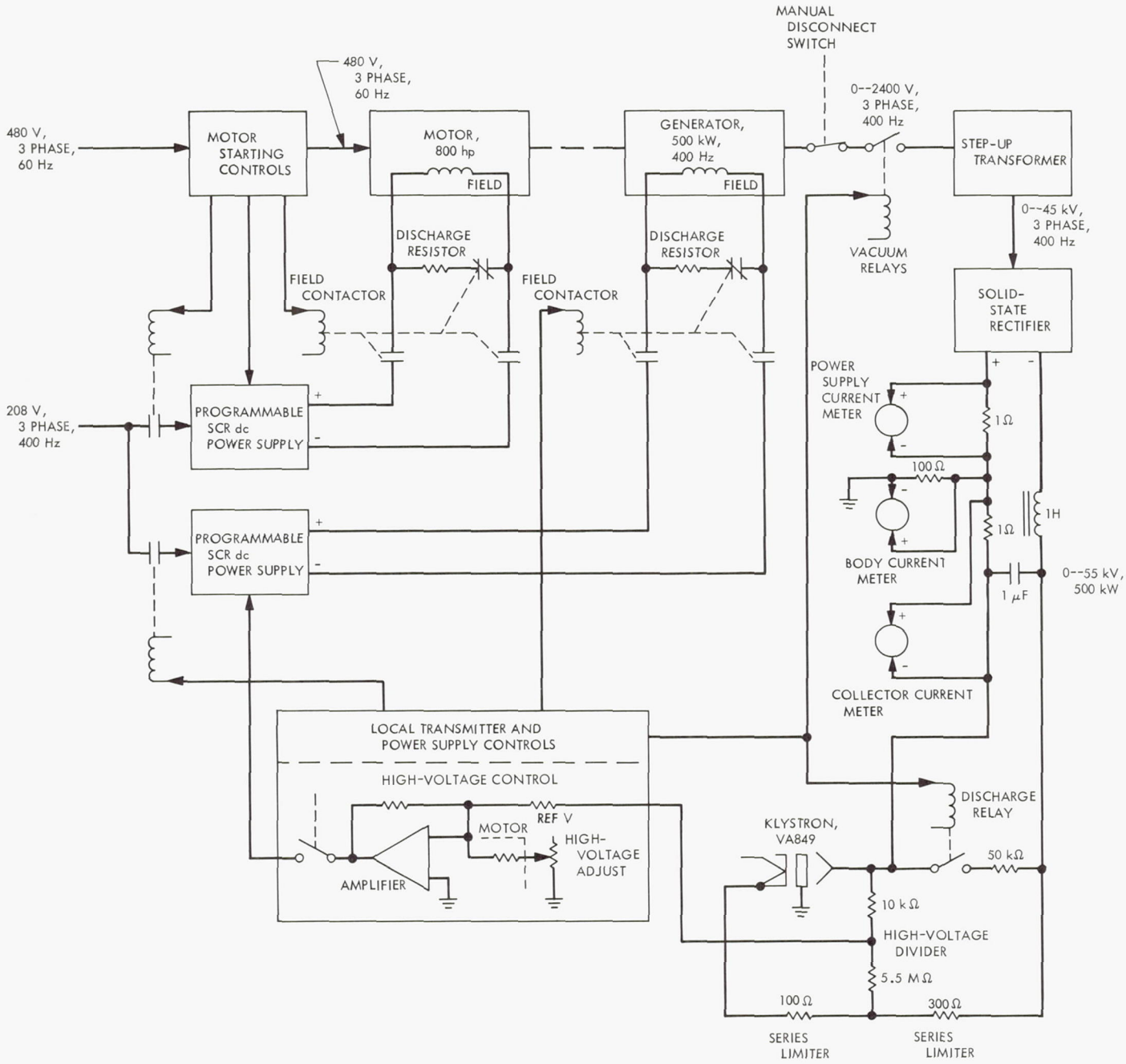

Fig. 6. Block diagram of the transmitter power supply and klystron

(3) Solid-state three-phase full-wave bridge rectifier.

(4) Choke-capacitor ripple filter.

(5) High-voltage divider.

(6) 300- and 100-Ω series limiter.

(7) VA 849 transmitter klystron.

(8) Transmitter power supply controls.

Items 1 and 8 are new equipment, especially designed and built for the system. Items 2 through 5 were salvaged from the Venus 85-ft antenna transmitter after higher voltage units were installed in that system. Items 6 and 7 were used on the former 10-kW X-band transmitter system.

Table 2 gives the power supply operating characteristics, using the transmitter as a load. Although the dc output power is 72 kW, an additional approximate 20 kW is lost in the step-up transformer and rectifier.

Table 2. Power supply operating characteristics

Rectified dc output	
Voltage	25.3 kV
Current	2.85 A
Power	72 kW
Motor (800 hp, 60 Hz)	
Line voltage	480 V
Line current	139 A
Exciter field voltage	87 V
Exciter field current	24.5 A
Generator (500 kW, 400 Hz)	
Line voltage	1.6 kV
Line current	32 A
Exciter field voltage	33 V
Exciter field current	51 A

3. 500-kW MG Set Starting Transients

As previously reported in SPS 37-54, Vol. II, pp. 67–69, the MG set did not meet JPL's requirement of a maximum 500 kV-A during starting of the 800 hp motor. The motor-starting sequence was modified, and the starting transients were reduced from 700 kV-A to below the specification of 500 kV-A. The modified starting procedure has now been fully automated into the control circuitry. Figure 7 is a strip-chart recording of the line current for the modified start used during the 162-s starting cycle. The maximum line current shown is 450 A (375 kV-A) at 155 s. Because of the relatively slow response time of the strip-chart recording, the current waveform does not show the larger in-rush currents shown on the oscilloscope photo in Fig. 10 of SPS 37-54, Vol. II, p. 69.

4. VA 849 Klystron Transmitter

The antenna-mounted transmitter uses a VA 849G klystron, rated for 25 kW RF output at 8.4501 GHz. Prior to the power supply upgrade, the transmitter had operated at 10-kW output power. The system still uses the two original VA 849G klystrons that were procured in 1962; VA 849G SN 28 is installed in the transmitter, and VA 849 SN 26 is a spare. Table 3 gives the operating characteristics of SN 26.

The klystron has survived numerous waveguide arcs and internal arcs during the transition from low to higher power. Operation is now stable at the 25-kW power level, and the arcing has ceased to be a problem.

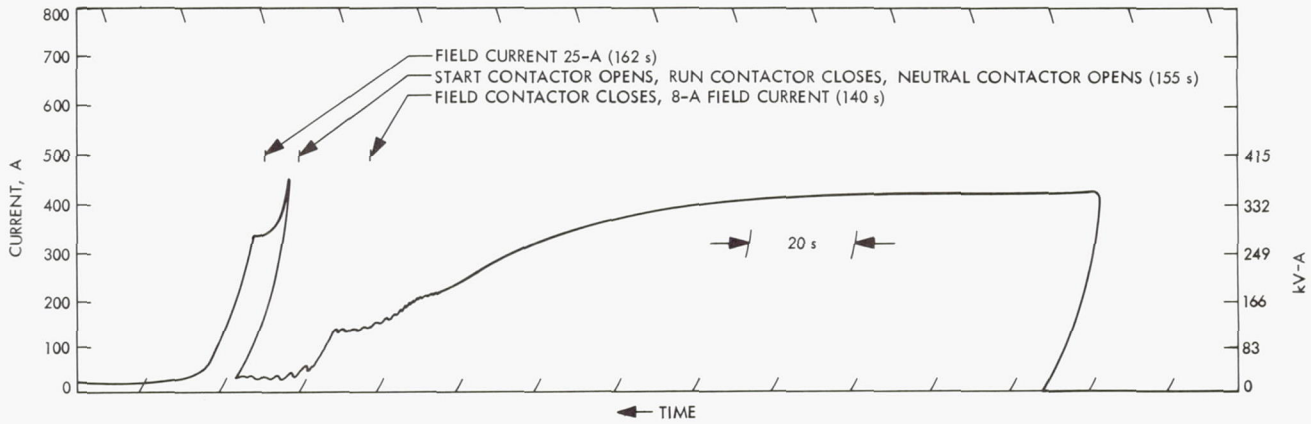

Fig. 7. 800-hp motor-starting current (modified start)

Table 3. Operating characteristics of VA 849G klystron SN 26

Output power (efficiency tuned)	25 kW
Reflected power (antenna)	115 W
Reflected power (water load)	350 W
Drive power	1 W
Beam voltage	25 kV
Collector current	2.85 A
Body current	28 mA
Focus magnet current	6 A
Collector coolant flow[a]	11.2 gal/min
Body coolant flow[a]	1.4 gal/min
Magnet coolant flow[a]	0.9 gal/min
RF water load coolant flow[a]	4.5 gal/min

[a]Coolant is a 25% uninhibited ethylene glycol and 75% water solution.

The klystron operating characteristics still match the manufacturer's data.

5. Beam Voltage Decay

In a high-power transmitter power supply, it is desirable to reduce the beam power supply energy as quickly as possible after detection of a fault (e.g., klystron beam or body overcurrent in case of a klystron internal arc). Figure 8 is an oscilloscope recording of the beam voltage upon simulation of a beam voltage OFF signal; the power supply load was a VA 849 klystron under normal operating conditions, and an actual fault did not occur. The small spikes on the voltage decay waveform are relay-switching transients picked up by the long leads from the output of the high-voltage divider. After the initial beam OFF signals, the following events occurred (Figs. 6 and 8):

(1) The program input to the generator field SCR dc power supply is turned off.

(2) The generator field contactor (FC) is deenergized. The field discharge resistor is connected across the field.

(3) The series contacts of FC open and disconnect the field programmable SCR dc power supply from the generator field.

(4) The vacuum relays in series with the generator output and step-up transformer are deenergized and opened.

Total time for the beam voltage to decay to 10% of its original value is 150 ms.

6. Klystron Internal Arc Power

In a klystron operating with a space-charge limited beam, the total dc power dissipated in a time interval is

$$P\,(\text{W-s}) = V \cdot I \cdot T = K\int_0^T V^{5/2} \cdot T \cdot dT$$

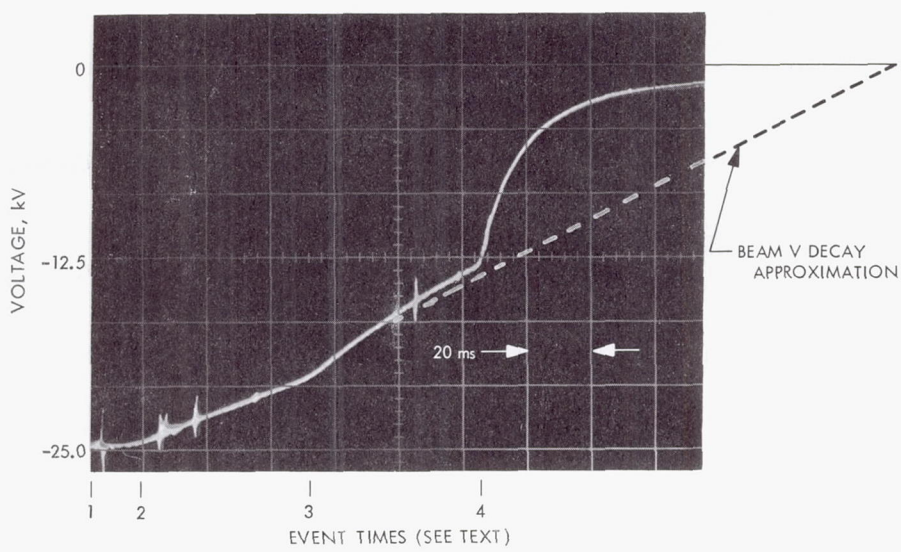

Fig. 8. Beam-voltage decay

where

V = dc beam voltage, V

I = current, A

T = time, s

K = prevalence of the klystron
= 0.72×10^{-6} for the VA 849G

If the beam voltage decay curve is approximated by the straight line function $V = 25{,}000\,(T/0.25)$, where $T = 0.25$ s, the power dissipated becomes

$$P\,(\text{W-s}) = K \int_0^{0.25} \left(\frac{25 \times 10^3}{0.25} T \right)^{5/2} T\,dt$$
$$= 3550\ \text{W-s}$$

In the case of a klystron internal arc the energy is actually dissipated in both the klystron and in the 400-Ω series limiting resistor (Fig. 6). Assuming a klystron arc has an impedance of 1 Ω, the power in the arc is

$$P_{(\text{klystron arc})} = 3550\ \text{W-s} \times \frac{1\,\Omega}{401\,\Omega} = 8.9\ \text{W-s}$$

In an effort to still further reduce the klystron arc energy and increase transmitter system reliability, a mercury-pool ignitron crowbar (SPS 37-41, Vol. III, pp. 102–103) is being built at JPL and is scheduled for installation during the latter part of FY 1969.

G. Wide-Band Doubler and Sine Wave Quadrature Generator, *R. B. Crow*

A wide-band doubler and sine wave quadrature generator has been developed for use on the multiple-mission command system. The circuit is a unique first-order phase-locked loop that produces both $\sin(\omega t)$ and $\cos(\omega t)$. The loop phase detector multiplies the two functions together and uses the difference frequency as the error signal to keep the two signals phase-locked, while the multiplier sum frequency fortuitously yields the second harmonic of the input frequency. Thus, for the particular multi-mission command function, the fundamental frequency (0.1 to 100 kHz) is used as a data subcarrier, while the second harmonic is used in the synchronizing signal. This unit is completely automatic and has possible application as both a wide-band doubler and sine wave quadrature generator. This particular solution to the doubling application yields the proper input/output phase relationship not achieved with other approaches considered.

Figure 9 illustrates that the phase relationship between the input and output is achieved by having two series R-C phase shifters controlled so that the output is phase-locked 90 deg from the input signal, i.e., the output is $\cos(\omega t)$ for $\sin(\omega t)$ input. This is accomplished by using a photoresistor as the variable resistor in the R-C circuit. An error voltage is generated at the output of a digital multiplier that is integrated (using an operational amplifier in the integrator configuration) and applied to a light source that controls the resistance of the photoresistor.

An analysis of the loop is performed as follows (Fig. 9): The control voltage v is seen to be

$$v = -\int K_D K_I \phi\,dt$$

where

$$\phi = \frac{\pi}{2} - \psi$$
$$= \frac{\pi}{2} - 2\cot^{-1}\left[\omega_0 CR(v)\right]$$

and the virtual integration justified with open-loop DC gain much greater than unity.

If the Taylor series expansion of $\cot^{-1} X$ is made about $X_0 = \omega CR(v_0)$, we find

$$\cot^{-1} X = \cot^{-1} X_0 - \frac{1}{1 + X_0^2}(X - X_0) + \cdots$$

Since it is desired that each of the two phase shifters have a phase angle of 45 deg in the locked condition, we take $X_0 = 1$ so

$$\phi = \frac{\pi}{2} - 2\left[\frac{\pi}{2} - \frac{1}{2}(X - 1)\right]$$
$$= X - 1$$
$$= \omega CR(v) - 1$$
$$= \omega C\left(R(v) - R(v_0)\right)$$

and

$$v = -\int K_D K_I \omega C\left(R(v) - R(v_0)\right) dt$$

If $R(v)$ is now expanded in a Taylor series

$$R(v) = R(v_0) + R'(v_0)(v - v_0) + \cdots$$

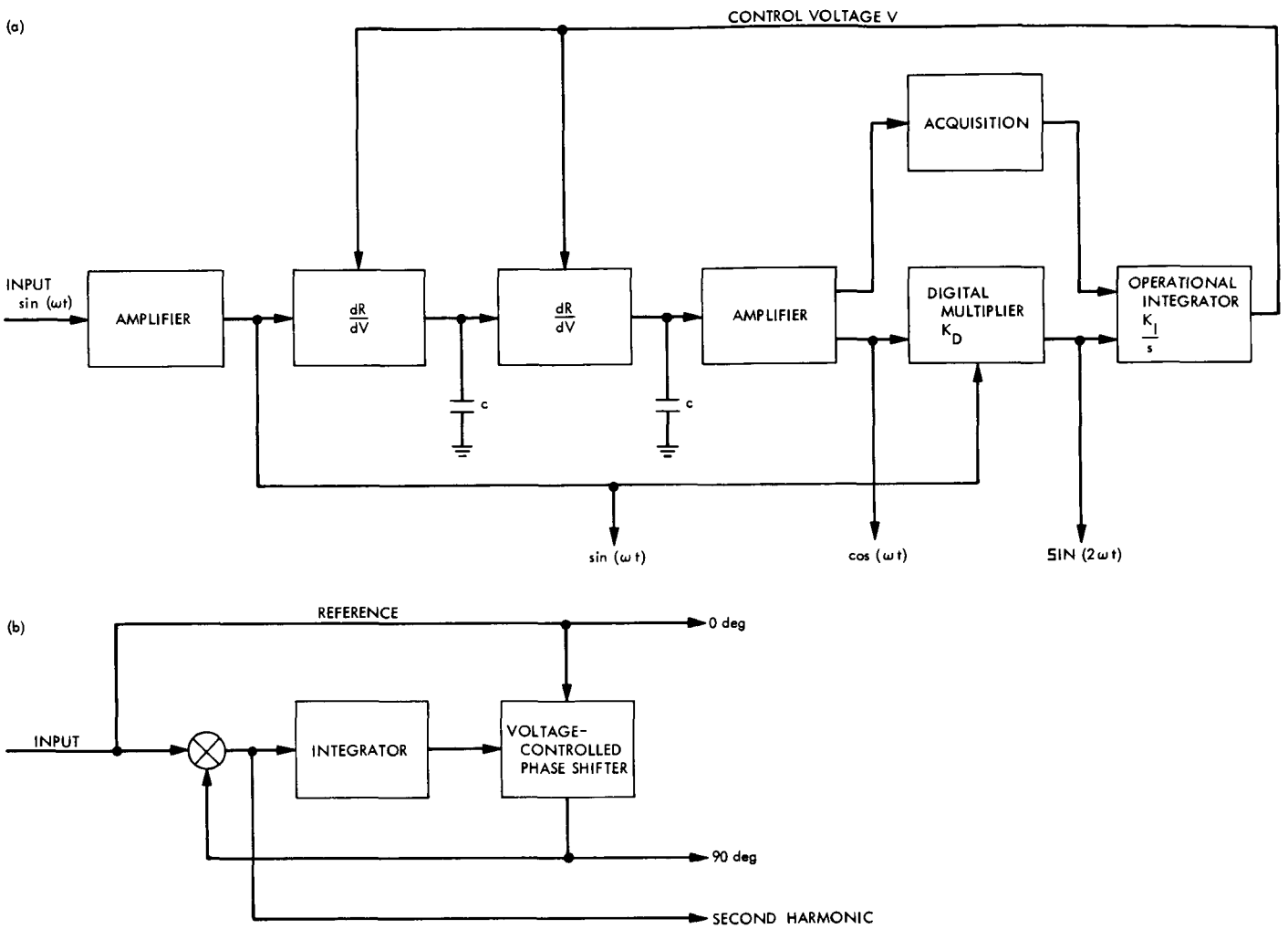

Fig. 9. Wide-band doubler and quadrature generator (a) block diagram, (b) phase-locked loop configuration

it follows that

$$v = -\int_{-\infty}^{t} K_D K_I \omega C R'(v_0)(v - v_0)\, dt$$

By differentiating both sides above and taking the Laplace transform, we find

$$V(s) = \frac{v_0 (K_D K_I \omega C R'(v_0))}{s(s + K_D K_I \omega C R'(v_0))}$$

$$= \frac{v_0 K}{s(s + K)}$$

or

$$v(t) = v_0 [1 - e^{-Kt}]$$

and, thereby, we also find

$$\phi = -\frac{R'(v_0)}{R(v_0)} e^{-Kt}$$

Thus it is seen that the steady-state phase error between the $\sin(\omega t)$ input and $\cos(\omega t)$ output will be zero, providing $(dR)/(dv)$ of the photoresistor is not zero at the operating point. This condition (viz., $(dR)/(dv) \neq 0$) holds for the particular device used for input frequencies of from 0.1 to 100 kHz. Further, the loop response is one of the first order and is always stable. Figure 10 illustrates the measured response of the first unit.

To confirm the model detailed above, the loop time constant was calculated ($\tau = 1/K$) and then measured experimentally. The measurement was made by driving

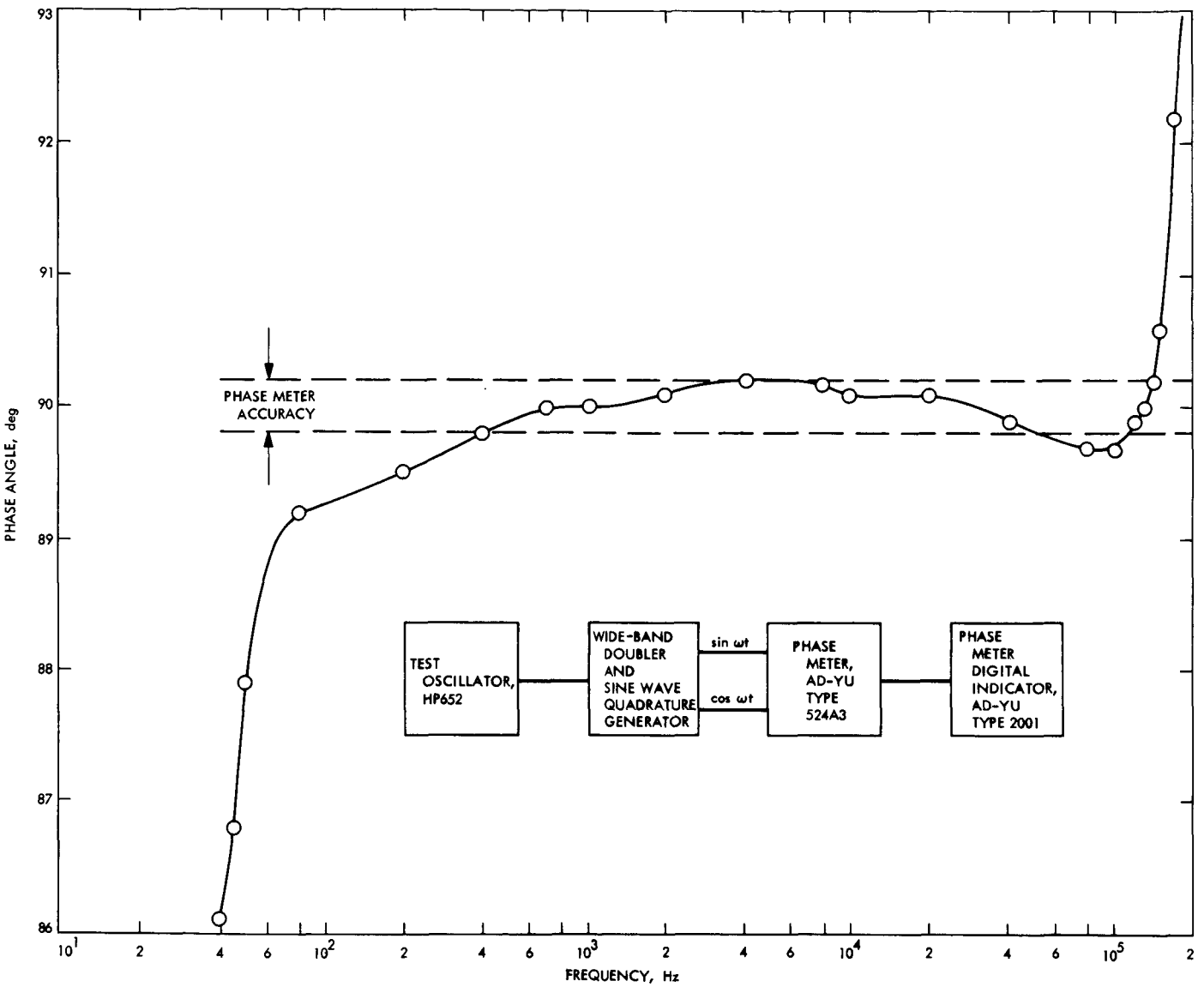

Fig. 10. Phase relationship between the two sine wave outputs

the input to the integrator when the loop was locked, and then measuring the frequency response. Figure 11 illustrates the frequency response test setup.

Since the loop response to an external input $y(t)$ is

$$V(s) = \frac{Kv_0}{s(s+K)} - \frac{K_I \omega CR'(v)\,Y(s)}{(s+K)}$$

i.e., a transient term and a steady-state term (caused by the driving function $Y(s)$), it is seen that the frequency response to a sine-wave input will be down 3 dB when the frequency equals K.

The results shown in Fig. 11 confirm the model, considering the accuracy with which $(dR)/(dv)$ was known from the manufacturer's published data.

The open-loop frequency response is obtained by breaking the loop at the output of the multiplier:

$$V(s) = \frac{K_I}{s} Y(s)$$

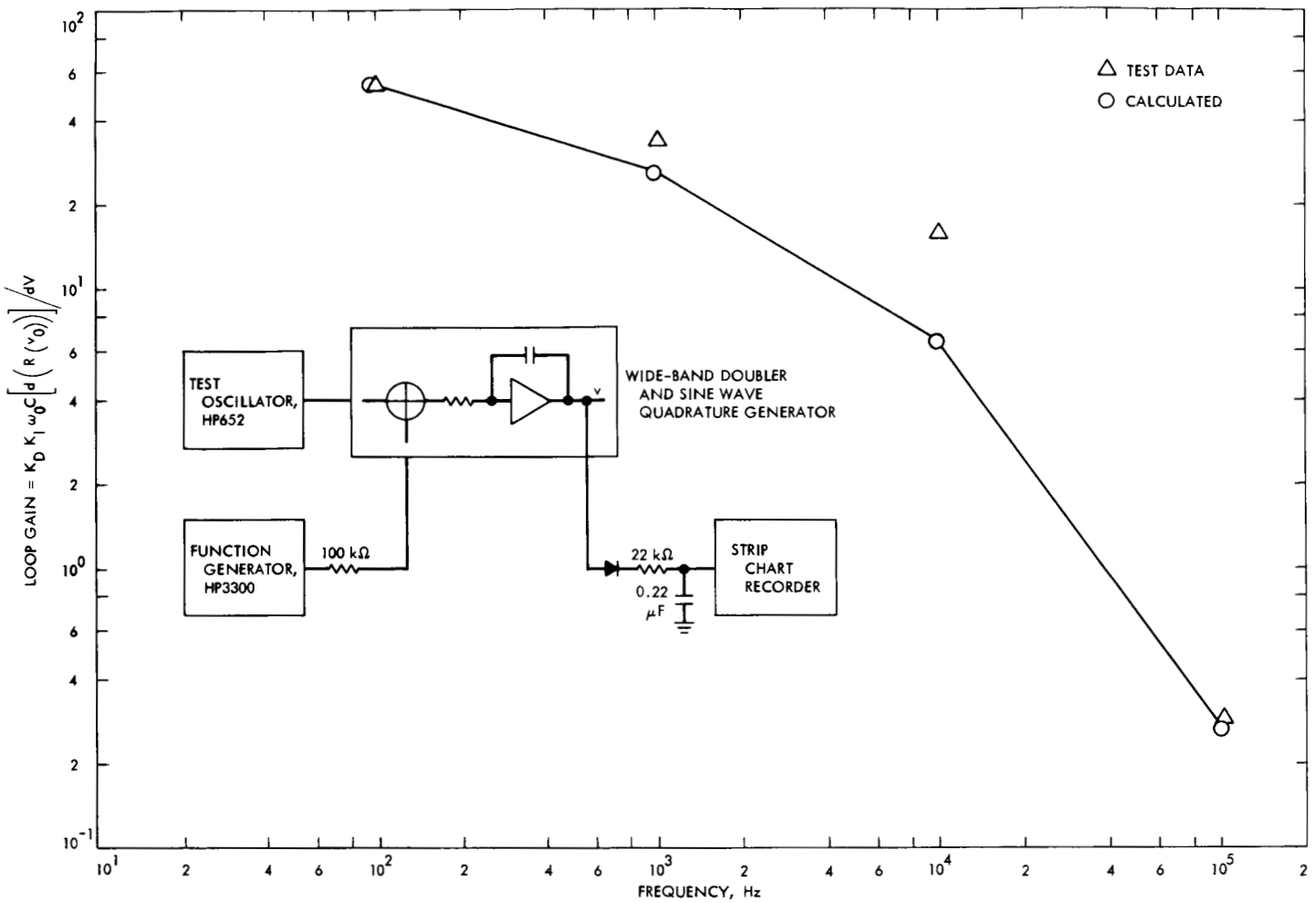

Fig. 11. Calculated versus measured loop gain versus frequency

and therefore the relation

$$\Phi(s) = K_D \omega C R'(v_0)\left(V(s) - \frac{v_0}{s}\right)$$

$$= K_2 (V(s) - v_0)$$

results in the response

$$\phi(s) = \frac{KY(s) - K_2 v_0}{s}$$

One unusual problem was encountered in building the first model. The desired control voltage ranged from −2 to −10 Vdc to control the lamp properly which, in turn, causes the photoresistor to change its resistance. In checking the prototype it was found, however, that decade step changes in frequency could shock the integrator so that the control voltage v momentarily became positive. When this occurred the loop no longer had control (the lamp being equally sensitive to either polarity control), and the integrator would continue integrating because of the reversal of K until the operational integrator saturated. This problem was solved by designing an acquisition circuit that sensed when the loop no longer had control (i.e., when the light was off and the cos (ωt) signal disappeared) and then applying a discrete command to make the control voltage v the approximate correct negative voltage so that the loop was again active and could lock onto the input signal.

In summary, this wide-band quadrature generator will have an output that is 90 deg displaced from the input (and a square wave second harmonic of the input) over a frequency range of 0.1 to 100 kHz. Operation is automatic and independent of frequency (over the specified limit) and operator control.

H. Division 33 Hi-Rel Module Development: A Line Driver for the DSIF Standard Logic Module Family, *D. W. Slaughter*

1. Introduction

The DSIF maintains a family of standard digital logic modules for the construction of special-purpose logic subsystems (SPS 37-46, Vol. III, p. 159). This report describes a line driver circuit which is being proposed as a member of this family.

Line driver circuits are required to interface between logic subsystems assembled from these logic modules (flip-flops, nand gates, clock generators) and the circuits of other equipments or subsystems, such as computers and radio-frequency subsystems. Large systems of digital logic also have internal interfacing requirements.

2. Design and Performance

The design goal is to minimize the number of line driver types which would have to be stocked in order to cover the spectrum of applications, and also to provide a flexible capability which would minimize the need for constructing special-purpose circuits for use in future systems which cannot be defined at this time.

The following requirements were considered:

(1) Bipolar output.

(2) Independent selection of the positive and negative logic output voltage levels.

(3) Signal swing large enough to drive all known or reasonable devices.

(4) Clean signals for driving analog devices.

(5) Ability to drive long signal lines, 100 ft or more.

(6) Transformer coupling, if required.

In addition, the line driver should be compatible with the other logic modules in terms of input logic levels, propagation delay, and rise and fall time of the output waveform.

Figure 12 is a schematic diagram of the proposed line driver. A logic zero input (nominally 0 V) produces a negative output current from a current source mechanized by the lower portion of the circuit; a logic one input (nominally +12 V) produces a positive output current from the upper portion of the circuit. Transistor Q1 (adjacent to the input) performs the selection of the proper current source.

The current-mode arrangement was chosen because of its capability for driving a variety of signal line types (coaxial cable, shielded wire, twisted pair and open lines) with a minimum of ringing at the terminal end, while maintaining circuit simplicity. Driving a constant current down the signal line prevents any ground potential (ringing-type noise) between the driver and the load from coupling into the signal (i.e., modulate the driving source) to the extent that the ground potential does not exceed the supply potential behind the current source.

The logic voltage at the user is generated by the flow of line current though the line terminating resistance. The resistance in the emitter circuits of the output transistors determines the positive and negative output currents. The selection of currents to be provided as a user option is under investigation. The means for selecting the values of resistors R13 and R14 is the primary concern. When resistors R13 and R14 are 0 Ω, the output currents are plus and minus 100 mA. This produces ±5 V across 50 Ω. The maximum voltage is ±10 V across 100 Ω, a limit set by the power supply voltages of ±12 V. Slightly higher supply voltages can be used for special purpose applications. For nonlinear loads, the logic voltage levels at the user may be set with the aid of diode clamps. Particularly useful is a diode clamp to ground. During the logic zero state, the diode will also serve in effect to sink current from the user in any amount up to the line drive current capability.

Figure 13 displays typical waveforms seen at the terminus of 50 ft of 50-Ω coaxial cable.

Pulse waveforms may be coupled through an optional pulse transformer, if desired. The proposed standard logic module will provide a shielded transformer selected by taper pin jumpers.

3. Performance Parameters and Worst-Case Analysis

Worst-case analysis (effects of component parameter variations) has considered both catastrophic failure and performance variation. By definition a catastrophic failure is one that occurs when component parameters values are such that the circuit does not respond usefully to an input logic level shift. Concerning this possibility, the line driver is similar to the typical nand gate in its insensitivity to component value change. Since the Hi-Rel module series uses high-quality metal-oxide-over-glass resistors, catastrophic failure due to resistor changes requires shifts of

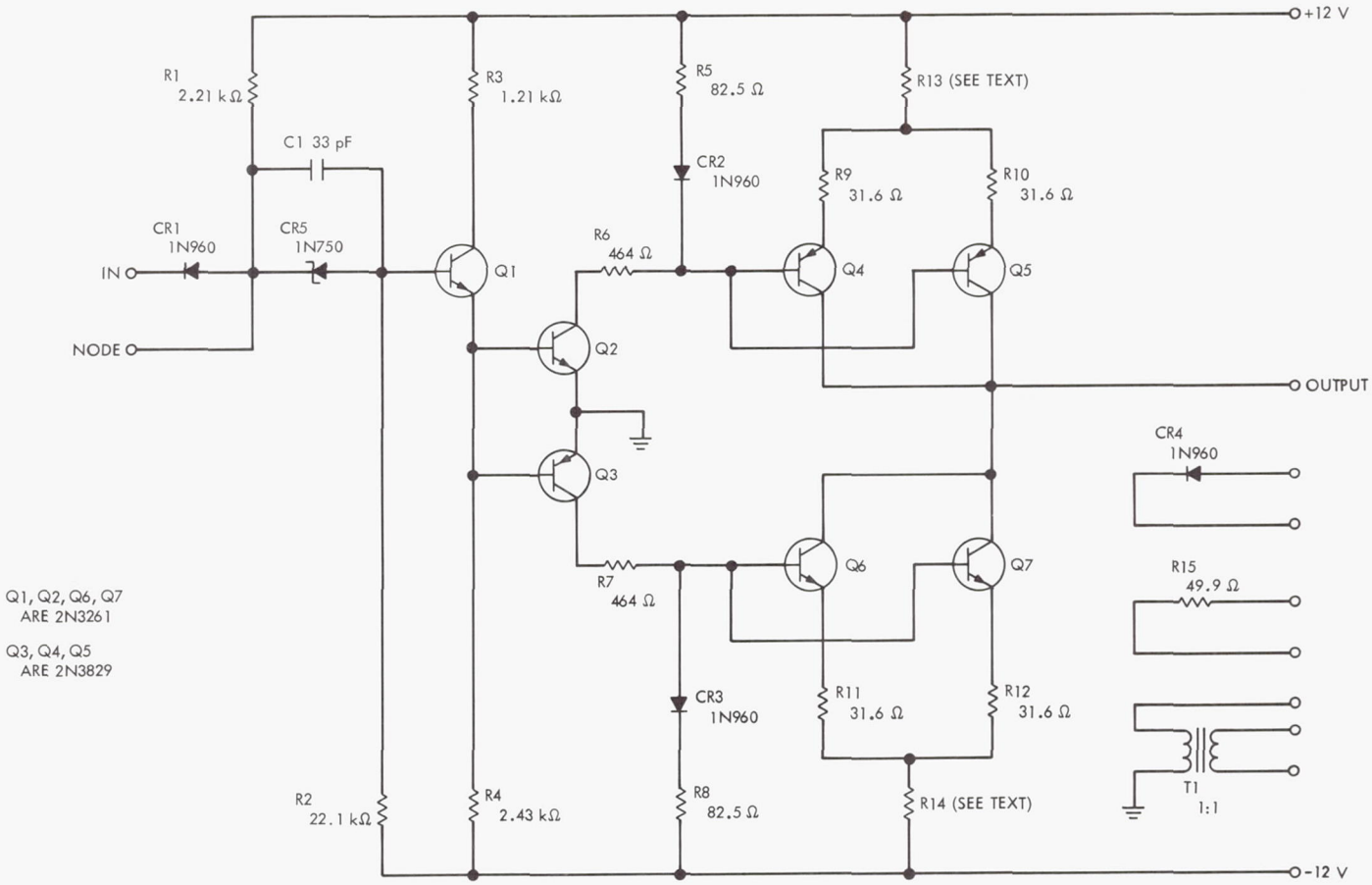

Fig. 12. Line driver circuit diagram

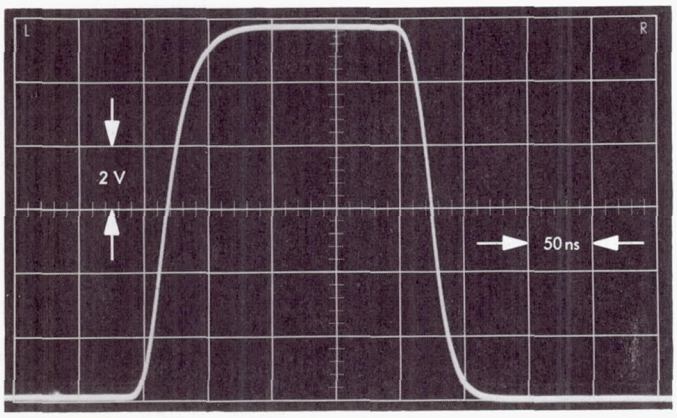

Fig. 13. Line driver output waveform

an order of magnitude or more outside the normal tolerances and aging. Transistor current gains would have to decrease by a factor of 3 or more below normal minimums.

Worst-case analysis of the circuit performance parameters is currently being performed, and the following is a qualitative discussion. The significant circuit performance parameters which require worst-case analysis are: (1) output current magnitude, (2) logic propagation delay, and (3) waveform rise and fall time.

Because this line driver is intended for general-purpose application, it was not a simple matter to arrive at a specification for these performance parameters. The procedure has been to survey the potential applications as well as possible; also it was decided that there would be no attempt to provide performance out of line with the rest of the Division 33 Hi-Rel module family. Because the same transistors are used, the rise and fall times are typical of the Hi-Rel power amplifier, about 25 ns.

Presently, transistors are being measured in the test circuit specified by the transistor screening specification. These measurements will be analytically compared to

their performance in the line driver, and a worst-case performance will be derived. Figure 13 is a photograph of a typical output waveform across a 50-Ω load. The stability of the output current is of interest for some applications. The current magnitude is directly proportional to the value of resistors R5–R6 and R7–R8 which form voltage dividers; also to the value of resistance between the emitters of the output transistors and the supply voltage. Diode CR2 (in the positive current source) and CR3 (in the negative current source) are included to compensate the temperature coefficient of the transistor base voltage; data are currently being sought concerning the variance of this temperature coefficient.

The current gain of the output transistors is also a factor which determines the output current to the extent that the transistor base current produces an unwanted effect on the voltage division provided by R5, CR2, and R6. Currently available data indicate a stability of ±5% for the output currents, including the effect of aging and a temperature range of 10 to 65°C. The output currents may increase an additional 2 to 3% at 100°C.

VIII. Design and Implementation of Technical Structures and Utilities

A. Pioneer DSS Antenna Surface Reset,

V. B. Lobb and J. Carpenter

1. Introduction

An evaluation measurement of the rms surface distortion of the Pioneer DSS antenna was made upon completion of the mechanical portion of the Pioneer DSS upgrade. The calculated rms distortion indicated a significant antenna gain loss at S-band frequency. It was decided that the surface should be reset on a noninterference basis along with the servo and electronics upgrade.

2. Surface Measurement Before Panel Resetting

A theodolite was installed in the center of the 85-ft dish and bucked in on the four datum plane targets (near the corners of the square girder) which were installed after the completion of the mechanical upgrade. Readings were taken using the new technique for setting perforated plate panels described in *Subsection VII-C*. The dish measurements were read to ± 0.060-in. accuracy, which was close enough to furnish data for surface evaluation. These data were reduced in the field by hand to a 1-σ value of 0.66 in. rms, and then computed on the RMS Best Fit computer program focal length fit with a resulting 0.3-in. rms distortion. Peak surface deviations in excess of 2 in. were measured in numerous places. See Fig. 1 for the resulting computer contour plot of the measured best-fit surface.

A graph of antenna dB loss versus surface rms distortion was computed to check the loss of antenna gain (Fig. 2). The antenna loss (from Fig. 2) was 1.5 dB for a 0.3-in. rms distortion. This loss was consistent with the antenna's previous performance, which was from 1.0 to 2.0 dB below the DSN average over the past 2 yr. A surface panel reset was required to improve the antenna's performance.

3. Panel Resetting

Using the data obtained on the first evaluation, data sheets were made which showed the rib and row numbers, the position of the panels which were to be shimmed, and the amount of adjustment to be made.

Seventy-five percent of the panels were shimmed using circular aluminum shims, in increments of 0.125 in. The remaining 25% of the panels were set by resetting the panel attach clips. The shimming and setting of the surface was accomplished in one-fifth the time required by the old setting procedure.

PIONEER DSS; 85-ft POLAR ANTENNA; Z-POSITION; FIELD READING;
FOCAL LENGTH FIT; rms SURFACE DISTORTION = 0.3000 in.; OCT. 10, 1968.

CONTOUR DEFINITIONS

1/2 RF PATHLENGTH ERROR, in.	LABEL
-1.250	A
-1.000	B
-0.750	C
-0.300	D
-0.250	E
-0.000	F
0.250	G
0.500	H
0.750	I
1.000	J
1.250	K
1.500	L
1.750	M

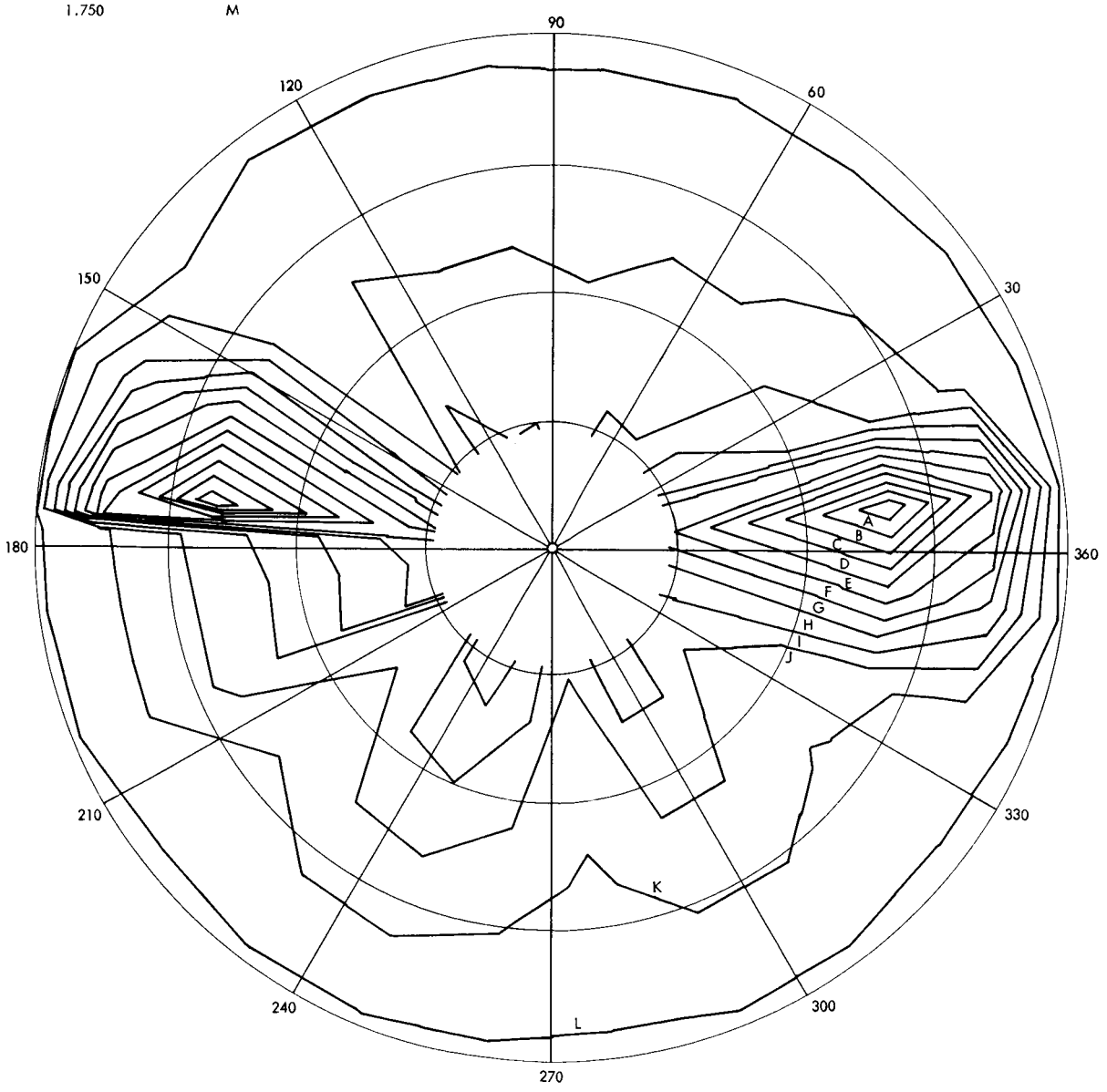

Fig. 1. Computer plot of measured best-fit surface before resetting

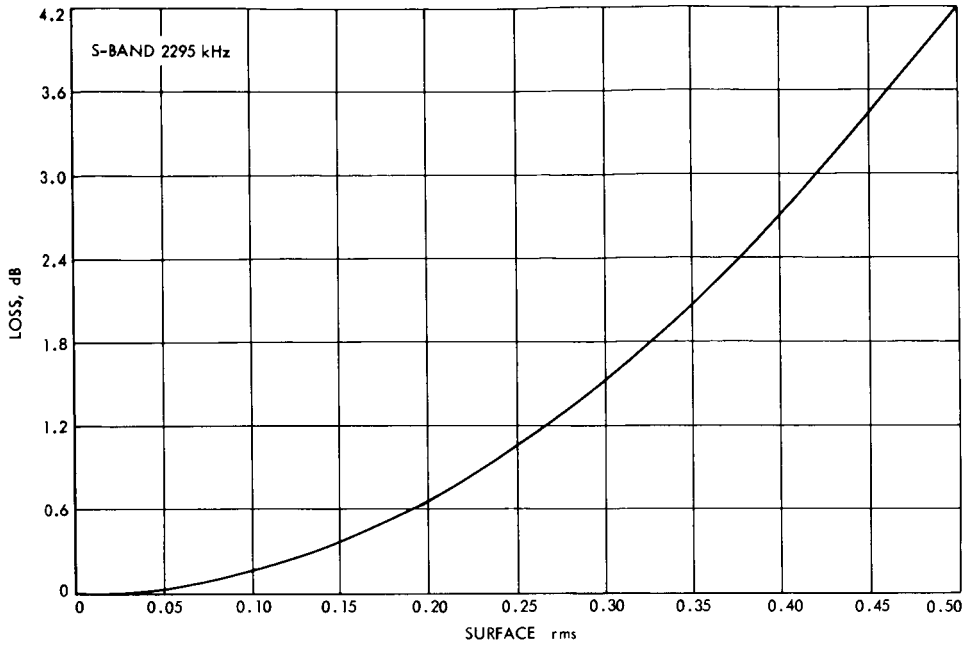

Fig. 2. Loss in decibels at S-Band versus surface distortion

The hyperbola was aligned and set to the new mechanical axis and the panel edge angles were installed

4. Surface Measurement After Panel Resetting

The dish measurements taken during and after the completion of the panel settings were read to ±0.030-in. accuracy. This is a higher setting accuracy than is nominally needed for antenna performance at S-band, considering that the individual antenna panels have an 0.080-in. rms surface distortion. The higher reading accuracy was used so that a more accurate computation of the dish rms (i.e., panel-setting rms) value could be made by the computer.

Surface measurements and computer computations indicated that the dish rms surface distortion was 0.0375 in. This value combined with the individual panel rms distortion value (0.080 in. rms) results in an rms value of 0.090 in.

The antenna loss (Fig. 2) was 0.13 dB for 0.090 rms. See Fig. 3 for the resulting computer contour plot of the measured best-fit surface.

5. Conclusions

The surface evaluation following reset should improve the antenna gain by 1.4 dB. The optical check and mechanical setting of the surface which indicates the 1.4-dB gain will be verified by antenna RF performance on future *Pioneer* spacecraft tracking.

B. Mars DSS Operation Support Building Implementation, *T. Potter*

The new operation support building at the Mars DSS was completed and ready for occupancy on Aug. 31, 1968. In order to meet tracking requirements and at the same time implement the new building for the *Mariner* Mars 1969 reconfiguration and tests, it was necessary to operate both the pedestal control room and the new control room and to obtain some additional subsystems from the Pioneer DSS. When the decision was made that the Mars DSS would support the *Apollo 8* mission, the station was reconfigured. Concurrently with the implementation of the new control room (Fig. 4) in the operation support building, the station met all *Apollo 8* test requirements and continued to fulfill prior tracking commitments. The station was operational except for 5 days while several subsystems were being moved from the pedestal control room to the new control room. Table 1 lists the equipment that was transferred, modified, and implemented.

The communications room will be a self-contained center. The following equipment has been installed:

The microwave antenna and tower (Fig. 5) were moved from the generator building to the communications room

PIONEER DSS; 85-ft POLAR ANTENNA; Z-POSITION; FIELD READING;
FOCAL LENGTH FIT; rms SURFACE DISTORTION = 0.0375 in.; OCT. 19, 1968.

CONTOUR DEFINITIONS

1/2 RF PATHLENGTH ERROR, in.	LABEL
-0.125	A
-0.100	B
-0.075	C
-0.050	D
-0.025	E
0.000	F
0.025	G
0.050	H
0.075	I
0.100	J
0.125	K

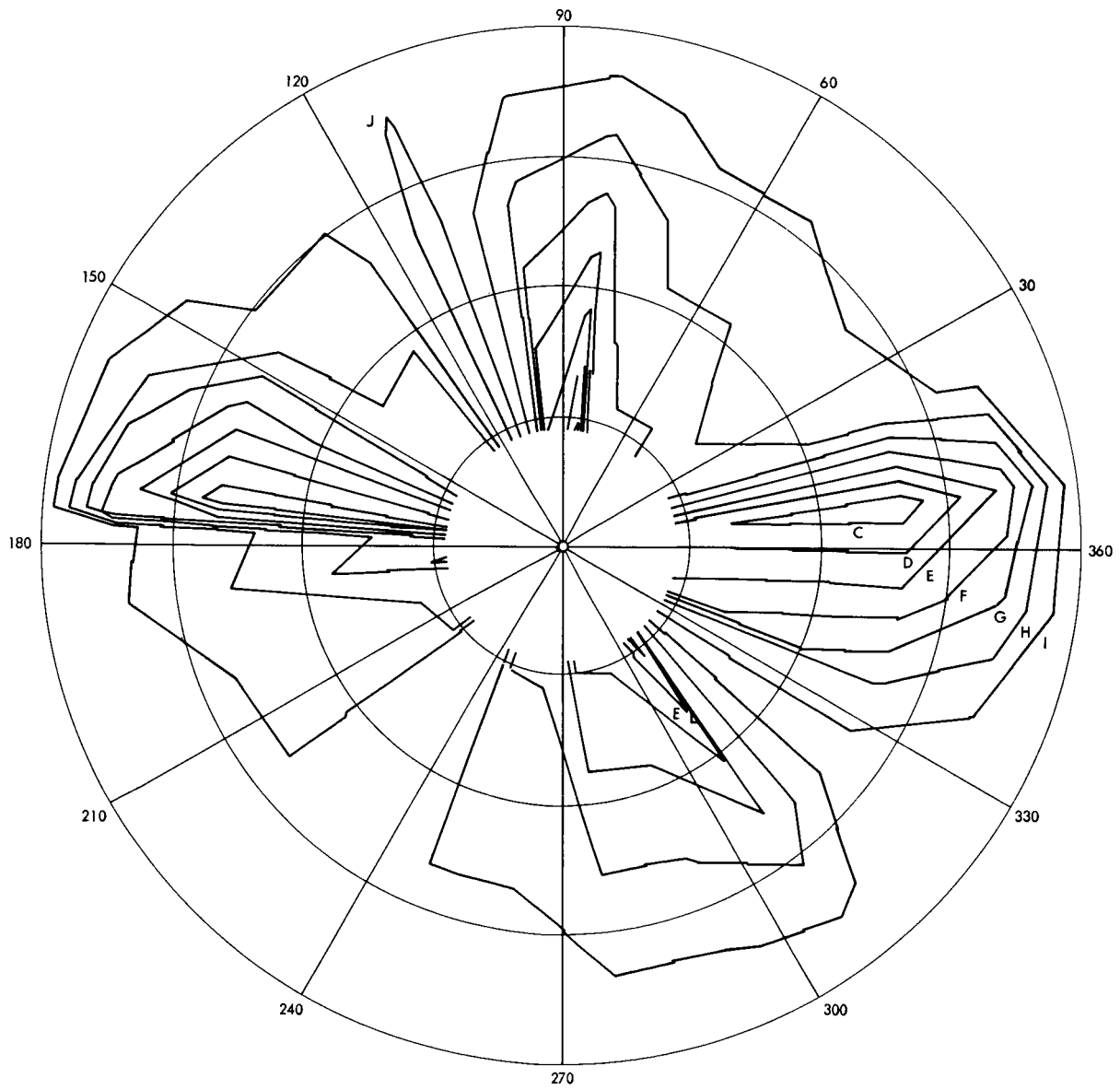

Fig. 3. Computer plot of measured best-fit surface after resetting

Fig. 4. Control room at the operation support building at Mars DSS

Table 1. Operation and support building control room equipment installation

Unit	Comment
Receiver-exciter SN1	Replaces SN3
Receiver-exciter SN3	To be used in Block III-C subcarrier demodulator assembly
Digital instrumentation and frequency and timing subsystems	Received from Pioneer DSS and modified for Phase II
Tracking and data handling, analog instrumentation, recording, and ranging subsystems; station control and monitor console, and ground operational equipment	Removed from pedestal control room
SDS 910 computer	Received from Pioneer DSS and modified for antenna-pointing subsystem
Telemetry and command data-handling subsystem	Transfer rack 1034 received from Pioneer DSS. Transfer rack 1838 moved from pedestal control room. Telemetry and command processor is new equipment
Transmitter system high-voltage supply	Remote control panel moved from pedestal control room and mounted on transmitter
System junction module	SJM 1, 3, and 5 were received and modified
Angle data subsystem	Master equatorial will be modified and aligned
Antenna microwave subsystem switch control and test signal control rack	Control racks for each maser and receiver test transmitter will be located in pedestal control room
Servo electronic control and monitoring cabinets	Moved from pedestal control room

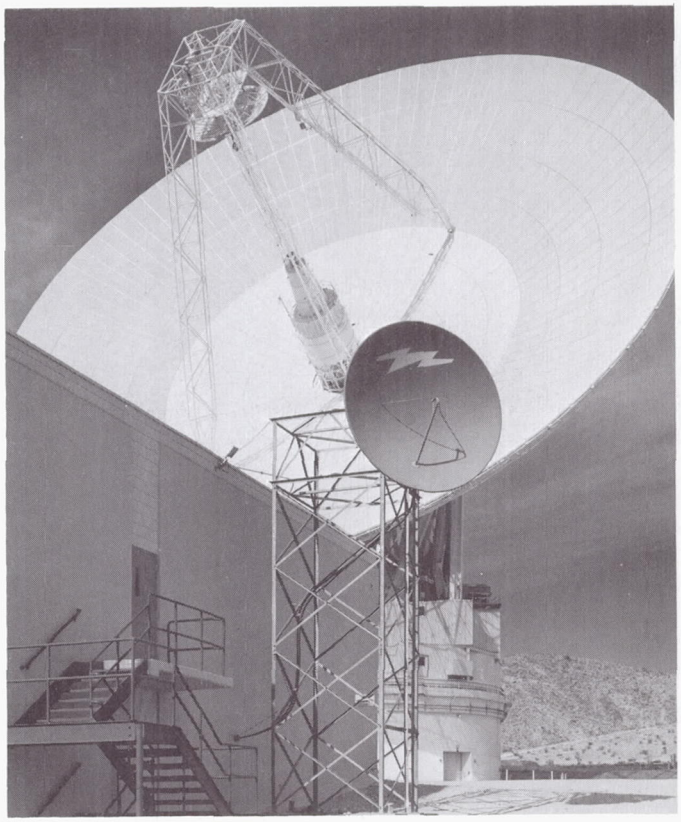

Fig. 5. Microwave antenna installation at Mars DSS

(Fig. 6) and became operational by Oct. 3. Two high-speed data lines bays, one voice data bay, station communications control group bays, communications junction module, teletype machines, ground operational equipment, and read-write-verify command equipment have also been installed.

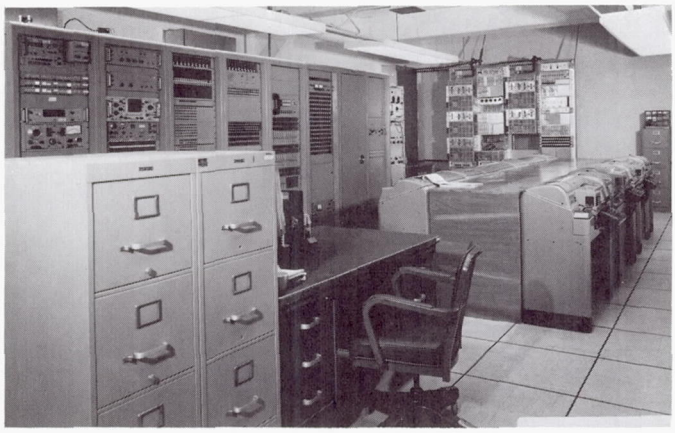

Fig. 6. Communications center of operation support building at Mars DSS

Planetary ranging equipment, SDS 920 computers, programmed local oscillators and receivers for the R&D equipment are being moved from the alidade to the pedestal control room.

A computer listing of all system cables was prepared. Approximately 200 system cables plus some subsystem cables were required for the new equipment, relocation of equipment, and operation of the two control rooms. Forty percent of the cables has been installed.

C. Reconfiguration of Goldstone DSCC Communications Centers, *B. G. Bridges*

A communications center reconfiguration is in process for the purpose of standardization of equipment throughout the DSN. The Echo DSS communications center and the Goldstone DSCC Communications Switching Center have been reconfigured (SPS 37-52, Vol. II, pp. 152–154). Since the last reporting period the Mars DSS and Pioneer DSS communications centers have also been reconfigured.

The Echo DSS communications center equipment (Fig. 7) consists of: communications junction module, high-speed data lines, stations communications control group (SCCG), and tactical intercom. The SCCG of the Echo DSS consists of three bays of equipment: two for teletype and one for voice/data. The Echo DSS has no intersite microwave equipment; it is connected with the communications switching center microwave equipment by twelve 75-Ω foam flex coaxial cables.

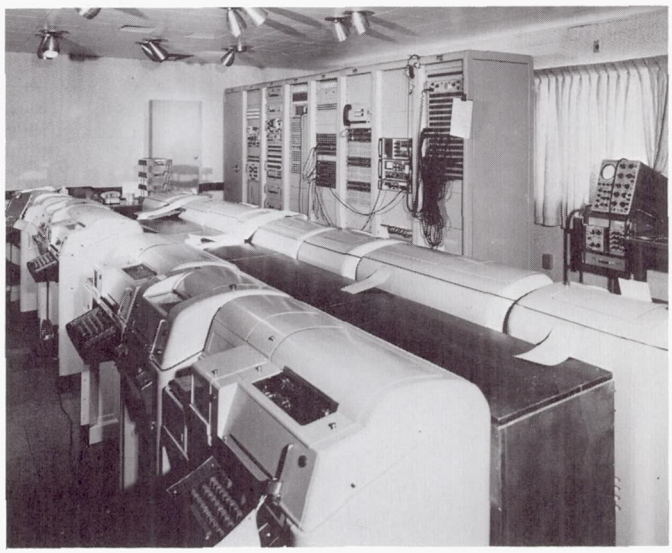

Fig. 7. Echo DSS communications center equipment configuration

The Pioneer DSS will not be fully operational until April 1969. It will have the same equipment as the Echo DSS. The station is being used at present in a limited configuration (communications only) to assist in the support of the *Apollo 8* mission.

The Mars DSS assumed complete communications operations on December 11, 1968. The subsystems in operation are: tactical intercom, teletype, high-speed data, SCCG, and intersite microwave. Figure 6 in *Section VIII-B* depicts the communications center equipment configuration.